Structure and mechanical properties of aluminosilicate glasses

Dissertation

zur Erlangung des akademischen Grades Doktor-Ingenieur
(Dr.-Ing.)

vorgelegt dem Rat der Chemisch-Geowissenschaftlichen Fakultät
der Friedrich-Schiller-Universität Jena

von M. Sc. Thilo Grammes
geboren am 12.08.1990 in Saarbrücken

Gutachter:

1. Prof. Dr. Delia S. Brauer
   Friedrich-Schiller-Universität Jena
2. Prof. Dr. Dominique de Ligny
   Friedrich-Alexander-Universität Erlangen-Nürnberg
3. Prof. Dr.-Ing. Joachim Deubener
   Technische Universität Clausthal

Tag der Verteidigung: 19.02.2020

Acknowledgements

First and foremost, I would like to express my sincere gratitude to Prof. Dr. Delia S. Brauer for her guidance throughout this thesis, for valuable teaching and discussions and for providing outstanding opportunities for collaborations.
I gratefully acknowledge financial support by the DFG within the priority programme SPP 1594, as well as support by the DAAD.
Within said priority programme, my work profited immensely from collaboration with Prof. Dr. Dominique de Ligny (Erlangen) and Prof. Dr. Leo van Wüllen (Augsburg). I am very grateful for their support and inspiring discussions. Special thanks to Alina Nizamutdinova (Augsburg). As part of her own Ph.D. thesis she carried out a detailed structural characterisation of my glasses by solid-state NMR spectroscopy.
Additionally, I owe significant progress of my research to scientific stays in Athens (Greece) and Tampere (Finland) and would like to thank Dr. Efstratios I. Kamitsos (National Hellenic Research Foundation) and Dr. Jonathan Massera (Tampere University) for their support, great advice and their hospitality.
Furthermore, I would like to thank Alexander Veber for support with Brillouin and Raman spectroscopy, René Limbach for ultrasonic echometry and nanoindentation, Amy Nommeots-Nomm for DTA, Steffi Ebbinghaus and Mikko Hokka for XRD, Prof. Dr. Falko Langenhorst for TEM, Johannes Buchheim and Detlef Schelle for EDX, Christian Zeidler, Thomas Kittel, Florian Lindner and Claudia Aichele for refractive index measurements, Tadiyos Tarekegn Alemayehu for assistance with crack resistance measurements, Timothy Oshiobughie Imogore for implementing the centre of gravity calculation into *Matlab* and Gabriele Möller for excellent sample preparation. Regarding the deconvolution of Raman spectra, I would like to thank Naya Tagiara for her introduction and Maria Rita Cicconi, Carsten Grammes and Domingos de Sousa Meneses for discussions on how to further improve the deconvolution process.
Additionally, I would like to express my gratitude to all of my colleagues in Jena and abroad. In particular, I would like to thank my colleagues and friends Nuttawan Sawangboon and Ferdinand Drünert for their advice. Furthermore, I highly appreciate the feedback from all proofreaders.
Finally, I would like to thank my family and friends for their support and Lisa for her love and encouragement throughout the past years.

Dedicated to my family

spectrum [*Latin*]	-	apparition / ghost
$\sigma\kappa o\pi\varepsilon\omega$ / skopeo [*Ancient Greek*]	-	to study / to observe
spectroscopy	-	the study of ghosts

Attributed to Sir Isaac Newton,
see e.g. ref. [142]

Abstract

The effect of phosphate on the mechanical properties of aluminosilicate glasses so far has barely been studied. Yet, phosphate incorporation bears potential for changing the polymerisation of aluminosilicate glasses and thus their properties. This thesis presents the first detailed mechanical analysis of phospho-aluminosilicate glasses that includes elastic properties. The studied compositions comprised metaluminous glasses from the system SiO_2 - Al_2O_3 - Na_2O - P_2O_5 with 0 to 7.5 mol% P_2O_5 and 50 to 70 mol% SiO_2. The glass hardness and elastic properties were assessed by several techniques of indentation and sound speed measurement and were found to decrease with increasing P_2O_5 content. Changes of these properties with increasing SiO_2 content were less expressed and could be explained by either density changes or polymerisation. Additionally, the densification upon indentation was studied, as well as crack resistance and strain rate sensitivity. Furthermore, phosphate was found to decrease the glass transition temperature and to impede crystallisation. To tailor glass properties, the structure-property relationships need to be understood. This thesis includes a structural analysis by combined infrared and Raman spectroscopy. A far-infrared analysis of the sodium signal indicated a competition between aluminate and phosphate groups for charge-balancing sodium. Also, a correlation was found between shifts in infrared and Raman spectra and the degree of ionic bonding, represented by the theoretical optical basicity. In summary, the mechanical properties and the structure-property relationships of metaluminous phospho-aluminosilicate glasses were characterised and the analysis of the degree of ionic bonding and of the role of sodium provided new structural insights.

Contents

List of symbols and abbreviations

A_i	Area of a band i in spectroscopy
BO	Bridging oxygen
C_g	Packing density
COG	Centre of gravity
CR	Crack resistance
c	Speed of light
c_{water}	Water content
DTA	Differential thermal analysis
d	Thickness of a sample & Indentation diagonal
E	Young's modulus
$\mathcal{E}$	Energy
EDX	Energy-dispersive X-ray spectroscopy
FIR	Far-infrared
FTIR	Fourier transformation infrared spectrometer
f	Brillouin shift
G	Shear modulus
H	Hardness (nanoindentation)
H_v	Vickers hardness (microindentation)
h	Planck's constant
I	Intensity
IR	Infrared
K	Bulk modulus
KKT	Kramers-Kronig transformation
k	Imaginary part of the refractive index
k_B	Boltzmann constant
M	Molar mass
MAS NMR	Magic angle spinning nuclear magnetic resonance
MIR	Medium-infrared
MQMAS	Multiple-quantum magic angle spinning
m	Strain rate sensitivity
m_{ox}	Mass of oxygen in 1 mol of glass
N_A	Avogadro's number
$N_{ox,i}$	Stoichiometric number of oxygen atoms in a component i
NBO	Non-bridging oxygen
NIR	Near-infrared
NMR	Nuclear magnetic resonance

n	Refractive index or its real part
n^*	Complex refractive index
P	Load during indentation
PCI	Probability of crack initiation
Q^n_T	Tetrahedral TO_4 unit with T being the cation at the tetrahedral centre and n denoting the number of bridging oxygens of the tetrahedron
$\mathrm{Q}^{4,high}_{Si/Al}$, $\mathrm{Q}^{4,low}_{Si/Al}$	Stretching of $\mathrm{Q}^4_{Si/Al}$ units with larger ($\mathrm{Q}^{4,high}_{Si/Al}$) or smaller ($\mathrm{Q}^{4,low}_{Si/Al}$) intertetrahedral angles
q	Charge
R	Reflectance
r	Real amplitude of the refractivity
r^*	Complex refractivity
SEM	Scanning Electron Microscopy
T	Temperature & Transmittance (infrared spectroscopy)
T_g	Glass transition temperature
T_x	Crystallisation temperature
T_{2s}	Stretching of TO_4 tetrahedra with two O moving towards T and the other two O moving away from it
TEM	Transmission electron microscopy
V	Volume
V_m	Molar volume
VH	Vertical-horizontal polarisers (cross-polarised Raman)
VV	Vertical-vertical polarisers (parallel polarised Raman)
v_L, v_T	Longitudinal and transversal sound velocity
XRD	X-ray diffraction
x_i	Molar fraction of a glass component i

α	Absorption coefficient in infrared spectroscopy & Polarisability
α_m	Molar electronic polarisability
$\alpha_{O^{2-}}$	(Partial molar) oxygen polarisability
$\dot{\varepsilon}$	Strain rate
$\dot{\varepsilon}_i$	Indentation strain rate
ε_{water}	Molar extinction coefficient of water
ε_y, ε_z	Strain along direction y or z
Θ	Half-angle in X-ray diffraction
θ	Imaginary phase angle of the refractivity

Λ	Optical basicity
Λ_{th}	Theoretical optical basicity
λ	Wavelength
ν	Frequency (in spectroscopic context) & Poisson's ratio (in mechanical context)
ν_s, ν_{as}	Symmetric and antisymmetric stretching vibration
$\tilde{\nu}$	Wavenumbers
$\tilde{\nu}_0$	Laser wavenumbers in Raman spectroscopy
ρ	Density
ρ_{ox}	Oxygen packing density
χ^2	Squared difference between data and a fitted model

1

Introduction

The mechanical properties of aluminosilicate glasses have been valued by humanity already in ancient times. Obsidian, a natural aluminosilicate glass from vitrified lava, found use in the fabrication of tools [13, 23, 53]. In modern engineering, the development of fracture mechanics has demonstrated the high intrinsic strength of aluminosilicate glass fibres [68], paving the way for their use as reinforcement in composite materials. Modern reinforcement fibre glasses, such as *E-glass*, are aluminosilicate glasses with a multitude of additional elements [33, 180]. Because of that, the underlying structural origin of their mechanical properties is hard to grasp. For the aim of tailoring glass properties by manipulation of the glass structure, the structure-property relationships need to be thoroughly understood. This may be achieved by studying the structure of model glasses with as few components as possible before extending the model to multi-component glasses.
The basic structural units of silicate glasses are SiO_4 tetrahedra. They are connected by shared corners, i.e. shared oxygen atoms, to form a network structure. The manipulation of this network structure is key to altering the mechanical glass properties. A highly polymerised network yields favourable mechanical properties. Although such high polymerisation is achieved with pure vitreous silica, the extremely high temperatures required for its processing sparked interest in alternatives with lower glass transition temperature,

yet comparable polymerisation.
Aluminosilicate glasses pose a viable option for this problem. In the most simple case, they contain Al_2O_3 and alkali oxides in addition to SiO_2. The presence of alkaline cations reduces the glass transition temperature but usually also the glass polymerisation, see e.g. ref. [160] and p. 83 of ref. [202]. Aluminium, on the other hand, may take a similar network forming role as Si: If charge-balanced by alkaline cations, aluminium can form tetrahedral $[AlO_4]^-$ units. The associated alkaline cations thus no longer depolymerise the network. If the ratio of aluminium to alkaline cations reaches unity, a fully polymerised glass is obtained, called a metaluminous glass [151]. However, metaluminous aluminosilicate glasses also require relatively high processing temperatures albeit not as high as vitreous silica [160].
Glasses with more than two network formers may open up new possibilities to change glass structure and properties. One option is the use of P_2O_5 as a third network forming oxide besides SiO_2 and Al_2O_3. The incorporation of phosphate is known to reduce the solidus temperature of aluminosilicate melts [250]. Furthermore, the addition of phosphate in the right amount has been found to impede crystallisation in the technical production of some aluminosilicate glasses [65].
Phosphate has been found to strongly associate with certain cations of a melt. In the geological context of solidified magmas, this has sparked interest in finding deposits with elevated concentrations of certain, sometimes rare metals [99, 218, 238]. Furthermore, the presence of phosphate in aluminosilicate melts is of technological interest within the field of waste vitrification [197, 220]. However, phosphate also strongly associates with the alkaline and aluminium cations of aluminosilicate melts [62, 144, 184], thus rendering the bonding scenario more complicated.
So far, only few studies have been published on the effects of phosphate on the mechanical properties of aluminosilicate glasses [116, 219, 220, 256]. All of these studies have investigated glasses with an excess of alkaline ions over aluminium. Also, they have mostly provided data on glass hardness, excluding elastic properties. Therefore, the aim of this thesis was to provide a comprehensive mechanical characterisation of metaluminous phosphoaluminosilicate glasses. To understand the effect of phosphate on the mechanical properties, the glass structure also was to be investigated.
Phosphate forms tetrahedral structural units similar to those of silica and alumina. Usually though, phosphate tetrahedra are partially depolymerised. If present in charge-neutral form, they carry a P=O double bond that does not bind to other tetrahedra [102]. If phosphate associates with alkaline cations, non-bridging oxygen atoms are formed, resulting in further depolymerisation [47, 62, 228]. As phosphate associates both with alkaline ions

and with aluminium, its presence potentially may disturb the formation of $[AlO_4]^-$ tetrahedra charge-balanced by alkaline ions. On the other hand, phosphate may also charge-balance $[AlO_4]^-$ units by formation of Al-O-P bonds [102, 184]. In this bonding scenario, the phosphate itself also takes the role of a fully polymerised tetrahedron and has been found to push optical properties towards those of vitreous silica [37].
The different potential bonding scenarios involving different cations also pose the question to which degree the chemical bonds in such glasses may be regarded as ionic. Chemical bonds in silicate glasses always carry both ionic and covalent character, but they are predominantly covalent in vitreous silica, see e.g. p. 23 of ref. [174]. If phosphate affects the degree of ionic bonding, this should also impact on the directionality and strength of individual cation-oxygen bonds of the network. This may have an influence on mechanical and thermal properties and was therefore also investigated in this thesis.
In order to still be able to conduct a detailed structural analysis, a model glass system with a minimum number of components was chosen for this thesis. This model system comprised phosphate-containing, metaluminous glasses of the composition SiO_2 - Al_2O_3 - Na_2O - P_2O_5, with SiO_2 contents ranging from 50 to 70 mol% and P_2O_5 contents up to 7.5 mol%. Additionally, phosphate-free, metaluminous glasses were synthesised to match the SiO_2 contents of the phosphate-containing glasses, in order to provide a simple and well-understood reference for the effects of phosphate incorporation.
All glasses were characterised for their mechanical properties. A special focus was set on elastic properties and hardness, which were measured by several methods each to verify the reliability of the results. Additionally, the plastic deformation mechanism, the strain rate sensitivity and the crack resistance were investigated. This thesis thus provides the first comprehensive mechanical analysis of metaluminous phospho-aluminosilicate glasses.
Besides mechanical properties, the thermal behaviour, the density and the refractive index were also determined. Their development upon changing glass composition was used to assist in structural interpretation.
The degree of ionic bonding was assessed by two different approaches. One was the oxygen polarisability, based on experimental data of density and refractive index. The other approach was the calculation of the optical basicity of the glasses from their stoichiometric compositions. Both properties describe the electron density around the oxygen anions. As oxygen is the main component of the studied glasses and present in all bonds, this allowed to estimate changes in the degree of ionic bonding. The relationship between oxygen polarisability and optical basicity was compared with a previously established relationship for more simple glasses [41].
Structural characterisation of the glasses by solid-state nuclear magnetic res-

onance (NMR) spectroscopy was carried out by a collaboration partner to analyse the type of structural units of each of the three elements Si, Al and P [161].
Complementary to that, this work provides a detailed structural analysis by infrared and Raman spectroscopy, including parallel polarised and cross-polarised Raman spectra. These combined vibrational spectroscopies allowed to partially separate information of phosphate groups from the rest of the spectra. This provided insight into how phosphate affects the bonding of aluminate and silicate groups and vice versa. Changes within both infrared and Raman spectra were correlated with the changing degree of ionic bonding. Furthermore, infrared spectroscopy was used to study the changing chemical environment of sodium and the resulting charge-balancing situation in the glasses. Besides this structural characterisation, Raman spectra were also correlated with the plastic deformation of the glasses caused by indentation.
Chapter 2 of this thesis will provide an overview of the state of the art in phospho-aluminosilicate glass reseach as well as the necessary background knowledge for data interpretation. Details of the experimental procedures will be given in chapter 3. The experimental results and their detailed discussion will follow in chapter 4.

2

Theory and state of the art

2.1 Glass polymerisation

The structure of oxide glasses can be described in terms of their network polymerisation. In simple silicate glasses, the network structure is characterised by the interconnection of SiO_4 tetrahedral units via Si-O-Si bonds, called bridging oxygen bonds (BO). In the more complex glasses studied in this thesis, some of these silicate tetrahedra are substituted by aluminate ($[AlO_4]^-$) or phosphate (PO_4) tetrahedra. The presence of alkaline ions may break bridging oxygen bonds, thus creating non-bridging oxygen atoms (NBO) which are charge-balanced by the alkaline ions. As a result, the glass network structure is depolymerised.
The degree of polymerisation of a tetrahedral unit is expressed by the Q notation. Here, Q^n_T describes a tetrahedral TO_4 unit with T being the cation at the tetrahedral centre (T = Si, Al, P) and n denoting the number of bridging oxygen bonds which connect this tetrahedron with the rest of the network. For example, a Q^3_{Si} unit is a partially depolymerised SiO_4 tetrahedron with three BO and one NBO. Here, this notation includes BO to tetrahedra of all species, e.g. also Si-O-Al bonds or Al-O-P bonds [27, 146].

2.2 Aluminosilicate glasses

While simple silicate glasses contain SiO_2 as the only network forming oxide, aluminosilicate glasses contain an additional potential network forming oxide, Al_2O_3. Aluminium may be present in four-, five- or sixfold coordination [11, 156, 158, 177–179, 186]. Only fourfold coordinated aluminium is regarded as a network former as it forms $[AlO_4]^-$ tetrahedra that contribute to the network structure in the same way as SiO_4 tetrahedra do[1] (Figure 2.1). However, $[AlO_4]^-$ tetrahedra bear a negative charge and require charge-balancing alkaline or alkaline earth cations (summarised as M), see e.g. ref. [186] and p. 231 of ref. [149]. For the sake of simplicity, M will be regarded as alkaline cation with a single positive charge, e.g. Na^+. In simple silicate glasses, the amount of M determines the degree of network polymerisation as bridging oxygen bonds are broken by M, see e.g. p. 83 of ref. [202]. In aluminosilicate glasses, the structural role of Al and M is determined by the ratio of Al/M. Depending on this ratio, aluminosilicate glasses are classified as peralkaline, metaluminous or peraluminous glasses, see e.g. p. 106 of ref. [149]. In peralkaline glasses there is an excess of M over Al. All aluminium forms charge-balanced $M^+[AlO_4]^-$ tetrahedra and acts as network former. The excess M, that is not required for charge-balancing, assumes the role of network modifier, depolymerising the glass [177].
In peraluminous glasses, there is an excess of Al over M, so that not all aluminium can be stabilised in fourfold coordination. As a consequence, all alkaline cations charge-balance $[AlO_4]^-$ tetrahedra, while the excess aluminium assumes higher coordination and may act as network modifier, see

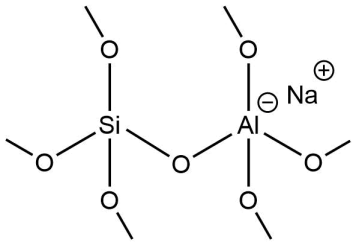

Figure 2.1: Schematic illustration of two connected Q^4_{Si} and Q^4_{Al} groups. The aluminate tetrahedron is charge-balanced by Na^+.

[1] The contribution of $[AlO_4]^-$ tetrahedra to the network structure is so similar to the contribution of SiO_4 tetrahedra that their corresponding signals cannot be distinguished with Raman spectroscopy [11].

e.g. p. 252 of ref. [149]. Alternatively, the excess aluminium may form so-called oxygen triclusters [105], see below for details.
This thesis focusses on metaluminous glasses.[2] Here, the ratio of Al/M is 1, so that all aluminium is stabilised in fourfold coordination and adds to the glass network, while no ions are left to take the role of network modifier, see e.g. p. 114 of ref. [230]. Therefore, the network structure of metaluminous glasses resembles that of vitreous SiO_2, with some SiO_4 tetrahedra being substituted by $[AlO_4]^-$ tetrahedra.
The presence of Al as network former results in some structural peculiarities. Theoretically, two $[AlO_4]^-$ tetrahedra should not be found connected to each other because of charge repulsion. This hypothesis became known as the Löwenstein rule [118]. However, even Löwenstein already mentioned exceptions to that rule [118] and nowadays, more exceptions are known [63, 110, 156, 210]. Another structural anomaly that may occur in metaluminous to slightly peraluminous aluminosilicate glasses is the formation of oxygen triclusters. These are oxygen atoms connecting not two but three tetrahedral units, see e.g. p. 262 of ref. [149]. They are metastable, as the oxygen bears a surplus positive charge in such a configuration. This charge, however, may be balanced by aluminate tetrahedra connected to the tricluster, see e.g. p. 113 of ref. [230]. Triclusters thus allow for the presence of $[AlO_4]^-$ tetrahedra without charge-balancing alkaline cations. Given additional alkaline cations, triclusters may even connect more than one aluminate tetrahedron, thus also breaking the Löwenstein rule [104]. Since their postulation [105], triclusters have been subject of discussion [190, 191, 227, 228], but their existence has been supported by X-ray absorption spectroscopy [21, 172], computational modelling [104, 229] as well as ^{17}O NMR experiments [210, 211]. Nowadays, the concept of triclusters is even being expanded to other glass systems such as borate glasses [232].
The high degree of polymerisation in metaluminous aluminosilicate glasses leads to favourable mechanical properties alongside with high melt viscosities [179, 227]. Young's modulus, E, of aluminosilicate glasses ranges from 60 to above 100 GPa, depending on composition [180, 181, 225, 239]. Their hardness ranges from 5.6 to above 8 GPa [11, 107, 206, 215, 225]. For metaluminous sodium aluminosilicate glasses comparable to the glasses of this study, values of E between 70 and 75 GPa have been found [225, 239] as well as a hardness of 6 GPa [225].

[2] In the geological sciences, metaluminous aluminosilicate compositions are also referred to as tectosilicate compositions [109, 227].

2.3 Phosphate-containing aluminosilicate glass

The incorporation of P_2O_5 as a third network forming oxide into aluminosilicate glasses further expands the range of structural possibilities, and the interaction between phosphate groups and the rest of the glass network is more diverse compared to silicate or aluminate groups. This is caused by the electronic distribution within phosphate groups. As phosphorus bears five valence electrons, a charge-neutral phosphate tetrahedron will be in Q^3_P state (Figure 2.2a). This group is connected to the glass network via three BO and bears a terminal oxygen with a P=O double bond. If a phosphate group forms four BO to the glass network, an additional negative charge-balance for this Q^4_P group is required to compensate the positive partial charge resulting at the phosphate [184]. In phospho-aluminosilicate glasses, the formation of Al-O-P bonds may provide this charge-balance (Figure 2.2b). The involved aluminate groups no longer require charge-balancing alkaline ions. These alkaline ions may instead take a different structural role, such as network modifier or charge-balance for less polymerised phosphate groups. If phosphate is charge-balanced by an alkaline ion, metaphosphate groups (Q^2_P) are formed (Figure 2.2c). With only two BO, they are less polymerised than the abovementioned groups. Here, the surplus electron density of the P=O double bond is delocalised between P and the two NBO[3] (indicated by dashed bond lines in Figure 2.2c) [19].

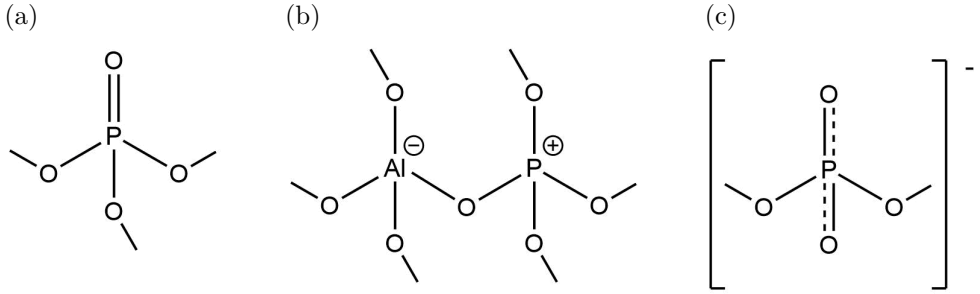

Figure 2.2: Schematic illustration of different phosphate groups. (a) Q^3_P. (b) Q^4_P, charge-balanced by an aluminate group (Al-O-P bond formation). (c) Q^2_P or metaphosphate.

[3] Groups with lower degree of polymerisation (pyrophosphate Q^1_P, orthophosphate Q^0_P) are also possible. The charge delocalisation will then spread over three or four NBO, respectively.

Besides the varying number of NBO affecting glass polymerisation, the surplus electron density of phosphate groups influences the glass structure by attracting alkaline ions.[4] In alkali phosphosilicate glasses without Al, this effect leads to phosphate groups claiming alkaline ions from the silicate network, resulting in a polymerisation of the silicate network, see refs. [47, 96, 112, 117, 184] and p. 492 of ref. [174].
A similar effect has been found for peralkaline phospho-aluminosilicate glasses and melts, owing to their excess of alkaline ions over aluminium [48, 62, 146, 184, 185, 226, 228]. Here, phosphate forms depolymerised groups (Q^0_P to Q^2_P). With increasing Al_2O_3 content, these alkali phosphate groups increasingly assume the more polymerised Q^2_P state [62, 226] and may be connected to the aluminosilicate network [27, 146]. When the Al_2O_3 content reaches metaluminous composition, phosphate additionally forms Q^4_P groups, connected to the aluminosilicate network via Al-O-P bonds [62, 119, 144, 170, 226]. For peraluminous compositions, this Al-O-P bond formation is preferred over the formation of depolymerised phosphate groups [62, 144, 148, 226]. Therefore, phosphate in metaluminous glasses may be expected to be present both as Q^2_P and Q^4_P units [62, 96, 144, 146]. Some studies have additionally suggested the presence of Q^3_P units [146, 189, 228]. Phosphate appears to prefer Al-O-P bonds over Si-O-P bonds. The latter ones are thermodynamically less favourable than Si-O-Si bonds, promoting separation of phosphate and silicate units, see refs. [62, 96, 119, 184] and p. 493 of ref. [174]. The preference for Al-O-P bonds also applies for phospho-aluminosilicate glasses with high silica content [3, 37, 102] and has recently been confirmed even for glasses with four different network formers (Si, Al, B and P) [89]. The formation Al-O-P bonds often has been interpreted as formation of domains with a structure similar to that of the mineral berlinite ($AlPO_4$) [62, 102, 150, 228]. However, minor Si-O-P bond formation has been found to still be possible in glasses with high SiO_2 content, resulting in Q^4_P groups that are not exclusively linked to Al but also to Si [27, 146, 184]. Despite many common ideas of the abovementioned studies, the effects of phosphate on aluminosilicate glass structure are still not fully understood. The requirement of charge-balancing both for $[AlO_4]^-$ and phosphate groups will create competition for alkaline ions [96]. Al-O-P bond formation may liberate alkaline ions from their charge-balancing role. Most studies on phospho-aluminosilicate glass structure focussed on phosphate bonding, neglecting the different roles taken by alkaline ions. In this thesis, the interaction of alkaline ions with Al and P was studied by means of infrared spectroscopy.

[4] Besides that, the increased mobility of the surplus electron density and the increased charge account for a high polarisability of the phosphate groups, which enhances their Raman spectroscopic signals.

Much of the original interest on phospho-aluminosilicate glasses came from the geological sciences, with studies of the solubility of phosphate in magmas and on its ability to attract metal cations, leading to liquid-liquid immiscibilities and property changes of the magmas [119, 170, 184, 185, 250]. This remains a subject of industrial interest with regard to identifying deposits enriched in phosphate, iron or rare elements [99, 218, 233, 238]. The affinity of phosphate for metal cations also bears industrial potential for waste immobilisation applications [197, 219, 220] and needs to be considered during steel production, as there may be phosphate in the aluminosilicate slags used for the purification of iron [237]. Additionally, this effect finds use in the preparation of glass ceramics, if phosphate is applied as nucleation agent for peralkaline aluminosilicate glasses [65]. On the other hand, phosphate apparently acts as crystallisation inhibitor as soon as the Al/alkaline ratio approaches metaluminous compositions [65].
All of these applications are focussed on the binding of certain elements by phosphate. Studies on the effect of phosphate on the mechanical properties of aluminosilicate glasses have only started recently. To the knowledge of the author, only peralkaline compositions have been examined in the literature [116, 219, 220, 256]. This thesis thus presents a first extensive mechanical investigation of metaluminous phospho-aluminosilicate glasses.

2.4 Studied glass compositions

Three different series of glass compositions were studied in this thesis. The first series consisted of glasses with constant 60 mol% SiO_2 and increasing phosphate content from 0 to 7.5 mol%. The phosphate was not simply added to a base composition, but substituted for equal amounts of Al_2O_3 and Na_2O. By doing so, the ratio of Si/Al was changed, but the SiO_2 content could be held constant while preserving the metaluminous state with $Al : Na = 1$. Structural implications will be discussed below. The highest studied P_2O_5 content of 7.5 mol% is a considerable amount when compared to natural magmatic systems[5] and covers the range investigated by most previous studies (7 mol% P_2O_5 or less, see e.g. refs. [27, 150, 226]). Therefore, this series allowed to gain a good overview over the effects of relevant phosphate amounts.

[5] Most magmas contain less than 2 wt% of P_2O_5, which already has intense effects on their properties [64, 138, 148]. For comparison, the phosphate-bearing glasses studied in this thesis contained about 5 to 15 wt% (2.5 to 7.5 mol%) P_2O_5.

The second glass series comprised four glasses with constant 7.5 mol% P_2O_5 and silica content varying from 50 to 70 mol%. Here, an increase in SiO_2 content was counter-balanced by corresponding reduction of Al_2O_3 and Na_2O contents to maintain the metaluminous state. In combination with the third, phosphate-free glass series, this series allowed to identify how silica-related property changes and the behaviour of sodium and aluminium were altered under the presence of phosphate.
The third glass series consisted of three phosphate-free metaluminous reference glasses with 50, 60 and 70 mol% SiO_2, respectively. A good understanding of this compositional range based on previous studies (see e.g. refs. [133, 139, 152, 160, 222]) provided an ideal starting point for the identification of phosphate-related structural changes in the other two glass series.
An overview of the studied glass compositions is provided in Table 2.1. All glasses were named following the notation SiXPY, where X denotes the SiO_2 content and Y the P_2O_5 content in mol%.
These three series were chosen to study specific changes of the glass network structure. This is best understood when comparing the cations substituted for each other upon compositional change and how this affects the corresponding tetrahedral units (Figure 2.3). In the two series with constant P_2O_5 contents of 0 and 7.5 mol%, an increasing silica content by one incremental unit of SiO_2 is accompanied by the decrease of the Al_2O_3 and Na_2O contents by 1/2 incremental unit each. In terms of cations (charges are omitted here), 1 Al and 1 Na are replaced by 1 Si. This can be interpreted as substitution of a SiO_4 tetrahedron for a $Na^+[AlO_4]^-$ tetrahedron. As both tetrahedral units are Q^4 units, the glass polymerisation upon changing SiO_2 content may be assumed to remain constant. As results will show, this assumption success-

Table 2.1: Nominal composition (in mol%) of the studied glasses.

Glass	SiO_2	P_2O_5	Al_2O_3	Na_2O
Si70P0	70	-	15	15
Si70P7.5	70	7.5	11.25	11.25
Si60P0	60	-	20	20
Si60P2.5	60	2.5	18.75	18.75
Si60P5	60	5	17.5	17.5
Si60P6.25	60	6.25	16.875	16.875
Si60P7.5	60	7.5	16.25	16.25
Si55.5P7.5	55.5	7.5	18.5	18.5
Si50P0	50	-	25	25
Si50P7.5	50	7.5	21.25	21.25

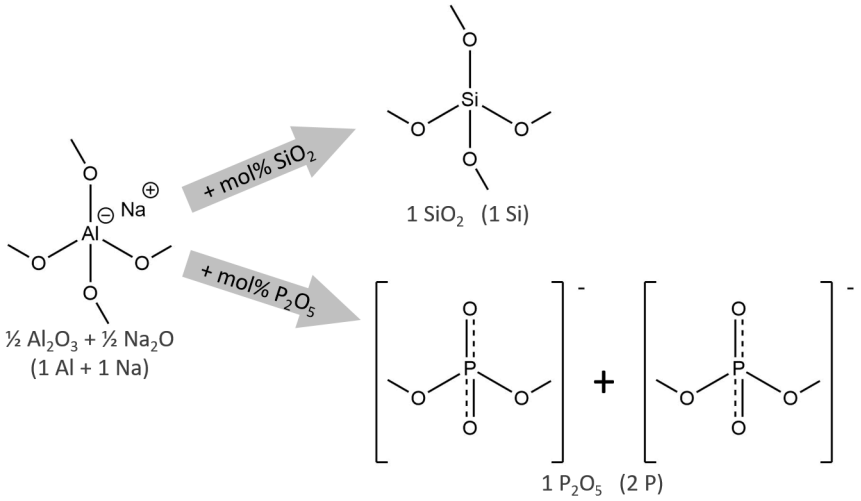

Figure 2.3: Simplified schematic of how $Na^+[AlO_4]^-$ tetrahedra may be replaced upon increasing SiO_2 or P_2O_5 content. Text denotes the oxide units corresponding to the shown tetrahedra and the corresponding cations (in brackets, without charges).

fully explains several property trends, although the structural changes are also affected by the presence of P_2O_5.
Increasing the phosphate content by one incremental P_2O_5 unit corresponds to substituting one unit of $NaAlO_2$, or in terms of cations, to replacing 1 Al and 1 Na by 2 P. In terms of tetrahedra, one $Na^+[AlO_4]^-$ tetrahedron is replaced by two phosphate tetrahedra. The simplified scenario in Figure 2.3 shows them as two Q^2_P groups. Alternatively, Q^4_P units with Al-O-P bonds may also be formed. In either case, the total amount of tetrahedral units per mol increases upon increasing phosphate content. Also, the new phosphate groups bear fewer BO each when compared to the replaced Q^4_{Al} group - unless they form Al-O-P groups. This implies that an increase in P_2O_5 content should decrease the overall glass polymerisation and - because of the higher total number of tetrahedral units - should also increase the molar volume.

2.5 The degree of ionic bonding

The bonding in multi-component oxide glasses is a mixture of covalent and ionic bonding. While some glasses have a rather ionic bonding character, e.g.

those involving fluorides [52], others show mainly covalent bonds, such as vitreous SiO_2, see e.g. p. 23 of ref. [174]. An averaged degree of ionic bonding, or ionicity, provides an additional means to characterise the structure-property relationships of glasses.
As all studied glasses here are oxide glasses, with more than 50 % of all atoms being oxygen, the electron distribution around the oxygen is a good indicator of the overall bonding behaviour. For individual bonds, a theoretical percentage of ionic bonding may be calculated from electronegativity differences, based on tabulated data (see p. 111 of ref. [192]). That is, in order of decreasing percentage of ionic bonding (in brackets): Na-O (74 %), Al-O (54 %), Si-O (44 %) and P-O (32 %). However, the actual ionicities of these bonds will depend on local structure and vary with glass composition. Therefore, other concepts describing the electron density around oxygen proved more useful in the assessment of an average degree of ionic bonding: optical basicity and oxygen polarisability.
The optical basicity, Λ, describes the capacity of oxygen to donate electrons to neighbouring atoms (oxygen as a Lewis base) [40, 43, 45, 46]. An increase in the degree of ionic bonding within a glass will lead to an increase in optical basicity, because the oxygen then is closer to the O^{2-} anionic state and possesses a larger electron density to donate to its surroundings. The optical basicity is defined on a relative scale to CaO, which is thought to have mainly ionic bonding character and represents an optical basicity of unity[6] [46]. To measure the optical basicity, probe ions such as Tl^{+} or Pb^{2+} need to be incorporated into a glass. These ions possess absorption bands in the UV-vis wavelength range which are sensitive to the amount of electron density that the probe ions receive from neighbouring oxygen, thus the name *optical* basicity [40]. However, the glasses in this thesis were synthesised without such probe ions. Alternatively, the theoretical optical basicity, Λ_{th}, may be calculated, based on tabulated optical basicity values of the oxide components of a glass. The corresponding equation may be best understood when given in the notation by Velli et al. [235] for a generalised oxide glass of composition $x_A\, A_mO_n$ - $x_B\, B_pO_q$ - ..., where A and B are cations, x_A and x_B molar fractions of the oxides and m, n, p and q the stoichiometric numbers of the oxides.

$$\Lambda_{th} = \frac{nx_A}{nx_A + qx_B + ...}\Lambda\left(A_mO_n\right) + \frac{qx_B}{nx_A + qx_B + ...}\Lambda\left(B_pO_q\right) + ... \quad (2.1)$$

[6] Unfortunately, the definition of optical basicity is only based on CaO. No reference material for highly covalent bonds with low basicity has been considered and there are also ionic oxides with $\Lambda > 1$, see e.g. p. 165 of ref. [39]. Therefore, an exact percentage of ionic or covalent bonding in a glass cannot be inferred from optical basicity.

Here, the fractions preceding the optical basicities, Λ, of the individual oxides indicate the relative amount of oxygen contributed to the glass by each oxide.

When optical basicities are only available from such calculations, the oxygen polarisability, $\alpha_{O^{2-}}$, provides an additional measure of ionicity that is partially based on experimentally accessible properties. A high oxygen polarisability indicates large electron density around the oxygen, which is then closer to being an O^{2-} anion. The glass then has a higher degree of ionic bonding. To derive $\alpha_{O^{2-}}$, one first needs to calculate the molar electronic polarisability, α_m, of a glass from measured values of refractive index and density. This is done using the Lorentz-Lorentz relationship [40].

$$\alpha_m = \frac{3V_m}{4\pi N_A} \cdot \frac{n^2 - 1}{n^2 + 2} \tag{2.2}$$

Here, N_A is Avogadro's number, n the refractive index[7] and V_m the molar volume derived from density. The molar electronic polarisability, given in volume units of $Å^3$, is a measure of polarisability that has been averaged over the entire glass and represents a sum of the partial molar polarisabilities of all constituent ions, weighted with respect to their respective molar fractions [40]. The partial molar polarisabilities of the cations have been found to be constant regardless of the chemical environment, while the partial molar oxygen polarisability changes depending on the surroundings of the oxygen anion [40]. For this reason, the partial molar oxygen polarisability, $\alpha_{O^{2-}}$, may be calculated from α_m using knowledge of glass composition and tabulated partial molar cation polarisabilities.

2.6 Background for NMR spectroscopy

Solid-state nuclear magnetic resonance spectroscopy (NMR) provides a means to study the chemical environment of specific nuclei within a glass, yielding quantitative information about the nuclei's coordination, the polymerisation of their tetrahedral units or even about the neighbouring tetra-

[7] For practical reasons, the refractive index used in the Lorentz-Lorentz relationship is usually measured at a visible wavelength [38, 242, 244]. In this thesis, the index at 632.8 nm was chosen.

hedral species, see e.g. p. 316 of ref. [1].
In short, NMR spectroscopy probes the relaxation of the nuclear spin of an element of interest after resonance excitation with a radio frequency pulse, see e.g. p. 8 of ref. [125]. Signals are presented over a scale of resonance frequency, normalised to the resonance frequency of a reference material. This scale is termed chemical shift, given in ppm, see e.g. p. 46 of ref. [125]. The spin relaxation is influenced by the spins of surrounding electrons, but also by dipolar and quadrupolar interactions. This phenomenon, termed chemical shielding, is the reason why the chemical shift contains information about the chemical environment of the probed nuclei, see e.g. p. 318 of ref. [1]. Roughly, a higher electron density in the vicinity of the nucleus of interest causes more shielding of its nuclear spin, thus moving the corresponding chemical shift to more negative values. The shielding is directional, which causes an anisotropy of the chemical shift in solid samples. In a solid-state NMR experiment, this anisotropy needs to be eliminated by spinning the sample around the space diagonal, with respect to the externally applied field, see e.g. p. 321 of ref. [1]. This technique is termed magic angle spinning (MAS) NMR. MAS NMR experiments may yield information on the nuclei's coordination and the polymerisation of their tetrahedral units, but not on the neighbouring tetrahedral units in a glass. For this, more advanced dipolar-based NMR techniques are required [16, 161, 162, 189, 249] which are beyond the scope of this thesis.
Not all elements bear suitable nuclear spins to be probed, but all elements of the studied glasses can be theoretically investigated with NMR spectroscopy. In this thesis, MAS NMR results for the nuclei ^{27}Al, ^{29}Si and ^{31}P will be presented.

2.7 Background for vibrational spectroscopy

Infrared (IR) and Raman spectroscopy, summarised as vibrational spectroscopy, are two complementary methods to probe molecular structure. They are based on the interaction of light with the characteristic vibrations of molecular groups. Such characteristic vibrations are usually described either as *stretching* or *bending modes*. In SiO_4 tetrahedra, an example of stretching vibration is the collective stretching of all four Si-O bonds around the central silicon atom. An example of bending is the change of Si-O-Si bond angle between two neighbouring tetrahedra [159].

Vibrational spectroscopy probes the energies corresponding to the characteristic vibrations. Factors determining this energy include the strength of the chemical bonds within a molecular group, the degree of cross-linking - and thus vibrational coupling - with surrounding parts of the glass network, bond angles and coordination numbers of involved atoms, see e.g. refs. [84, 159, 216] and p. 9 of ref. [207]. The intensity of signals in IR and Raman spectra, called *bands*, represents the relative abundance of the corresponding groups in the studied material. The information on abundance is only semi-quantitative, though, because intensity also depends on the symmetry of the group vibrations, see p. 83 of ref. [217]. Still, vibrational spectra may yield information on the short range order of a glass, e.g. an estimation of the types and relative amounts of present Q groups or the coupling between different groups. Furthermore, vibrational spectra may contain information on aspects of the medium range order in glasses, i.e. the relative ordering of atoms beyond the distance of 1 - 2 atomic bonds. For example, Raman spectroscopy is sensitive to collective Si-O-Si bending vibrations of larger rings which are made up of individual SiO_4 tetrahedra, see e.g. p. 83 of ref. [217]. Such *ring breathing modes* can be distinguished with regard to the size of the ring structures and thus provide information on the openness of the glass network structure [58, 200]. Shifts of their associated Raman bands may even indicate density changes of the glasses because they are correlated with bond angle changes [29, 36, 56, 183].
The energy, $\mathcal{E}$, corresponding to a vibration is commonly described in terms of frequency, ν, or wavenumbers, $\tilde{\nu}$, in cm^{-1}, see e.g. p. 3 of ref. [207].

$$\tilde{\nu} = \frac{1}{\lambda} = \frac{\nu}{c} = \frac{\mathcal{E}}{hc} \tag{2.3}$$

Here, λ is the vibrational wavelength, c the speed of light and h is Planck's constant. In this thesis, the terms *wavenumbers*, *frequency* and *energy* will be used equivalently in the context of vibrational spectroscopy, as they all are proportional.
Different criteria determine IR and Raman signal generation. They are called selection rules. To be IR-active, vibrations of a molecular group need to cause a change in the group's dipole moment. To be Raman-active, they need to cause a change in group polarisability. Therefore, IR and Raman spectra yield complementary information.

2.7.1 Different IR approaches

In infrared spectroscopy the sample is exposed to light of a wide range of IR wavelengths. Characteristic signals are generated by resonance absorption at the wavelengths that match the vibrational frequencies in the molecular groups of the sample, see e.g. p. 85 of ref. [217]. The IR wavelength range may be roughly divided into the near-infrared (NIR, 0.8 - 5 μm or 12500 - 2000 cm^{-1}), medium-infrared (MIR, 5 - 25 μm or 2000 - 400 cm^{-1}) and far-infrared (FIR, 25 - 400 μm or 400 - 25 cm^{-1}) ranges. The NIR range contains signals from water that may be integrated into the glasses. The MIR range provides information on the vibrational groups of glasses, complementary to Raman spectra. The FIR range contains the vibrations of alkaline ions.

IR reflection In the MIR and FIR range, light absorption is too strong to determine absorption bands by transmission spectroscopy. Instead, the light reflected from the sample surface needs to be analysed. Additionally, the FIR signals are not easily accessible, because absorption from atmospheric components is also strong in this range. To overcome this, measurements need to be performed in vacuum. IR reflectance spectra differ from transmittance spectra and are not easily interpreted in terms of glass structure. Instead, spectra of the absorption coefficient need to be calculated.
The absorption coefficient, α, of a vibration can be linked to the imaginary part, k, of the complex refractive index, $n^* = n + ik$, with the vibration's wavenumber, $\tilde{\nu}$ [83, 85, 123].

$$\alpha(\tilde{\nu}) = 4\pi\tilde{\nu}k(\tilde{\nu}) \tag{2.4}$$

These *loss* properties are directly accessible by transmission, but not reflection experiments. Here, to gain k, several steps are required, the main one being a Kramers-Kronig transformation (KKT). The KKT allows to transform a known real part of a complex property into the imaginary part, and vice versa, see refs. [98, 252] and p. 430 of ref. [97]. A reflectance spectrum $R(\tilde{\nu})$ carries information from both real and imaginary parts of the refractive index, so the KKT cannot directly extract k. One may, however, define the complex reflectivity $r^*(\tilde{\nu})$ of the sample as a function of its real amplitude $r(\tilde{\nu}) = \sqrt{R(\tilde{\nu})}$ and imaginary phase angle $\theta(\tilde{\nu})$, writing $ln(r^*(\tilde{\nu})) = ln(\sqrt{R(\tilde{\nu})}) + i\theta(\tilde{\nu})$, see p. 432 of ref. [97]. Here, the measured re-

flectance constitutes the real part, allowing to calculate the imaginary phase angle $\theta(\tilde{\nu})$ with the KKT [85, 208].

$$\theta(\tilde{\nu}) = \frac{2\tilde{\nu}}{\pi} \int_0^\infty \frac{ln\,(r(\tilde{\nu}'))}{\tilde{\nu}^2 - \tilde{\nu}'^2} d\tilde{\nu}' \tag{2.5}$$

The phase angle can then be used to calculate both real part, n, and imaginary part, k, of the refractive index with the Fresnel equations [85].

$$n(\tilde{\nu}) = \frac{1 - r(\tilde{\nu})^2}{1 + r(\tilde{\nu})^2 - 2r(\tilde{\nu})cos(\theta(\tilde{\nu}))} \tag{2.6}$$

$$k(\tilde{\nu}) = \frac{2r(\tilde{\nu})sin(\theta(\tilde{\nu}))}{1 + r(\tilde{\nu})^2 - 2r(\tilde{\nu})cos(\theta(\tilde{\nu}))} \tag{2.7}$$

Subsequently, a spectrum of the absorption coefficient may be calculated using Equation 2.4. The use of the KKT in Equation 2.5 introduces an error as it requires extrapolation of the reflectance spectrum to zero and infinity. This error is, however, not significant and will be discussed in Section 3.9.

IR transmission and water content The use of hydrous raw materials such as hydroxides for glass synthesis may introduce water into glasses [167]. The water may be present as molecular water (H_2O) or as hydroxyl groups (OH) bonded to network forming ions. In this thesis, the term *water content* will refer to the combined contents of H_2O and OH. The presence of larger amounts of water (≥ 1 - 10 wt%) is detrimental for glass and melt polymerisation [8] and is therefore widely studied in the geological sciences with regard to magmatic behaviour at high water contents [7, 12, 111, 164, 213]. Furthermore, the water content may affect the refractive index [137]. In this thesis, the water content was determined to verify if depolymerisation caused by water was to be expected.
For this analysis, the 3500 cm^{-1} band of NIR transmission spectra was evaluated. This band corresponds to the combined stretching vibrations of H_2O and OH groups [2, 213]. Additionally, a band at 4500 cm^{-1}, assigned to OH groups [213], was investigated in an attempt to quantitatively distinguish between OH and H_2O in the studied glasses. However, that was not successful as the 4500 cm^{-1} band was too weak. In contrast to MIR and FIR, the NIR range is accessible to IR transmission spectroscopy. The following steps are required to calculate the water content from transmission spectra.

To achieve background correction for reflection and scattering losses, transmittance, T, needs to be normalised. In this thesis, it was normalised to the transmittance value at $5000\,\mathrm{cm}^{-1}$, following the method by Palles et al. [167]. This value was free of sample signal, yet still sufficiently close to the bands of interest to define a common baseline level. Afterwards, the absorption coefficient, α, may be calculated from the normalised transmittance, T_n, and the sample thickness, d, using the Lambert-Beer law [167].

$$\alpha = \frac{-ln\,(T_n)}{d} \tag{2.8}$$

The intensity of the maximum of the absorption coefficient at the investigated band, α_{max}, is proportional to the amount of the absorbing species, i.e. the combined amount of H_2O and OH. In order to calculate the water content, c_{water}, from α_{max}, knowledge of the molar extinction coefficient, ε_{water}, of water in the respective glasses is required [167].

$$c_{water} = \frac{\alpha_{max} V_m}{23.03 \cdot \varepsilon_{water}} \tag{2.9}$$

Here, V_m is the molar volume of the glass. The factor 23.03 derives from unit conversions in order to yield c_{water} in mol%.

2.7.2 Raman spectroscopy and polarisation

In Raman spectroscopy, laser light is being scattered by molecular vibrations, see e.g. p. 4 - 6 of ref. [207]. Raman spectra present the vibrational frequency of molecular groups as shift (in cm^{-1}) from the incident laser energy, called the Rayleigh line. The intensity of Raman scattering, I_{Raman}, is proportional to $\alpha^2 \tilde{\nu}_0^4$, where $\tilde{\nu}_0$ is the wavenumber of the incident laser and α the polarisability of the scattering group, see p. 86 of ref. [207]. Groups of different polarisabilities will differ in signal intensity if present in equal amounts. As a consequence, groups of different net charge, q, may also differ in Raman intensities. The polarisability is roughly proportional to q^2, and therefore $I_{Raman} \sim q^4$, see e.g. p. 537 of ref. [34].
Sample impurities, even at trace amounts, cause a risk of luminescence which may obscure the weak Raman scattering signals. To avoid luminescence, a suitable laser wavelength has to be chosen, see p. 27 of ref. [207]. The choice

of laser wavelength does not affect the Raman scattering frequency, see p. 6 of ref. [207]. However, as the Raman scattering intensity depends on the laser wavelength, an appropriate data reduction is needed to compare spectra measured with different lasers. This will be further explained in Section 3.10.1.

A standard Raman spectrum is referred to as *unpolarised*, even though it is usually partially polarised owing to polarisation of the incident laser. If two polarisers are placed in the path of the Raman signal coming from the sample, then parts of the signal can be filtered depending on polariser angle. The spectrum is called *parallel polarised* if both polarisers are set at 0° to the incident laser's polarisation. Such spectra are referred to as VV Raman spectra (VV: vertical-vertical polarisers) and have a similar appearance as unpolarised spectra. If one of the polarisers is turned by 90°, the spectral envelope changes. The resulting spectra are referred to as *cross-polarised* spectra or VH Raman spectra (VH: vertical-horizontal polarisers).
The VH spectrum may provide different information, such as additional bands that have been hidden in the VV spectrum and symmetry information on individual groups [59, 71, 130, 167]. VV Raman spectra are usually said to be dominated by the signals from *polarised* vibrations while VH spectra show signals from *depolarised* vibrations, see e.g. p. 79 of ref. [1]. For example, phosphate signals are dominant in VV spectra but weak in VH spectra because of the high polarisability that comes with the delocalised surplus electron from pentavalent phosphorus [19, 171].
For disordered solids, important theoretical developments on the correlation between group symmetry and VV and VH spectra were published by Galeener and co-workers [56, 59–61, 130]. In short, they demonstrated that VH Raman, IR and neutron scattering spectra of simple TX_2 glasses such as SiO_2 all map to the vibrational density of states of a glass to some degree. Therefore, they all have similar spectral shapes [59] even though they differ in detail. Their dominant bands are antisymmetric vibrations [56]. By contrast, the strongly differing shape of the VV Raman spectra is mostly caused by symmetric vibrations [61, 130].
Most vibrational modes are neither purely symmetric nor antisymmetric. Yet still, vibrations with a higher degree of symmetry will be subject to stronger suppression upon cross-polarisation. This allows to determine symmetry differences, which is helpful in the assignment of Raman bands.
The use of cross-polarisation is best demonstrated with an example (Figure 2.4). Here, five bands are indicated by the letters F, G, H, I and K.[8] The

[8] The letters were chosen to match the notation of the band assignment in Section 4.6.

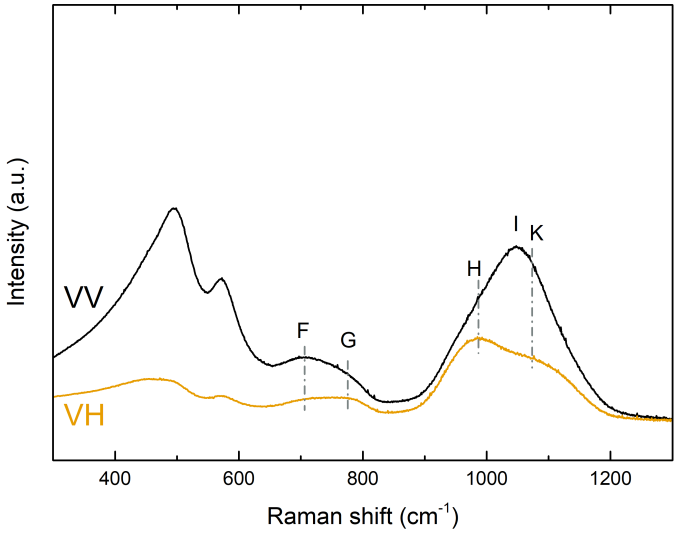

Figure 2.4: VV and VH Raman spectra of an exemplaric glass. The VH spectrum contains bands hidden in the VV spectrum (H,K). Changing relative band intensities upon cross-polarisation reveal different group symmetries (F,G). The VH spectrum was enlarged to identify features more easily.

bands H and K are not distinguishable in the VV spectrum. Only band I clearly marks the VV maximum. The asymmetric shape of VV band I can only be explained by additional, hidden bands. These are the bands H and K which become visible in the VH spectrum, when the contribution from the symmetric vibration I is suppressed.
As regards bands F and G, their relative intensities change from VV to VH spectrum. Band F is more strongly suppressed upon cross-polarisation. Vibration F therefore must be more symmetric than vibration G.

2.8 Background for the mechanical properties

2.8.1 Elastic deformation

The elastic constants describe reversible material deformation under non-critical loading conditions. The constants probed in this thesis were shear

modulus, G, bulk modulus, K, Young's modulus, E and Poisson's ratio, $\nu = -\varepsilon_y/\varepsilon_z$. Poisson's ratio describes lateral material contraction ε_y upon strain ε_z. The moduli describe the material's resistance towards hydrostatic compression (K), shearing (G) and uniaxial tension with lateral contraction (E), see e.g. p. 160 of ref. [22]. Assuming isotropic symmetry in glasses, the elastic constants may be calculated from the longitudinal and transversal sound velocities, v_L and v_T, and the glass density, ρ [115, 181, 195].

$$G = \rho v_T^2 \tag{2.10}$$

$$K = \rho \left(v_L^2 - \frac{4}{3} v_T^2 \right) \tag{2.11}$$

$$E = \rho \left(\frac{3v_L^2 - 4v_T^2}{\left(\frac{v_L}{v_T}\right)^2 - 1} \right) \tag{2.12}$$

$$\nu = \frac{v_L^2 - 2v_T^2}{2\left(v_L^2 - v_T^2\right)} = \frac{E}{2G} - 1 \tag{2.13}$$

The elastic moduli correlate with the volume density of energy. In a silicate-based glass, this energy density will depend on individual bond strengths, the coordinations of the atoms, the degree of polymerisation but also on the packing density [128, 180, 181]. Even if individual bond strengths, atomic coordinations and degree of polymerisation remain constant, the packing density may still change for a glass system if e.g. SiO_4 tetrahedra are substituted for $Na^+[AlO_4]^-$ tetrahedra. The aluminate tetrahedra will require more free volume because of the charge-balancing sodium ions. Rouxel noted that, although the elastic modulus appears to be proportional to glass transition temperature, T_g, this correlation is not universal. The packing density appears to affect the modulus only, not the glass transition temperature [180, 181].

Poisson's ratio has been linked to packing density, glass polymerisation and even to plastic deformation mechanisms. For increasing polymerisation, ν decreases over various glass systems [180, 246]. On the other hand, ν increases non-linearly with increasing packing density [107, 180, 181, 195] or, in other words, with decreasing free volume. The free volume determines how much a glass may be permanently densified. This degree of densification can thus also be linked to Poisson's ratio [246] and, moreover, ν may be used to estimate whether the dominating mechanism of plastic deformation in a glass is densification or shearing [195]. However, all of these dependencies

of ν have been reported over a wide range of glass systems, sometimes with significant scatter within a single system. Therefore, in the limited compositional range of this study, Poisson's ratio can merely provide weak hints towards structural trends.
Elastic constants were determined by ultrasonic echometry, Brillouin spectroscopy and nanoindentation. Ultrasonic echometry is the simple measurement of sound velocities within macroscopic samples of known thickness using transducers. Brillouin spectroscopy and nanoindentation are less straightforward and will be explained below in more detail.

Brillouin spectroscopy Instead of externally inducing sound waves in a sample and measuring their propagation speed, Brillouin spectroscopy draws information from the scattering of light on thermal phonons, i.e. scattering on sound waves in the sample. A good explanation of the underlying physical processes alongside with derivation of the equations has been published by Whitfield et al. [240]. Brillouin spectroscopy is similar to Raman spectroscopy, the difference being that the frequency shift of the incident laser light for Brillouin scattering is much smaller than for Raman scattering. The measured acoustic modes depend on the geometry of the Brillouin experiment. In the most simple setup, the backscattered light from right angle sample irradiation is detected. This backscattering geometry only allows for the measurement of longitudinal modes, see p. 124 of ref. [1]. The Brillouin shift, $f_{backscatter}$, of this geometry is linked to the longitudinal sound velocity, v_L, by the following equation [173].

$$f_{backscatter} = \frac{2nv_L}{\lambda} \tag{2.14}$$

Here, n is the refractive index of the sample and λ is the incident laser wavelength. Besides the backscattering geometry, glasses in this study were also investigated in the platelet geometry. Here, the laser is directed onto a thin sample slice under 45° to the sample normal. The scattered signal is measured on the opposite side of the sample slice, also under 45° to the sample normal, see p. 125 of ref. [1]. The use of this symmetric geometry allows elimination of the dependence on refractive index, giving the following relationship between the Brillouin shift, $f_{platelet}$, of either longitudinal or transversal modes with their corresponding sound velocities, v [240].

$$f_{platelet} = \frac{v\sqrt{2}}{\lambda} \tag{2.15}$$

In theory, the use of platelet geometry and Equation 2.15 is sufficient to determine both longitudinal and transversal sound velocities, without even requiring knowledge of the sample's refractive index. However, deviation of the sample slices from perfect plane parallel geometry introduces errors of the Brillouin shifts in platelet geometry. To account for this deviation, the longitutinal sound velocity, v_L, was taken from backscattering geometry, which can be performed with higher precision. The transversal sound velocity, v_T, obtained from the platelet geometry, was corrected for the deviation between the longitudinal sound velocities obtained from both geometries: $v_{T,corrected} = v_T \cdot v_{L,backscatter}/v_{L,platelet}$.

Nanoindentation Nanoindentation allows to simultaneously determine hardness and elastic modulus, using the method by Oliver and Pharr [165, 166]. During a nanoindentation experiment, a self-similar indenter tip, usually a diamond Berkovich tip [122], is pressed into the sample surface with increasing load, P, and constant strain rate, $\dot{\varepsilon}$ [122]. Continuous measurement of load over indentation depth allows to determine the hardness as a function of the indendation depth [115, 165, 257]. To determine the elastic modulus, the continuous movement of the indenter tip is superimposed with a sinusoidal vibration that allows to measure unloading cycles over the indentation depth [115, 165, 257].
The elastic modulus obtained from nanoindentation is not completely identical with Young's modulus, E. Young's modulus is strictly defined for uniaxial stresses with only minor lateral contraction while the indentation experiment creates a complex three-dimensional stress condition [165, 181]. Nevertheless, owing to the uniaxial movement of the indenter the nanoindentation modulus is usually treated similar to Young's modulus in the literature [113–115, 126, 165]. The same will be done here, but keeping the experimental differences in mind. As the results will show, the difference between modulus values obtained from nanoindentation and the other two methods is systematic, but small.

2.8.2 Plastic deformation and densification

In contrast to the common notion of glass as a brittle material, glasses may be plastically deformed on sufficiently small scales [28, 92]. This allows the study of glass hardness as well as the plastic deformation mechanism. Low

hardness brings a higher risk of surface flaw formation upon contact with another material. Upon load, such surface flaws may eventually lead to catastrophic failure.
In this study, glass hardness was investigated both by microindentation and nanoindentation. The main difference between these methods is the probed sample volume: The diagonals of indentations from both methods differed by one order of magnitude.
During microindentation, a diamond indenter of the Vickers pyramidal geometry is pressed into the sample surface with a defined load and pressing time. Afterwards, the size of the resulting indentation is determined by microscopy. The Vickers hardness, H_v, may be calculated by the following equation, see ref. [115] and p. 175 of ref. [22].

$$H_v = 1.8544 \frac{P}{d^2} \tag{2.16}$$

Here, P is the load in N and d is the indentation diagonal in μm. The factor 1.8544 summarises geometrical terms.
Hardness measurements by nanoindentation have already been described in Section 2.8.1. Advantages of nanoindentation are the direct calculation of hardness from load and calibrated properties without the need for optical investigation of the indentations [165], as well as depth dependent hardness measurement. However, nanoindentation may yield slightly higher hardness values compared to microindentation. This is because the optical investigation of a microhardness indentation only gathers information from plastic deformation, while the load signal from nanoindentation comprises information from both plastic and elastic deformation [165].

With regard to the plastic deformation mechanisms of glasses, one may distinguish between densification and shearing [195]. The dominant mechanism is closely linked to the openness of the glass structure as may be expressed by packing density and polymerisation. These properties are linked to Poisson's ratio, ν. The dominant deformation mechanism has been found to be densification for highly polymerised glasses with low $\nu < 0.2$ and shearing for glasses with high $\nu > 0.3$ [195, 254]. The glasses studied in this thesis were created with the aim of high polymerisation, so that densification should be the main deformation mechanism. As will be seen later, their ν values ranged between 0.20 and 0.24. Therefore, both deformation mechanisms should be partially active but densification can be expected to be the dominating deformation mechanism [72, 195, 254].
In accordance with the dependence of the deformation mechanism on ν,

the maximum permanent densification has also been found to be higher for glasses with low ν values [183]. In vitreous silica, the maximum densification upon indentation may be as high as 20 vol% [92, 108]. Densification behaviour is not only of importance for mechanical glass performance but is also studied in the geological sciences, with interest in the behaviour of magma within the Earth's mantle [172, 187, 204]. In this thesis, the densification behaviour was studied by investigating the shift of the low frequency envelope of Raman spectra upon microindentation, which may be related to changing bond angles and thus changing density [29, 36, 56, 183]. This experiment was performed under the assumption that densification is the dominant deformation mechanism.

2.8.3 Cracking

If a glass is loaded beyond the range of plastic deformation, fractures will eventually occur. As soon as a crack is *critical*, i.e. able to continue growing until rupture of a part, a major failure criterion is met. The fracture behaviour of the glasses in this study was investigated using a Vickers microindenter. By applying different loads, the average number of critical cracks per indentation and load can be used to define a probability of crack initiation (PCI) [91]. A Vickers microindenter can cause several types of fractures, an overview may be found in ref. [28]. Out of these fracture types, radial cracks are the most critical. They may emerge from the four corners of a Vickers indentation (Figure 2.5) and then continuously grow into the material, only being able to stop if the local load is reduced or the part ruptures. A PCI of 100 % corresponds to each indentation developing four radial cracks. The transition from low to high PCI is usually nonlinear over load [91, 115]. The load at which the PCI reaches 50 % is defined as crack resistance (CR) for easier comparison of different materials [91, 193].
Higher crack resistances have been linked to higher silica contents of glasses [73] and to the dominance of densification as plastic deformation mechanism [10, 115]. Furthermore, atmospheric humidity may affect the crack resistance [73].

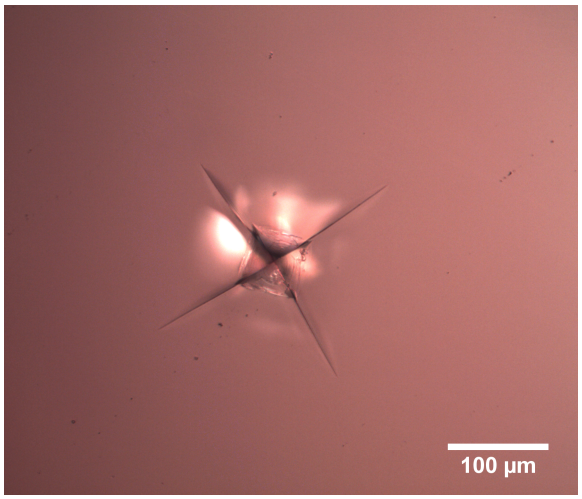

Figure 2.5: Vickers indentation (load 19.6 N) on a glass, showing four radial cracks.

2.8.4 Rate-dependence

A relatively new method of mechanical characterisation applied in this thesis is the investigation of strain rate sensitivity, m, based on nanoindentation strain rate jump experiments. Developed by Maier et al. [126, 127] and transferred to amorphous materials by Limbach et al. [114], this method probes changes of hardness, H, depending on the applied indentation strain rate, $\dot{\varepsilon}_i$.

$$m = \frac{\partial ln H}{\partial ln \dot{\varepsilon}_i} \tag{2.17}$$

The indentation strain rate can be derived from the loading rate in a load-controlled experiment [115, 126]. During a strain rate jump experiment, several different strain rates are applied over the course of a single nanoindentation experiment and the corresponding, sudden changes in hardness are measured to determine m [126]. The strain rate sensitivity has been developed from uniaxial creep experiments which, under constant load, develop a regime of constant strain rate after initial buildup time. Similar to classic creep parameters, the strain rate sensitivity describes an empirical, nonlinear relationship between stress and the rate of material deformation [114].

3

Experimental details

3.1 Glass synthesis

Raw materials for glass synthesis were high purity powders of $Al(OH)_3$ (aluminium hydroxide, hydrargillite, pure, Merck, Darmstadt), SiO_2 (quartz powder, $>99\,\%$, Carl Roth, Karlsruhe), Na_2CO_3 (sodium carbonate, $>99.5\,\%$, Carl Roth) and $NaPO_3$ (sodium metaphosphate, high purity, acidic, Carl Roth). After thorough mixing they were heated from room temperature to 1650°C at 5 K/min in alumina crucibles using a resistive furnace (Model HTK 16/17 FL, Thermconcept Dr. Fischer GmbH & Co. KG, Bremen). They were held at this temperature for one hour, subsequently quenched in air and then transferred to a cooling furnace (Model LM 312.06, Linn High Therm GmbH, Bad Frankenhausen) running at $T_g + 20\,K$ to reduce residual stresses. After an hour at this temperature, the crucibles with the samples were left to cool down to room temperature within the cooling furnace. Glass monoliths (Figure 3.1) were then retrieved by breaking off the alumina crucible walls. The method of casting the glasses out of platinum crucibles and subsequent splat-quenching was not pursued because of high melt viscosity, resulting from high polymerisation. The routine de-

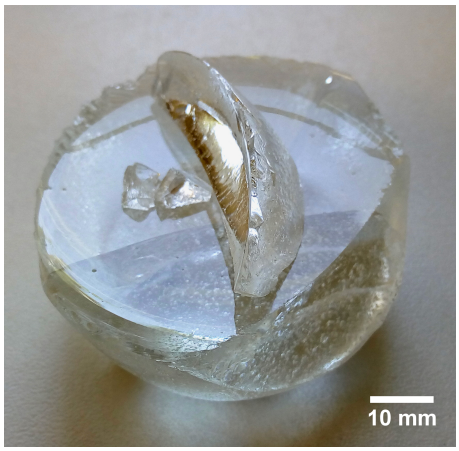

Figure 3.1: Typical glass sample, retrieved after cooling within an alumina crucible, followed by breaking off the crucible walls. Casting and splat-quenching were impeded by high viscosity.

scribed here allowed for comparable synthesis conditions for all glasses except Si50P0.[9] For sample cutting, sections close to the crucible walls were omitted because of potential crucible dissolution. Longer melting times may have been beneficial for sample homogeneity by removing bubbles, but were avoided to prevent excessive leaching of the crucibles.

3.2 Density and related properties

Glass density, ρ, was determined as mean value of ten measurements on a single specimen in a helium pycnometer (AccuPyc 1330, Micromeritics GmbH, Mönchengladbach). Powder samples ($> 5\,\mathrm{g}$) with a particle size of $125 - 250\,\mu\mathrm{m}$ were used to exclude the influence of bubbles. The experimental error was $\pm\,0.01\,\mathrm{g/cm^3}$.
Molar volume, V_m, was calculated from density and molar mass, M_{glass}, of the glasses [55]. M_{glass} is a stoichiometrically weighted sum of the mo-

[9] For glass Si50P0, cooling without crystallisation could only be achieved at a reduced cooling temperature of $T_g - 40\,\mathrm{K}$, owing to its high Na content. However, tests with various cooling temperatures showed that even such reduced cooling temperature had no significant effect on glass properties. This is probably owing to the high polymerisation.

lar masses, M_i, of the individual glass components, i (SiO_2, Na_2O, Al_2O_3, P_2O_5).

$$V_m = \frac{M_{glass}}{\rho} = \frac{1}{\rho} \sum_i x_i M_i \tag{3.1}$$

Here, x_i are the molar fractions of the individual glass components.
Another property derived from density is the packing density, C_g, which represents a normalisation of density to a unitless value [181].

$$C_g = \rho \frac{\sum_i x_i V_i}{\sum_i x_i M_i} \tag{3.2}$$

Its calculation requires the volume, V_i, occupied by the individual glass components, which is assumed to be the sum of their atomic volumes with atoms approximated as spheres.[10]
As the main constituent atom of the studied glasses is oxygen, the oxygen packing density, ρ_{ox}, also is of interest in the description of glass structure. The oxygen packing density was calculated as the mass of oxygen in a unit volume of glass [55, 176].

$$\rho_{ox} = \frac{m_{ox}}{V_m} = \frac{M_{ox}}{V_m} \sum_i x_i N_{ox,i} \tag{3.3}$$

Here, m_{ox} is the mass of oxygen in 1 mol of glass, M_{ox} is the molar mass of oxygen and $N_{ox,i}$ is the stoichiometric number of oxygen atoms provided by each glass component, e.g. 2 for SiO_2, 3 for Al_2O_3, so that $\sum_i x_i N_{ox,i}$ is the number of oxygen atoms in 1 mol of glass. The errors of molar volume, packing density and oxygen packing density were estimated by error propagation.

[10] Different datasets for ionic radii are available in the literature [169, 198, 199, 241]. In this thesis the *effective ionic radii* by Shannon were used as they are most up to date and take interaction between cations and anions into account [198].

3.3 Thermal analysis

Glass transition temperature, T_g, and crystallisation behaviour were studied by differential thermal analysis (DTA, Jupiter STA 449 F1, Netzsch-Gerätebau GmbH, Selb) at Tampere University, Finland. Fine powder samples of 50 mg and particle size $< 38\,\mu$m were heated up to 1500°C at a heating rate of 10 K/min. This heating rate was chosen to ensure good comparability with most literature data,[11] see ref. [131] and p. 240 of ref. [202]. T_g was determined as inflection point of the characteristic endothermal glass transition regime. For the investigation of crystallisation the particle size was varied between $< 38\,\mu$m, 125 - 250 μm and 1 - 2 mm (Figure 4.6 in Section 4.3). The experimental error for all characteristic temperatures was ± 5°C.

3.4 X-ray diffraction

X-ray diffraction was carried out on glass powder using Cu Kα radiation to verify if samples were amorphous and to study crystallisation. X-ray patterns shown in this thesis were measured at Tampere University, Finland (Empyrean, PANalytical, Royston, UK), with an acceleration voltage of 45 kV. Routine tests for verification of amorphous state were carried out at the Otto Schott Institute of Materials Research (MiniFlex 600, Rigaku, Neu-Isenburg) with an acceleration voltage of 30 kV.

3.5 Electron microscopy

Scanning electron microscopy Scanning electron microscopy (SEM) was used to determine glass compositions by energy-dispersive X-ray spectroscopy (EDX). For each glass the composition was calculated as mean value of four EDX measurements. Errorbars represent standard deviations. Three

[11] As an exception, DTA runs shown in Figure 4.3a, Section 4.3, were performed at 20 K/min, but cross-checks at 10 K/min yielded qualitatively similar results.

of these four measurements were run on the same instrument (Phenom pro X, Phenomworld, Eindhoven, NL) but using different specimens. An accelerating voltage of 15 kV was used. Measurement areas were between $200\,\mu m \times 200\,\mu m$ and $400\,\mu m \times 400\,\mu m$ to gain compositional information averaged over a larger area. The fourth EDX measurement was run on a different instrument (Neon 60, Zeiss, Jena, combined with X-Max X-Ray Detector $80\,mm^2$, Oxford Instruments, High Wycombe, UK) at an independent laboratory, using an accelerating voltage of 5 kV and a measurement area of $\sim 115\,\mu m^2$. Results from independent measurements were in good agreement. Additional tests with the second setup showed that results measured with accelerating voltages of 5 or 15 kV were comparable.

Transmission electron microscopy Transmission electron microscopy (TEM, Tecnai G^2, FEI, Hillsboro, US) and electron diffraction were used to verify the absence of small crystallites and of phase separation. Only glasses Si70P0 and Si70P7.5 were investigated.
An accelerating voltage of 200 kV was used. To avoid the time-consuming etching process of standard TEM samples, experiments were run on single glass powder particles of size $< 38\,\mu m$, which were placed on TEM grids by suspension in alcohol. During the experiment, the sharp edges of these particles were examined. Images will not be shown because no signs of crystals or phase separation were found, see Section 4.1.

3.6 Refractive index

The refractive index was measured at 480, 546.1, 632.8 and 1300 nm to cover the range from the visible to the NIR regime. The values at 480 and 546.1 nm were required to interpolate the index at 488 nm, which was needed for Brillouin spectroscopy. The refractive index at 632.8 nm was used for calculation of polarisabilities using the Lorentz-Lorentz relationship (Equation 2.2). The value at 1300 nm was helpful during optimisation of the extrapolation process for the Kramers-Kronig transformation of IR reflectance data. For index determination at 632.8 and 1300 nm, a prism coupler (2010/M Prism Coupler, Metricon, Pennington, US) was used with lasers of the respective wavelengths. Presented refractive indices at 632.8 and 1300 nm are mean values from three to four measurements at different spots on the sam-

ples. Errorbars show standard deviations. The indices at 480 and 546.1 nm were measured by Pulfrich refractometry (PR2, VEB Carl Zeiss, Jena), using a cadmium lamp for 480 nm (F' line) and a mercury lamp for 546.1 nm (e line). Here, the experimental error ranged from ± 0.0003 to ± 0.001, depending on the optical quality of the individual samples.

3.7 The degree of ionic bonding

The degree of ionic bonding was assessed by calculating the theoretical optical basicity, Λ_{th}, and the partial molar oxygen polarisability, $\alpha_{O^{2-}}$. The theoretical optical basicity was calculated using Equation 2.1, with the optical basicities of the oxide components taken from refs. [40, 235]: $\Lambda(SiO_2) = 0.48 \pm 0.01$, $\Lambda(Al_2O_3) = 0.60 \pm 0.01$, $\Lambda(Na_2O) = 1.15 \pm 0.03$ and $\Lambda(P_2O_5) = 0.33 \pm 0.01$. Errors of Λ_{th} were estimated by error propagation.
For calculation of the partial molar oxygen polarisability, the molar electronic polarisability, α_m, was determined first from molar volume and refractive index (Equation 2.2). Then, $\alpha_{O^{2-}}$ was derived using the nominal glass composition and tabulated partial molar cation polarisabilities taken from refs. [40, 50, 235]: $\alpha_m(Si^{4+}) = 0.033\,Å^3$, $\alpha_m(Al^{3+}) = 0.052\,Å^3$, $\alpha_m(P^{5+}) = 0.021\,Å^3$ and $\alpha_m(Na^{+}) = 0.179\,Å^3$. Errors of $\alpha_{O^{2-}}$ were estimated by error propagation of the experimental errors of density and refractive index.

3.8 Solid-state MAS NMR spectroscopy

One-dimensional MAS NMR spectra (Avance III 300 MHz spectrometer, Bruker, Karlsruhe) were recorded for the nuclei ^{27}Al, ^{29}Si and ^{31}P on all studied glasses. The spectrometer operated at a 7 T magnetic field. All NMR experiments were carried out by Alina Nizamutdinova as part of a collaboration with the group of Prof. Dr. Leo van Wüllen, Augsburg University. Further details may be found in her Ph.D. thesis [161].

3.9 Infrared spectroscopy

Reflection experiment Infrared spectra in the MIR and FIR range were recorded on a vacuum Fourier transformation IR spectrometer (FTIR) in reflectance mode (Vertex 80v, Bruker, Karlsruhe) at the National Hellenic Research Foundation in Athens, Greece. The angle of light incidence was 11° off the sample normal. Samples were polished slices. A gold mirror was used to measure the background of instrument and remaining atmosphere at 3.8 hPa. MIR and FIR spectra were recorded separately. The light sources were a globar for the MIR range and a mercury lamp for the FIR range. The amount of scans used in the FIR range (2000 scans) was five times as high as in the MIR range (400 scans) to reach comparable levels of signal quality. Resolution was $4\,\mathrm{cm}^{-1}$. FIR and MIR spectra were merged and cut to cover a total range from at least 75 to $2000\,\mathrm{cm}^{-1}$. Data beyond the cut-off limits was either detector noise (FIR region) or did not contain meaningful structural information (MIR to NIR region). Absorption coefficient spectra were calculated from the merged reflectance spectra using the steps explained in Equations (2.4) to (2.7) with the spectrometer's software *Bruker OPUS*. These calculations yielded absolute values for the absorption coefficient. No further normalisation was applied.
For the use of the Kramers-Kronig transformation (Equation 2.5), the merged spectrum had to be extrapolated to cover all wavenumbers from zero to infinity. This extrapolation involved several parameter choices that potentially may affect the resulting spectra. Care was taken to keep the spectral treatment steps comparable between all samples. The outcome of the KKT was iteratively optimised to match three extrapolation criteria.

- The first criterion required the spectrum of the absorption coefficient to approach zero intensity at zero wavenumbers without discontinuities.
- As a second criterion, the spectrum of the absorption coefficient had to be close to zero for the entire spectral range above $1500\,\mathrm{cm}^{-1}$, where no sample signal was to be expected.
- Additionally, the extrapolation to the high wavenumber end of the spectrum was aided by knowledge of the sample's refractive index at 1300 nm ($\sim 7692\,\mathrm{cm}^{-1}$). As a third criterion, the extrapolated spectrum of the real part of the refractive index, calculated from Equation 2.6, had to roughly match the measured refractive index at 1300 nm.

This iterative optimisation showed that the spectral region of interest was barely affected by variation of the extrapolation criteria. This is in agreement with other findings which have shown the KKT to be rather robust as long as the main signal range from 450 to 1500 cm^{-1} is covered, see p. 432 of ref. [97] for the theory and see ref. [4] for an example of successful application of the KKT process without measuring data below 450 cm^{-1}.

Transmission experiment and water content In order to determine the water content of the studied glasses, additional NIR spectra were measured in transmittance mode from below 2000 to 7500 cm^{-1}, using the same spectrometer and vacuum conditions as for the reflectance measurements. Reference spectra were determined with an empty sample compartment. Samples were plane parallel slices, polished on both sides. Their thickness (about 2 mm) was averaged from ten measurements with a micrometre gauge. The water content was calculated from the 3500 cm^{-1} band of the transmittance spectra (Equations 2.8 and 2.9). Errors were estimated by error propagation. The molar extinction coefficient, ε_{water}, for the 3500 cm^{-1} water band was not determined in this thesis. Instead, the literature value of $67.0 \pm 6.7\,l/(mol{\cdot}cm)$ was taken from a study on metaluminous basaltic, albitic and rhyolitic glasses [213], which are comparable to the phosphate-free glasses of this thesis. This value was also used for the phosphate-containing glasses in the absence of more fitting literature data. By using the same value of ε_{water} over all glass compositions, especially the ones including additional P_2O_5, an error was introduced. However, as water content was very low in all glasses (see Section 4.1), this error is not of further relevance here.

3.10 Brillouin and Raman spectroscopy

Most Raman spectra were obtained alongside Brillouin spectra using a customised optical setup at the university of Erlangen. In short, samples were illuminated in backscattering geometry through a microscope, using an objective lens with 50× magnification and a numerical aperture of 0.42. The experiments were performed at room temperature with a 488 nm sapphire continuous wave laser. The scattered signal was split into low and high frequency portions which were directed to a Brillouin and a Raman

spectrometer, respectively. The details of the optical setup are published in ref. [231]. Polarising optics allowed the recording of VV and VH Raman spectra. To improve signal to noise ratio, the signals obtained from several scans were summarised to a total acquisition time of 2400 s for VV and 4800 s for VH Raman spectra. The doubled time for VH spectra was required because of the low intensity of VH spectra. Raman spectra were recorded from -19 to $+1505\,\mathrm{cm}^{-1}$. To remove the Rayleigh line, the region below $+15\,\mathrm{cm}^{-1}$ was cut off.
Additional Brillouin measurements were performed in the platelet scattering geometry to access both longitudinal and transversal sound velocities. The samples used for both geometries were polished, plane parallel slices. Their thickness (200 - 300 μm) was averaged from five measurements with a micrometre gauge. The instrumental error of the Brillouin shifts was $\pm\,0.012$ GHz. Longitudinal and transversal modes were fitted with Gaussian curves using the software *Origin* (OriginLab Corporation, Northampton, US). Their Brillouin shifts were averaged between the Stokes and anti-Stokes signals to account for the instrumental non-zero position of the Rayleigh line. The averaged Brillouin shifts were used for the calculation of sound velocities (Equations 2.14 and 2.15). The required refractive index at the laser wavelength of 488 nm was linearly interpolated from the measured values at 480 and 546.1 nm. Elastic properties were then calculated using Equations (2.10) to (2.13). Errors of the elastic properties were estimated by error propagation.

Raman analysis was mainly performed on the spectra measured with the setup explained above, because they covered the highest wavenumber range. Yet, backup spectra were measured at the Otto Schott Institute using a Raman microscope (invia Raman Microscope, Renishaw, Wotton-under-Edge, UK) at room temperature with an objective lens with 50× magnification and a numerical aperture of 0.75. The 514.5 nm line from an argon ion laser was chosen for excitation. VV and VH spectra were recorded in the range from 194 to $1539\,\mathrm{cm}^{-1}$. The total acquisition time per spectrum was 300 s, summarised over several scans. These spectra were used to compare the results from two different excitation lines, as shown in Section 4.6.2. They were also used for deconvolution (Section 4.6.5) and in the analysis of a shift of the high frequency Raman envelope which is discussed in Section 4.8.
Furthermore, a Raman analysis of Vickers indentations was performed (Section 4.10.2). The corresponding spectra were measured at the National Hellenic Research Foundation in Athens, Greece. A Renishaw Raman microscope was used, similar to the one described above but with different

specifications. Here, measurements were performed at room temperature using the 488 nm line of an argon ion laser and an objective lens with 50× magnification and a numerical aperture of 0.50. Spectra were measured in the range from 150 to 1550 cm^{-1}. The acquisition time per spectrum was 225 s, summarised over several scans.
Spectral resolution was below 2.5 cm^{-1} for all Raman setups used. However, as their optical components differed in detail, the error of Raman shift for all setups was estimated conservatively as $\pm 3\,cm^{-1}$ for bands with a clear maximum and $\pm 20\,cm^{-1}$ for shoulders.

3.10.1 Post-processing of Raman spectra

The choice of post-processing routine always changes the appearance of Raman spectra. Care needs to be taken to only compare spectra that underwent the same post-processing steps. The analysis of absolute band intensities needs to be avoided as these intensities change depending on the post-processing routine. Instead, trends of the relative intensities between different bands need to be focussed on.
Here, linear baselines were subtracted from the spectra to bring the signal-free region above 1350 cm^{-1} to zero intensity level. The spectral data were reduced to acount for the dependence of the Raman intensity on temperature and frequency (details below). After that, spectra were normalised to the maximum of their respective low frequency bands. This normalisation was chosen to highlight changes of the low frequency bands during glass densification (details below). If Raman spectra in this thesis are given without specific note regarding normalisation, they were subjected to this treatment.

Baseline correction A baseline correction was necessary because spectra often showed a weak non-zero slope in the high frequency region above 1350 cm^{-1} that did not contain sample signal. To account for this background, potentially arising from instrumental setup or luminescence, linear baselines were subtracted from the spectra to bring the signal-free region above 1350 cm^{-1} to zero intensity level. Linear baselines were preferred to minimise arbitrariness in the determination of baseline points, and this is a commonly used routine [5, 50, 71].

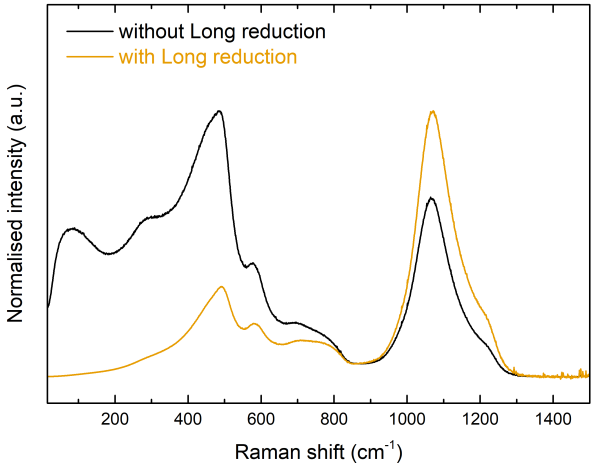

Figure 3.2: Demonstration of the effect of the Long reduction for temperature- and frequency-dependence of Raman scattering on the shape of Raman spectra for a selected glass. Spectra were normalised to their maximum intensities.

Data reduction Raman intensity does not only change with excitation frequency; it also depends on temperature by a Bose-Einstein factor that accounts for vibrations which are not in their ground state because of thermal activation. More detailed equations for Raman intensity may be found in the monographs by Derek Long, see p. 83 of ref. [120] or p. 120 of ref. [121]. To account for these effects, spectral data were reduced by the following equation, often referred to as the *Long reduction* [109, 145, 151, 159, 160, 173, 194].

$$I_{red} = I_{meas} \cdot \tilde{\nu}_0^3 \frac{\tilde{\nu}}{(\tilde{\nu}_0 - \tilde{\nu})^4} \left[1 - exp\left(\frac{-hc\tilde{\nu}}{k_B T}\right)\right] \tag{3.4}$$

Here, I_{meas} and I_{red} are the measured and reduced Raman intensities, respectively. T is the temperature, c the speed of light, k_B the Boltzmann constant ($1.38065 \cdot 10^{-23}$ J/K) and h is Planck's constant ($6.62607 \cdot 10^{-34}$ Js) [159]. There are also other reduction routines in use besides the Long reduction, mostly applying similar principles [14, 17, 61, 70, 167, 171, 205, 216]. The Long reduction is most common, though, and thus was chosen for this thesis. The process reduces intensities at low frequencies and emphasises intensities at higher frequencies (Figure 3.2). The shape of the high frequency region of the spectra is almost unaffected by the reduction while the shape of the low frequency region changes markedly. This is caused by the suppression of thermal activation, which largely contributes to the low frequency region

while not being linked to specific structural groups [31, 136, 159, 167]. The application of the Long reduction in this thesis was optional because no high temperature experiments were performed. The reduction was chosen because the reduced spectra largely resembled the IR spectra in shape. As IR spectra and VH Raman spectra both originate from antisymmetric vibrations [59], this resemblance was considered beneficial for the comparison of the spectra in Section 4.6.

Normalisation Common normalisations either divide the intensities by the highest measured signal (normalisation to maximum) or by the total measured signal (normalisation to integrated spectral area). In certain cases, normalisation to a specific band is also chosen [159]. These three different normalisation approaches are compared for suitability in Figure 3.3 for a series of glasses from this thesis with increasing phosphate content. Normalisation to the spectral maximum (Figure 3.3a) is not suitable for this thesis because not all glasses have their maximum intensity at the same band. Also, the high intensity band at $\sim 1050\,\mathrm{cm}^{-1}$ will be shown later to represent the phosphate content of these glasses. Setting this band to equal intensity for glasses with differing phosphate contents is not beneficial.
Normalisation to the area (Figure 3.3b) is an acceptable routine as here, the band at $1050\,\mathrm{cm}^{-1}$ increases with increasing phosphate content (from glass Si60P0 to glass Si60P7.5). However, there is no band of constant intensity. Shifts and relative intensity changes in the low frequency region from 300 to $650\,\mathrm{cm}^{-1}$ will become relevant later when discussing glass densification. For normalisation to the maximum of the low frequency region (Figure 3.3c), changes in the low frequency region can be more easily determined compared to Figure 3.3b. The increasing phosphate content is still well represented by the increasing intensity of the $1050\,\mathrm{cm}^{-1}$ band. Therefore, normalisation to the maximum of the low frequency region was chosen here as the standard normalisation. This way, a small error regarding the band of the low frequency maximum is created. But, as will be seen in Section 4.6, this band has several structural contributions and is unlikely to maintain the same intensity over all glasses. Nevertheless, in absence of an internal standard this error was regarded acceptable and unlikely to affect the interpretation as long as only relative intensities of different bands are being compared.

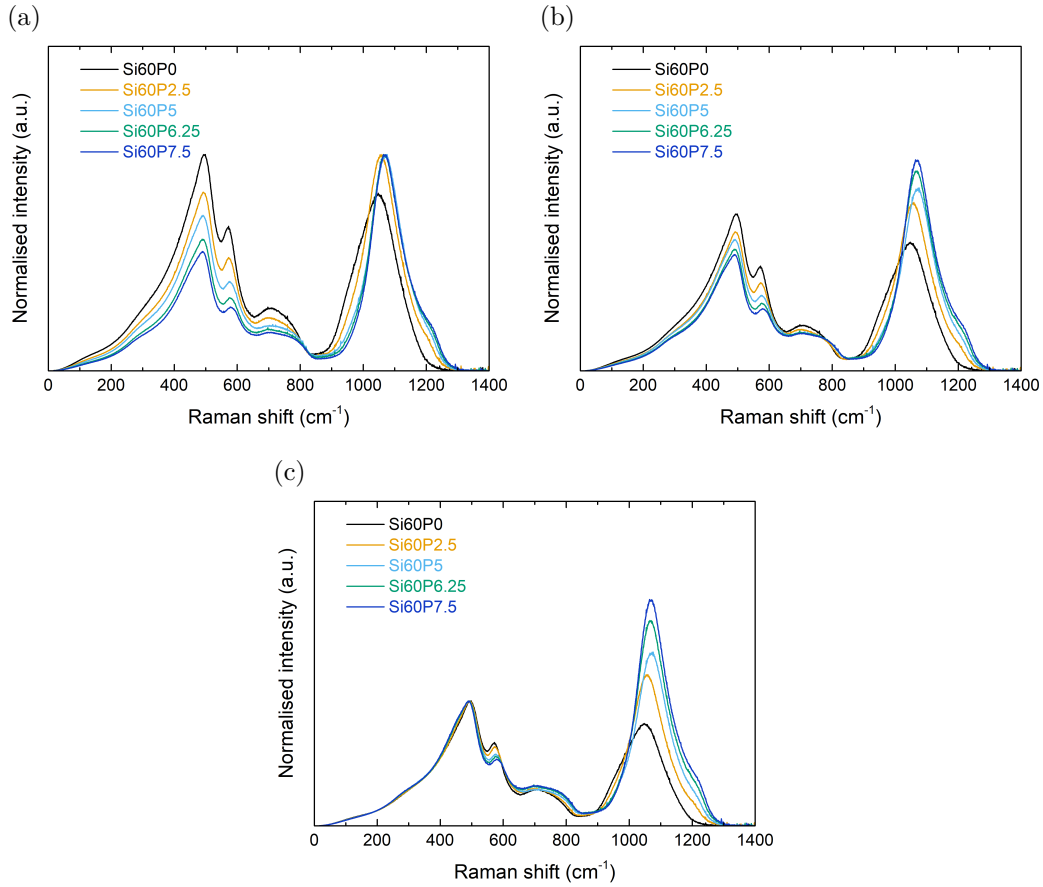

Figure 3.3: Comparison of different normalisation approaches for glasses with increasing phosphate content (0 mol% for Si60P0 and 7.5 mol% for Si60P7.5). (a) Normalisation to spectral maximum. (b) Normalisation to total integrated area. (c) Normalisation to the maximum of the low frequency region.

3.10.2 Raman analysis of densification

Glass densification by indentation resulted in a shift of the low frequency Raman envelope towards higher wavenumbers. In an attempt to characterise the densification, this shift was analysed by adapting the method presented by Deschamps et al. [36]. The low frequency envelopes of Raman spectra measured before and after indentation were integrated to obtain their respec-

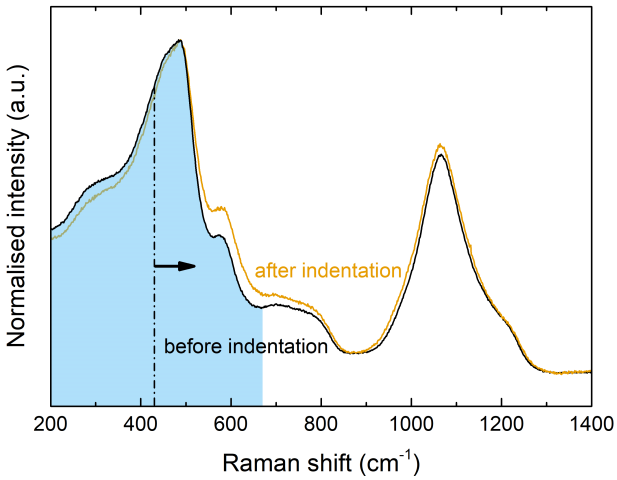

Figure 3.4: Exemplary Raman spectra of a glass before (black) and after (orange) densification by Vickers indentation. The densification shifted the low frequency region (blue area). This is quantified by determining the shift (arrow, not to scale) of the centre of gravity (dash-dotted line) of the affected region. Spectra were normalised to their maximum intensities.

tive centre of gravity by the following equation, using the software *Matlab* (The MathWorks, Inc., Natick, US).

$$\frac{\int_l^{COG} I(\tilde{\nu})d\tilde{\nu}}{\int_l^u I(\tilde{\nu})d\tilde{\nu}} = \frac{1}{2} \tag{3.5}$$

Here, the centre of gravity (COG) is the wavenumber which separates the integrated region into two parts of equal area. I denotes the Raman intensity and $\tilde{\nu}$ the Raman shift in wavenumbers. The lower and upper limits of the integration are l and u, respectively. The integration limits were chosen at the positions of the intensity minima which confined the low frequency Raman region. The error of the position of the centres of gravity was estimated as $\pm 6\,\mathrm{cm}^{-1}$.

After indentation, the entire low frequency region, and therefore also its COG, was shifted (Figure 3.4). The black spectrum in Figure 3.4 represents the glass before indentation, the orange spectrum afterwards. The shift of the low frequency region (blue area) is clearly visible. The dash-dotted line marks the COG position prior to indentation. The arrow (not true to scale) illustrates the COG shift upon indentation. Arguably, the integration limits

could be extended to include the middle frequency region between 650 and 800 cm^{-1}. A discussion of why this was not done follows in Section 4.10.2.
The COG shift was used to quantify the densification. Prior to COG calculation, Raman spectra underwent subtraction of a linear baseline that was fitted to the signal-free high-frequency end of the spectra. Optionally, the spectra were afterwards treated with the Long reduction (Equation 3.4). The two processing routes with and without Long reduction were compared to evaluate the influence of spectral processing on the densification analysis, considering that the Long reduction greatly changes the shape of the low frequency region. The Long reduction also required a change of the lower integration limit because it shifted the corresponding intensity minimum to the lowest measured frequency. This enlarged the integrated range for datasets that underwent the Long reduction. However, the impact of the changed integration limits on the COG calculation was deemed low because Raman intensities in the affected wavenumber regime had dropped significantly after the Long reduction.
A linear baseline fitted just below the integrated region may be considered a valid alternative to the one fitted to the signal-free high frequency end of the spectra. This type of baseline was also tried, but will not be shown as differences were small.
To compare the COG shifts depending on glass composition, Raman spectra measured in the centres of five indentations were investigated per sample, as well as five reference spectra of non-indented glass. The obtained COG shifts were averaged. Each indentation was created with a load of 981 mN with a Vickers microindenter and loading parameters as specified in Section 3.12. Raman measurements were carried out at the National Hellenic Research Foundation as described above. For a selected indentation, a Raman mapping was performed to verify that the indentation centre corresponds to the highest local densification. For this map, 31×31 individual Raman spectra were measured around the indentation centre, with a step size of 1 μm between two measuring positions and a measurement time of 60 s per spectrum. This mapping was performed using the Raman microscope at the Otto Schott Institute with a spatial resolution of $\sim 0.4\,\mu$m. The focus of the microscope was set on the level of the glass surface outside of the indentation. No refocussing within the indentation was performed, because here a clear focal point was hard to identify. Thus, an error was introduced for the points of the map corresponding to the indentation. However, this error was expected to mainly affect intensities, not the analysed frequency shift.

3.10.3 Deconvolution of Raman spectra

Raman spectra were deconvoluted in an attempt to gain further structural information. Deconvolution was performed on unpolarised Raman spectra measured at 514 nm excitation and was limited to the high frequency spectral envelope. Prior to deconvolution, each spectral envelope underwent a linear baseline subtraction and was normalised, setting its intensities to a range from 0 to 100 for easier comparison of the different glasses.
The number of deconvoluted bands was chosen to match the number of bands identified in the VV and VH Raman spectra. Phosphate-free glasses were deconvoluted with three bands, phosphate-containing ones with five bands. Any additional bands may further improve the mathematical fit by minimising the residual, the difference between model and measured data. However, they would also increase arbitrariness of the fitted model [147, 148, 194]. A lower number of bands may in some cases be sufficient for a good fit, but would be meaningless as not all measured bands (VV and VH) would have been taken into account. The band shape was chosen to be Gaussian, the most simple form.
The deconvolution was performed using the software *Origin*. Fitting was carried out with *Origin*'s implemented Levenberg-Marquardt algorithm.[12] During fitting, the squared difference between data and model, χ^2, needs to be iteratively minimised. A tolerance value of $\chi^2 = 1e^{-9}$ was chosen as convergence criterion as well as a limit of up to 10000 iterations. Except for manually choosing starting position and amplitude, no further constraints were applied to the Gaussian fitting parameters. Typically, initial band positions were chosen to roughly match the experimental positions, while initial amplitudes were varied. Output band positions and areas were evaluated. Errorbars show standard errors in case of band positions and error propagation of standard errors in case of relative band areas.

[12] The Levenberg-Marquardt algorithm is a further developed version of the Gaussian non-linear least squares minimisation algorithm and is popular in solving fitting problems owing to its higher tendency to converge, see e.g. p. 228 of ref. [35].

3.11 Ultrasonic echometry

To obtain elastic properties from Equations (2.10) to (2.13), longitudinal and transversal sound velocities in the glasses were measured by ultrasonic echometry (Echometer, Karl Deutsch, Wuppertal). Samples were plane parallel slices. Their thickness (about 2 mm) was averaged from five measurements with a micrometre gauge. The echometer was calibrated with a standard part of defined thicknesses. Its piezoelectric transducer was operating at 8 to 12 MHz. The coupling agent between sample and transducer was honey for transversal measurements and a water based agent (Echotrace, Karl Deutsch, Wuppertal) for longitudinal measurements. Errors were estimated by error propagation from the errors of sample thickness, sound propagation time ($\pm\, 0.001\,\mu$s) and sample density.

3.12 Microindentation

Vickers hardness Glass hardness was determined using a Vickers microindenter (Duramin-1, Struers GmbH, Willich). For each sample, 25 indentations were evaluated with a load of 981 mN, a load buildup time of 15 s and a dwell time of 10 s. Errorbars show the standard deviation.

Crack resistance To investigate crack resistance, 25 Vickers indentations were prepared for each of the loads 981 mN, 1.96 N, 2.94 N, 4.91 N, 9.81 N and 19.6 N. For each indentation, the number of radial cracks was evaluated to determine the respective probabilities of crack initiation (PCI). PCI showed a sigmoidal trend when plotted over the logarithmic load (Figure 3.5). This trend was fitted[13] using the software *Origin*, following the procedure by Limbach et al. [115]. The load value of the fitted sigmoidal curve at 50 % PCI

[13] The fitted function was of the type *logistic dose response*. This empirical function originates from modelling the response of an organism to the dose of a chemical but it also succeeds in describing the response of glass to the level of applied load [115]. The function has the form $y = A_2 + (A_1 - A_2)/[1 + (x/x_0)^p]$, with y being the response (PCI), A_1 and A_2 the lowest (0 % PCI) and highest (100 % PCI) response, respectively, x the load, x_0 the load at $A_2/2$ (crack resistance) and p an empirical slope parameter.

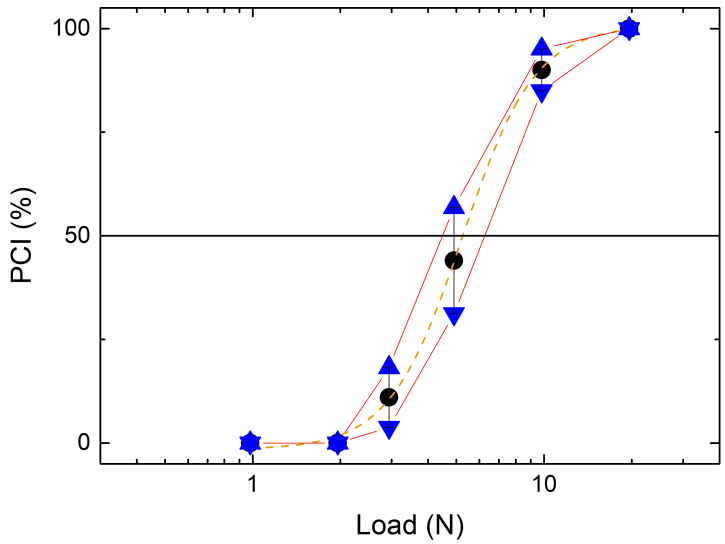

Figure 3.5: Determination of crack resistance and its error from the probability of crack initiation (PCI). The PCI is fitted with a sigmoidal function (orange dashed line). The intersection of this function with the 50 % PCI line marks the crack resistance. Connecting the end points (blue triangles) of the PCI errorbars creates an approximated error envelope (red lines). The intersections of this error envelope with the 50 % PCI line are used to estimate an error for the crack resistance.

was taken as crack resistance for each glass.
Few publications on glass crack resistance show errors for PCI and crack resistance [10, 73]. The reason is probably the large size of the PCI errorbars (Figure 3.5), which indicates scattering of the number of radial cracks formed per indentation. Here, a method was developed to use the PCI errorbars to estimate an error of the crack resistance. In Figure 3.5, the PCI errorbars show the 95 % confidence interval after evaluation of 25 indentations (up to 100 potential cracks) per load. The error of the crack resistance has to be found in the load dimension (horizontal axis). Therefore, the end points of the PCI errorbars (blue triangles) were connected by linear segments to create an estimated error envelope of the PCI (red lines). This error envelope intersects the 50 % PCI line at two loads above and below the crack resistance, generating two horizontal errorbars (not shown). Because of the logarithmic load axis, the crack resistance is not in the middle between these two loads. To achieve symmetric errorbars on a linear load scale, and to be conservative in this error estimation, the larger errorbar out of the two was chosen as the estimated error of the crack resistance.

3.13 Nanoindentation

Nanoindentation experiments (Nano Indenter G200, Agilent Technologies, Waldbronn) were carried out with a diamond Berkovich indenter tip on plane parallel, polished glass samples. Experiments at constant strain rate of $0.05\,\mathrm{s}^{-1}$ were performed to measure elastic modulus and hardness. Additionally, strain rate jump experiments were performed to determine the strain rate sensitivity.
During the constant strain rate experiments, the hardness was continuously measured up to a penetration depth of 2000 nm. To measure the elastic modulus at the same time, the indentation was superimposed with an oscillation of 2 nm and 45 Hz. Modulus and hardness reached a constant value over indentation depth after initial buildup. For each indentation, the values of this plateau region were averaged. The first 20 % (0 to 400 nm depth) of each indentation were omitted from averaging because they contained the pre-plateau buildup. Also, the last 10 % (1800 to 2000 nm depth) were omitted because the corresponding high loads may elastically distort the indenter tip, thus falsifying the contact geometry. The resulting averaged values of hardness and modulus between 400 and 1800 nm indentation depth were further averaged over several indentations. For each sample, 20 indentations were created. A few indentations did not show the plateau behaviour, typically because of bubbles below the sample surface. These indentations were omitted from evaluation. As a result, hardness and modulus were evaluated for 15 to 20 indentations, depending on the sample. Errorbars show the standard deviation.
For the strain rate jump tests, indentations were prepared similar to the ones above, but three different strain rates of 0.05, 0.007 and $0.001\,\mathrm{s}^{-1}$ were applied during the course of each indentation, following the protocol described by Limbach et al. [114]. Each strain rate was maintained over a range of at least 250 nm penetration depth. With the strain rate jumps, the measured hardness changed towards new plateau values. The hardness was averaged over the last 100 nm of each constant strain rate regime, to only cover plateau values without the buildup regimes. For each indentation, the strain rate sensitivity was then calculated (Equation 2.17). Ten indentations were created for each glass with the strain rate jump test. Similar to the constant strain rate test, a few indentations were omitted from evaluation as they clearly did not probe homogeneous material. Therefore, the strain rate sensitivity was averaged over 8 to 10 indentations, depending on the sample. The errorbars show the standard deviation.

4

Results and discussion

4.1 Assessment of sample quality

Amorphous state, composition and homogeneity Besides the risk of crystallisation, phosphate-containing glasses may show phase separation if phosphate attracts too much sodium [185]. In this study, no signs of crystallisation or phase separation were found by means of XRD, light microscopy, visible light laser scattering (532 nm and 640 - 660 nm laser pointers) and TEM including electron diffraction. The glasses are therefore assumed to be fully amorphous and non phase-separated.
Compositional deviations from nominal level were small, as verified by EDX analysis (Table 4.1). The SiO_2 content was decreased and the Al_2O_3 content increased by less than 2 mol% compared to the nominal composition for all samples. This amount of Al_2O_3 incorporation is less than for silicophosphate glasses, which have been found to incorporate 3 to >9 mol% Al_2O_3 [66, 167, 188]. This difference may be explained by the high melt viscosity of the present glasses. The P_2O_5 content was found to be up to 1 mol% smaller than the nominal one. This may be attributed to minor P_2O_5 evaporation during melting [66, 188]. The rather small P_2O_5 losses confirm a previous

Table 4.1: Comparison of nominal glass composition in mol% with composition from EDX analysis (in brackets).

Glass	SiO_2	P_2O_5	Al_2O_3	Na_2O
Si70P0	70 (68.2 ± 1.6)	- (-)	15 (15.9 ± 1.2)	15 (15.9 ± 0.4)
Si70P7.5	70 (68.7 ± 0.7)	7.5 (6.9 ± 0.8)	11.25 (12.2 ± 1.0)	11.25 (12.2 ± 0.7)
Si60P0	60 (57.8 ± 2.0)	- (-)	20 (20.8 ± 1.0)	20 (21.4 ± 1.6)
Si60P2.5	60 (59.1 ± 1.2)	2.5 (1.6 ± 1.0)	18.75 (19.8 ± 1.3)	18.75 (19.5 ± 0.4)
Si60P5	60 (59.4 ± 1.7)	5 (4.1 ± 0.1)	17.5 (18.8 ± 1.8)	17.5 (17.7 ± 0.9)
Si60P6.25	60 (59.2 ± 1.1)	6.25 (5.4 ± 0.6)	16.875 (18.1 ± 1.4)	16.875 (17.2 ± 0.7)
Si60P7.5	60 (58.3 ± 1.2)	7.5 (6.8 ± 0.7)	16.25 (17.1 ± 1.4)	16.25 (17.8 ± 0.7)
Si55.5P7.5	55.5 (54.4 ± 1.2)	7.5 (6.6 ± 0.8)	18.5 (20.1 ± 1.4)	18.5 (19.0 ± 0.6)
Si50P0	50 (48.1 ± 1.7)	- (-)	25 (26.2 ± 1.4)	25 (25.6 ± 0.7)
Si50P7.5	50 (48.7 ± 1.4)	7.5 (6.6 ± 0.7)	21.25 (22.4 ± 1.6)	21.25 (22.3 ± 0.6)

finding that P_2O_5 is not likely to leave melts of metaluminous composition [119].
Unfortunately, the samples contained bubbles, owing to high melt viscosity resulting from high polymerisation. Bubbles may disturb the infrared reflection and mechanical experiments. Removal of bubbles would require an increase of the batch size and a significant increase of the melting time, to allow for homogenisation in spite of high viscosity. However, this would lead to further Al_2O_3 leaching from the crucibles and was therefore not pursued.

Table 4.2: Water content of the studied glasses in mol% and wt%.

Sample	mol% ($H_2O + OH$)	wt% ($H_2O + OH$)
Si70P0	0.098 ± 0.019	0.026 ± 0.005
Si70P7.5	0.048 ± 0.015	0.012 ± 0.004
Si60P0	0.070 ± 0.016	0.018 ± 0.004
Si60P2.5	0.080 ± 0.017	0.020 ± 0.005
Si60P5	0.047 ± 0.015	0.012 ± 0.004
Si60P6.25	0.059 ± 0.016	0.015 ± 0.004
Si60P7.5	0.068 ± 0.017	0.017 ± 0.004
Si55.5P7.5	0.050 ± 0.015	0.012 ± 0.004
Si50P0	0.059 ± 0.015	0.015 ± 0.004
Si50P7.5	0.043 ± 0.014	0.010 ± 0.003

Water content Structural water is known to be often present in glasses and it is typically introduced by water-bearing precursors such as $Al(OH)_3$ and hygroscopic $NaPO_3$ [93, 167, 213]. Furthermore, phosphate is known to increase the solubility of water in aluminosilicate melts [119]. Water may decrease glass polymerisation, see e.g. ref. [138] and p. 436 of ref. [149]. However, the water content (combined amounts of molecular H_2O and OH groups) was found to be very low, typically below 0.1 mol% (Table 4.2). Therefore, water will not significantly affect polymerisation and can be omitted from further structural considerations in this thesis.

4.2 Density and related properties

Density and packing density decreased while molar volume and oxygen packing density increased with increasing P_2O_5 content and constant SiO_2 content (Figure 4.1, left column).[14] For increasing silica content and constant phosphate content of either 0 or 7.5 mol% the density and packing density decreased and the oxygen packing density increased (Figure 4.1, right column). For phosphate-free glasses the decrease in packing density was within the error limit at lower silica contents. Also, at 50 mol% SiO_2, the incorporation of P_2O_5 did not noticeably change the packing density. The molar

[14] For glass properties that are presented in graphical form throughout this thesis, tabulated values are provided in the appendix.

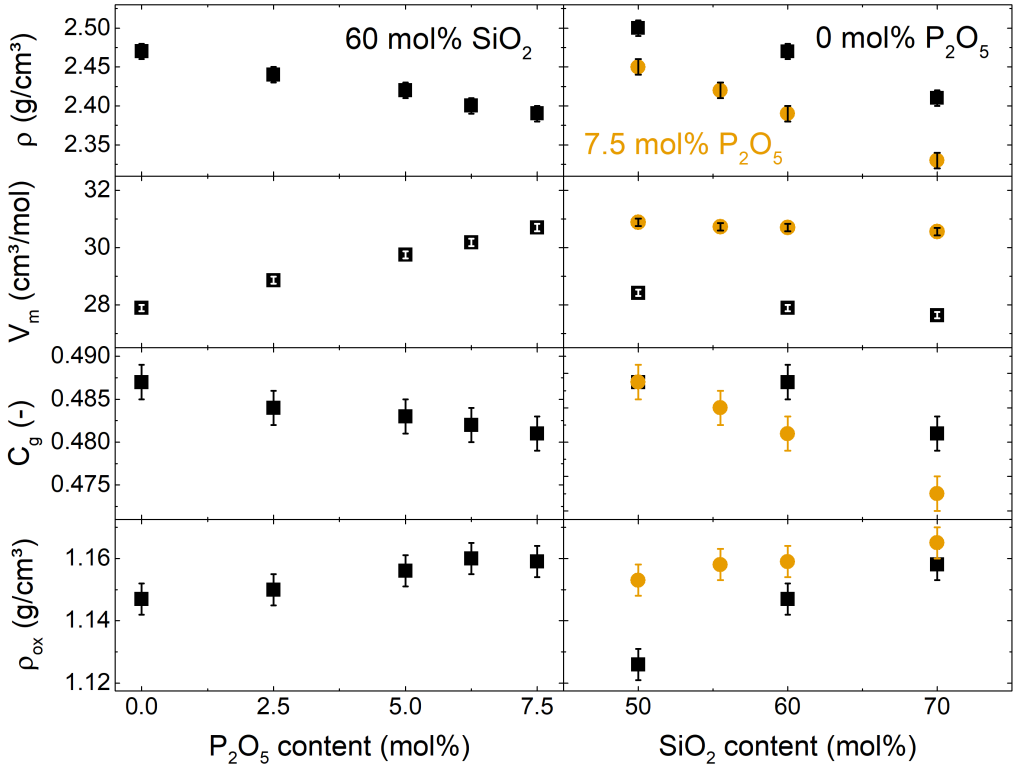

Figure 4.1: Overview of density, ρ, molar volume, V_m, packing density, C_g, and oxygen packing density, ρ_{ox} (top line to bottom line). (Left column) Change upon increasing P_2O_5 content for glasses with constant 60 mol% SiO_2. (Right column) Change upon increasing SiO_2 content for glasses with constant P_2O_5 content of either 0 mol% (black squares) or 7.5 mol% (orange circles).

volume only slightly decreased with increasing SiO_2 content and remained almost constant for glasses with 7.5 mol% P_2O_5.
The decreasing density and packing density with increasing phosphate content may be explained by the substitution of P_2O_5 for $NaAlO_2$, i.e. the substitution of two phosphate tetrahedra for one aluminate tetrahedron. The aluminate tetrahedra here all are assumed to have four BO, while phosphate tetrahedra may bear fewer BO. Even if the phosphate groups would assume Q^4_P state by forming Al-O-P bonds this would liberate Na^+ ions that formerly were needed to charge-balance the involved aluminate tetrahedra and which would now create new NBO elsewhere. This means that the substitution of P_2O_5 for $NaAlO_2$ introduces more tetrahedral units per mol but reduces the average number of BO per tetrahedron to below four. An increasing phosphate content therefore corresponds to a decreasing network polymerisation

in the studied glasses. A network with fewer cross-links and a larger number of tetrahedra per mol is likely to be less compact. This explains the decrease in density and packing density as well as the increase in molar volume with increasing phosphate content. A similar decrease in density has been observed in basaltic glasses [220].
For increasing silica content, silica tetrahedra (SiO_4) were substituted for aluminate tetrahedra ($Na^+[AlO_4]^-$). As both tetrahedral units bear four BO each, the overall network polymerisation is assumed to remain relatively constant. This is directly visible in the nearly constant molar volume. The decrease in density and packing density with increasing silica content is caused by the requirement for charge-balancing Na^+ ions in the vicinity of $[AlO_4]^-$ tetrahedra. Considering the similar ionic radii of Al^{3+} and Si^{4+} [198], their corresponding tetrahedra will also be of comparable size, but a network with more aluminate tetrahedra is likely to use more intertetrahedral space for the accommodation of sodium ions. Therefore, the density and packing density changed even though the molar volume remained roughly constant. The observation that C_g remained within the error limit for all glasses with 50 mol% SiO_2 and for the phosphate-free glass with 60 mol% SiO_2, even though ρ changed, is attributed to the C_g model assumption of densely packed spheres. This model depends on the choice of ionic radius[15] and does not take the directional bonds and NBO into account that may occur in the studied glasses.
The trend observed for oxygen packing density was opposite to that for density (Figure 4.1). This is counter-intuitive for oxide glasses with oxygen as the most abundant element. The concept of oxygen packing density, i.e. the mass of oxygen in a defined volume of glass, has been introduced by Ray [176], who pointed out its usefulness for weakly polymerised alkali silicate glasses with alkaline ions acting as network modifier. The glasses studied in this thesis, however, are highly polymerised, and sodium ions take a charge-balancing role rather than a modifying one. The calculation of ρ_{ox} (Equation 3.3) is based on the assumption of densely packed spheres and does not take the directional, covalent character of the oxygen bridging bonding into account. Recently, the oxygen packing density has been shown to correlate with the coordination number of the network-forming cations in phosphate-free aluminosilicate melts, see ref. [255] and p. 361 of ref. [101]. However, the network formers in the glasses of the present study did not change their coordination number (see NMR analysis in Section 4.5). The dependence of oxygen packing density on stoichiometric numbers appears to be a disadvantage in the presence of three different network forming oxides, all of

[15] Here, effective ionic radii from ref. [198] were used.

them with different stoichiometric numbers of oxygen. Therefore, the oxygen packing density will not be taken into account in further analyses here. Among the properties derived from density, the molar volume appeared to be the most suitable for arguments concerning network polymerisation.
The decreasing density in the three studied glass series coincided with a decreasing degree of ionic bonding (Section 4.7). A change in type of chemical bonds comes with a change in bond force constants, which will also affect bond lengths and, thus, potentially density as well. However, Taylor and Brown showed that bond length has no major influence on density. They have investigated metaluminous glasses similar to the phosphate-free glasses studied here by X-ray scattering [221, 222]. For increasing silica content and thus decreasing density they observed a decreasing T-O bond length (T = Si, Al) and increasing intertetrahedral bond angle. If bond length had a major influence on density, then a decreasing bond length should lead to a density increase rather than a decrease. Instead, density seems to be affected more by the intertetrahedral bond angle.

4.3 Thermal analysis

4.3.1 Glass transition temperature

Incorporation of phosphate led to a strong, roughly linear decrease in T_g (Figure 4.2a). From 0 to 7.5 mol% P_2O_5 the decrease in T_g ranged from 80 K for glasses with 50 mol% SiO_2 to > 120 K for glasses with 70 mol% SiO_2 (Figure 4.2b). By contrast, changes in T_g for varying silica content were small (~ 30 K). For increasing silica content (Figure 4.2b), T_g of phosphate-free glasses slightly increased while there was a decrease for glasses with 7.5 mol% P_2O_5.
The observed decrease in T_g with increasing P_2O_5 content is an indicator that phosphate addition reduces the network polymerisation of aluminosilicate glasses. This is reasonable as phosphate groups with $Q_P^{i\leqslant 3}$ bear fewer BO than silicate or aluminate tetrahedra of metaluminous glasses. Even Q_P^4 units require charge-stabilising Al-O-P bonds, thus liberating Na^+ ions that may depolymerise the network elsewhere. The marked influence of phosphate on characteristic temperatures of aluminosilicate glass has also been noted by Wyllie and Tuttle [250] who have found a strong decrease of the solidus

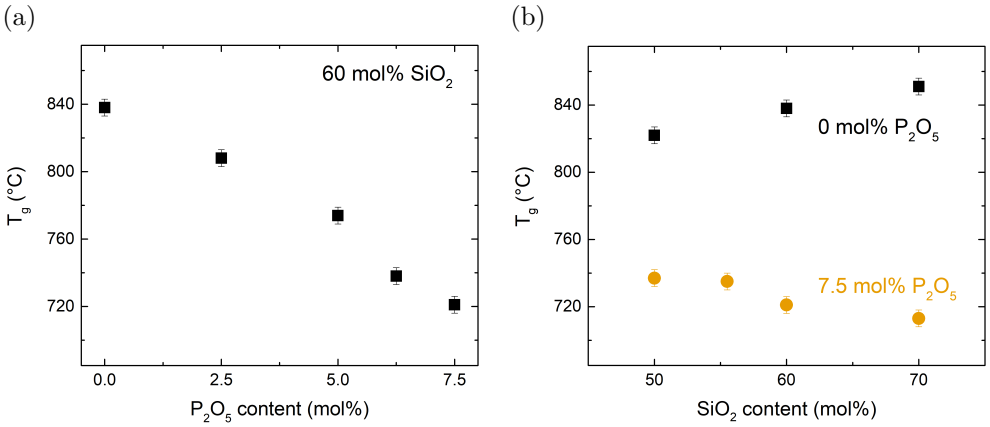

Figure 4.2: Dependence of glass transition temperature on glass composition. (a) Increasing P_2O_5 content and constant 60 mol% SiO_2. (b) Increasing SiO_2 content and constant P_2O_5 contents of 0 mol% (black squares) and 7.5 mol% (orange circles).

temperature of metaluminous albite glass upon incorporation of P_2O_5.
The much smaller changes of T_g with increasing SiO_2 content (Figure 4.2b) may be explained by the constant polymerisation expected for substitution of SiO_4 for $Na^+[AlO_4]^-$ tetrahedra. The small increase in T_g with increasing SiO_2 content in phosphate-free glasses may be explained by an increasingly covalent character of chemical bonds as the amount of Na^+ and Al^{3+} is reduced. This should increase the strength of bridging oxygen bonds and thus have a contribution to glass transition temperature even though polymerisation did not change [176, 181]. T_g seems to approach the value for vitreous silica, 1120°C [114].
In the literature, glass transition temperatures found for compositions similar to the phosphate-free glasses here were roughly comparable to the reported values, but usually lower by up to several tens of degrees [11, 15, 26, 160, 239]. There was no good agreement between the references, however. For example, reported T_g values for glass Si50P0 ranged from 725°C [160] to 800°C [239]. In the present study, a value of 822°C was found. This may be partially caused by faster quenching rates applied in those references.
Surprisingly, the T_g of glasses with 7.5 mol% P_2O_5 did not approach the T_g of vitreous SiO_2 but slightly decreased instead. Apparently the presence of phosphate as third network former had an additional influence on T_g when varying the silica content. Possibly, the assumption of constant network polymerisation is no longer correct in the presence of phosphate. This is discussed in Section 4.6.4 together with the results of far-infrared spectroscopy.

4.3.2 Crystallisation behaviour

Figure 4.3a shows a comparison of the DTA signals for three glasses with 0, 5 or 7.5 mol% P_2O_5 and constant 60 mol% SiO_2. The decreasing T_g with increasing phosphate content is highlighted by a dashed line, as is the crystallisation temperature, T_x, at the exothermal maximum of the crystallisation peak. Such a peak was only detected for the phosphate-free glass and is located between 1100 and 1250°C, followed by a melting endotherm above 1250°C.
Another broad and weak exothermal signal was found at temperatures slightly above glass transition, and below crystallisation (if observed). This broad exothermal signal is believed to show either the release of residual stresses or the sintering of glass powder. Numbers shown in that region in Figure 4.3a may thus correspond to a sintering temperature. In order

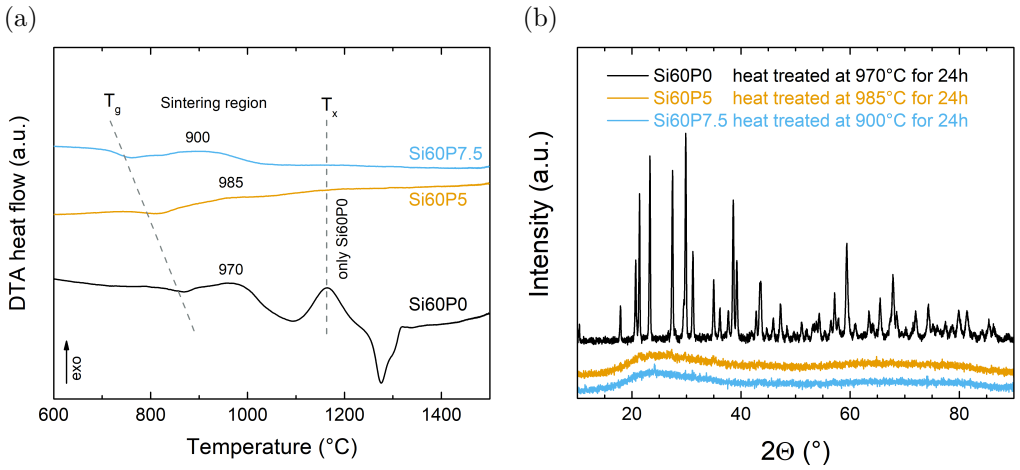

Figure 4.3: (a) Differential thermal analysis of selected glasses with 60 mol% SiO_2 and phosphate contents of 0 (black), 5 (orange) and 7.5 mol% (blue). Exothermal signals point upwards. Glass transition temperature T_g and crystallisation temperature T_x are marked by dashed lines. Only the phosphate-free glass crystallised. The weak, broad exothermal signal between T_g and T_x corresponds to sintering of the analysed powders. (b) X-ray analysis of the same glasses after 24 hours of heat treatment at the sintering temperatures indicated in (a). Signals were vertically shifted for easier comparison.

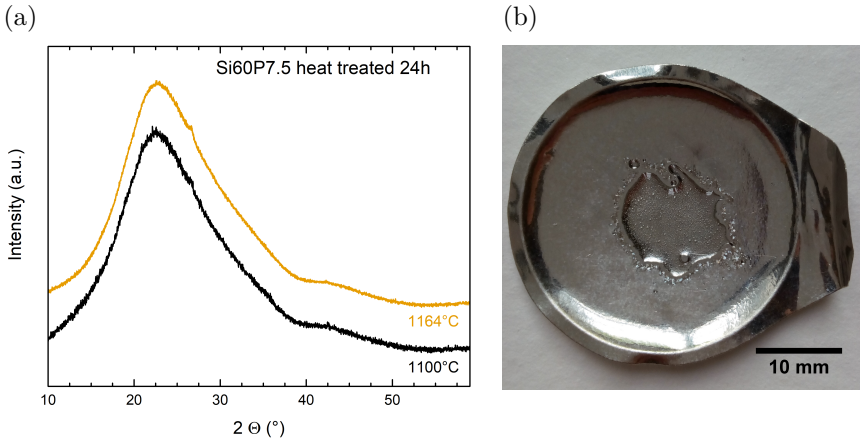

Figure 4.4: (a) X-ray analysis of glass Si60P7.5, heat treated for 24 h at indicated temperatures. Signals were vertically shifted for easier comparison. (b) After 24 h at 1100°C, the powder has fused into a transparent glass with no signs of crystallinity. Spots in the glass are bubbles.

to investigate whether those DTA sintering maxima may also contain signals from crystallisation, powder samples of the selected glasses were heat treated at the temperatures indicated in Figure 4.3b for 24 hours. After heat treatment, the phosphate-free sample looked opaque, while the phosphate-containing samples had fused into clear, transparent glass bodies. The samples were ground again and subjected to X-ray diffraction analysis (Figure 4.3b). No crystallisation was found for the phosphate-containing glasses, while the phosphate-free glass had clearly crystallised during the heat treatment. This result led to the conclusion that the term *sintering region* for the broad exothermal DTA signal was justified. In the case of phosphate-free glasses, however, a crystallisation maximum may well be present underneath the sintering signal.

To crystallise a phosphate-containing glass, two powder samples of glass Si60P7.5 were heat treated at 1164 and 1100°C, respectively, for 24 hours. These were the temperatures of the maximum and the onset of the crystallisation peak of the corresponding phosphate-free glass. Based on crystallisation kinetics, see e.g. p. 35 of ref. [154], these two temperatures were taken as estimates of the temperatures of high rate of crystal growth (1164°C) and high crystal nucleation rate (1100°C). They were selected to provoke crystallisation within short time, assuming that a crystal similar to the one in the phosphate-free sample would be created. However, an X-ray diffraction analysis showed that the samples were still amorphous after 24 hour heat

treatment (Figure 4.4a). The X-ray diffraction patterns showed a first hint towards a crystalline peak at $2\Theta \approx 26^{\circ}$, barely exceeding noise level. The glass powder had fused into a transparent glass body during the 24 hour heat treatment (Figure 4.4b). Apparent spots in that glass body were not crystals but bubbles.

The significantly reduced crystallisation tendency in phosphate-containing glasses bears interesting technological implications. Usually, aluminosilicate glasses have favourable mechanical properties [11, 181] but crystallise easily. Phospho-aluminosilicate glasses may combine a low crystallisation tendency with mechanical properties that are still close to those of phosphate-free metaluminous aluminosilicate glasses. Applications of interest may be high temperature glass soldering or 3D printing of glasses [103].

The low crystallisation tendency of the phosphate-containing glasses may also give insight into the glass structure: Formation of crystal nuclei requires local rearrangement of atoms; this rearrangement is apparently hindered by the presence of phosphate. The new interactions upon incorporation of phosphate appear to reduce the mobility of the other elements. Potentially, this is caused by the phosphate binding to both Na^+ and Al^{3+} for charge-balancing. Another reason may be an increase in entropy upon P_2O_5 incorporation.

A similar effect of crystallisation being inhibited by phosphate has been found by Ray and Day [175] for glasses of the composition Na_2O - 2 CaO - 3 SiO_2 to which they added 2 wt% P_2O_5, resulting in a shift of the DTA crystallisation to higher temperatures accompanied by a reduced peak intensity. Furthermore, Glatz et al. have recently published an investigation of the crystallisation in lithium aluminosilicate glasses upon addition of up to 1 mol% P_2O_5 [65]. For low Al/Li ratios they have found that phosphate promotes the nucleation of crystals by enrichment of Li around phosphate. For an Al/Li ratio closer to the metaluminous composition ($Al/Li \geq 0.7$), they have described phosphate as crystallisation inhibitor, owing to Al-O-P bonds connecting the phosphate to the rest of the network. This matches with the effect of phosphate on crystallisation observed in the present study. The discussion of spectroscopic results (Sections 4.5 and 4.6) shows that both the formation of Al-O-P bonds and the association of phosphate with sodium occurred here. However, enrichment of Na around phosphate was apparently not strong enough to cause phase separation or crystallisation. One reason for this may be the increased ionic radius of Na^+ compared to Li^+ ions [198], making Na^+ ions less mobile.

The crystallisation behaviour of phosphate-free glasses varied with silica content (Figure 4.5). The glass with 50 mol% SiO_2 showed a strong crystallisation peak between 900 and 1000°C, followed by a melting endotherm above 1400°C, of which only the onset was within the temperature limit of the

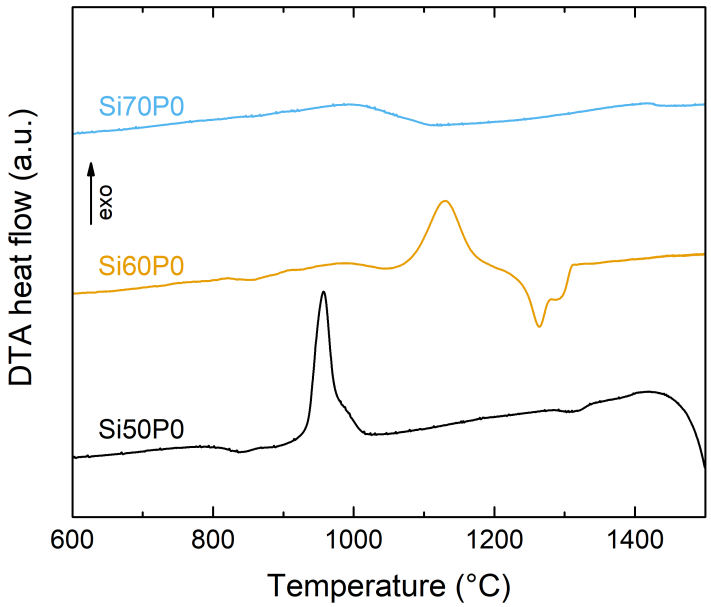

Figure 4.5: Differential thermal analysis of phosphate-free glass powders (particle size $< 38\,\mu$m) with 50 (black), 60 (orange) and 70 mol% SiO_2 (blue). Exothermal signals point upwards. Signals were vertically shifted for easier comparison. Intensity and position of the crystallisation peak changed with composition.

measurement. With an increase in silica content to 60 mol% the crystallisation peak lost intensity and shifted to higher temperature, while the melting endotherm shifted to lower temperature. For the glass with 70 mol% SiO_2, neither crystallisation peak nor melting endotherm were visible.
Lower silica contents correspond to substitution of $Na^+[AlO_4]^-$ for SiO_4 tetrahedra. This indicates a larger degree of ionic bonding, as shown in Section 4.7, which means a lower directionality of the chemical bonds and weaker force constants of individual bonds between cation and oxygen anion. For Na^+, the weaker bonds to oxygen may increase the ionic mobility and thus make the formation of crystal nuclei easier. This could explain why the DTA crystallisation peak was strongest for lower silica contents, and why it was found at lower temperatures.
To investigate whether crystallisation in phosphate-free glasses was surface or bulk crystallisation, a DTA experiment was performed on glass Si60P0 for three different particle sizes (Figure 4.6). The crystallisation peak and melting endotherm were clearly visible for the finest particle size. They were weaker for the medium particle size and no longer distinguishable for the large particle size. This indicates surface crystallisation, as for small particle sizes

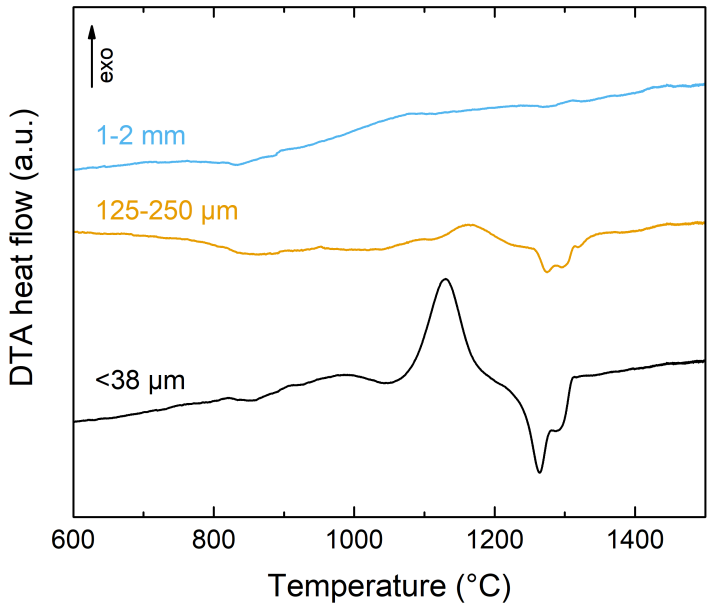

Figure 4.6: Differential thermal analysis of glass Si60P0 at a heating rate of 10 K/min for different sample particle sizes of $< 38\,\mu$m (black), 125 - 250 μm (orange) and 1 - 2 mm (blue). Exothermal signals point upwards. Signals were vertically shifted for easier comparison. Crystallisation peak and melting endotherm were visible for small particle size but became weaker with increasing particle size.

the surface to bulk ratio is much higher than for large particle sizes. Surface crystallisation has also been reported for lithium phospho-aluminosilicate glasses [65]. However, to conclusively get insight into the nucleation and crystallisation mechanism, further studies are necessary, which are beyond the scope of this thesis.

4.4 Refractive index

A typical, non-linear trend of the refractive index on wavelength [248] was visible for all glasses (Figure 4.7). Compositional trends were similar for all measured wavelengths and are shown for 632.8 nm in Figure 4.8. The refractive index decreased for the substitution of P_2O_5 for $NaAlO_2$ (Figure 4.8a) as well as for the substitution of SiO_4 for $Na^+[AlO_4]^-$ tetrahedra

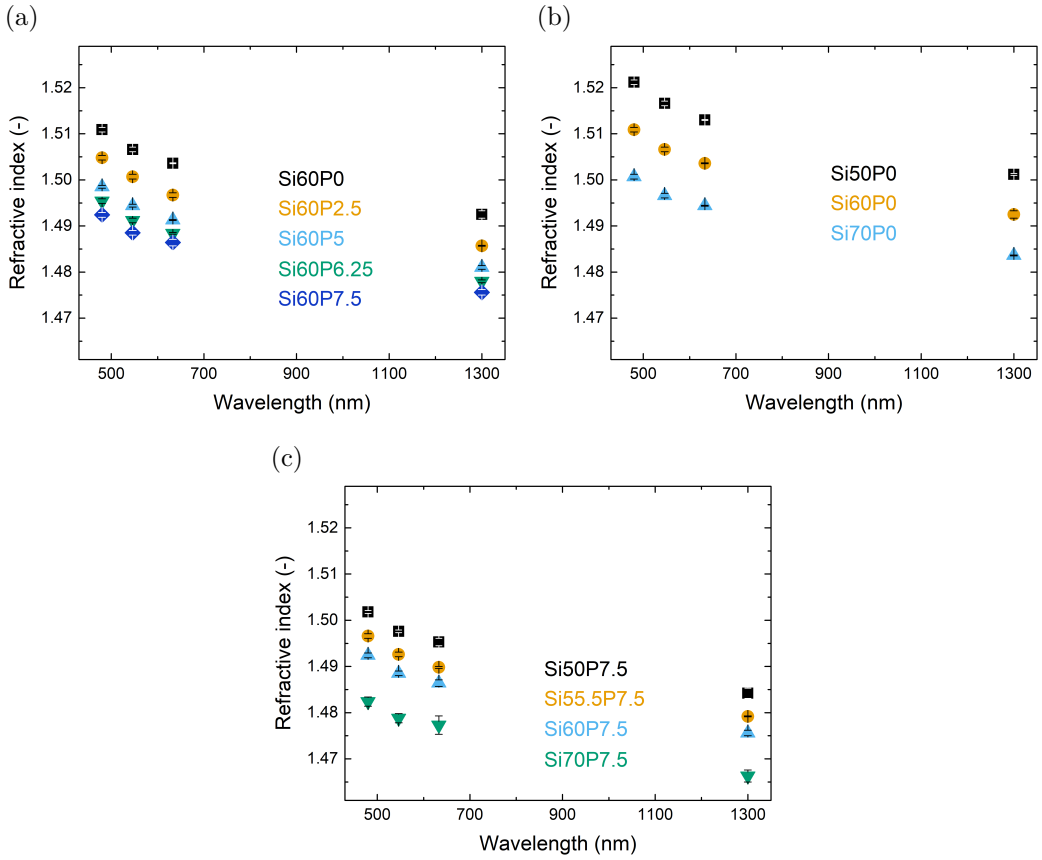

Figure 4.7: Dependence of the refractive index in the visible and near-infrared range on glass composition. (a) Increasing P_2O_5 content and constant 60 mol% SiO_2. (b) Increasing SiO_2 content and constant 0 mol% P_2O_5. (c) Increasing SiO_2 content and constant 7.5 mol% P_2O_5.

(Figure 4.8b). The decrease matched with the decreasing density trends for the same compositional changes. A decrease in density can be expected to cause a decrease in the average electron density of the glasses. This reduced electron density will subsequently affect the refractive index, as the principle of refraction is based on the interaction of light with the electrons of a glass, see e.g. p. 79 of ref. [69].

The decrease of refractive index with increasing silica content (Figures 4.7b, 4.7c and 4.8b) may also be explained in terms of glass composition. The refractive index approached the lower value for vitreous silica, which for the studied wavelengths ranges from 1.44 to 1.46 [248]. A similar decrease was found by Day et al. on metaluminous sodium aluminosilicate glasses, also

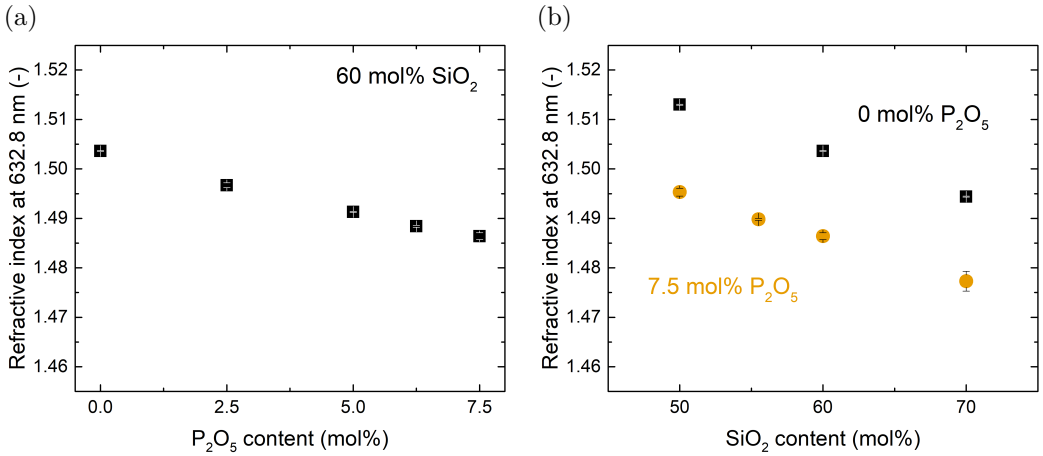

Figure 4.8: Dependence of the refractive index at 632.8 nm on glass composition. (a) Increasing P_2O_5 content and constant 60 mol% SiO_2. (b) Increasing SiO_2 content and constant P_2O_5 contents of 0 mol% (black squares) and 7.5 mol% (orange circles).

confirming the absolute refractive index values found here [32].
A composition-based explanation for the decreasing refractive index upon increasing phosphate content (Figures 4.7a and 4.8a) may be found in a study by DiGiovanni et al. who investigated the refractive index of glasses in the system SiO_2 - Al_2O_3 - P_2O_5 [37]. For constant SiO_2 content and Al/P ratio approaching unity, their refractive indices decreased to approach values close to those of vitreous silica. These conditions match the compositional trend of Figure 4.8a, despite the lack of sodium in their glasses. DiGiovanni et al. have ascribed the decreasing refractive index to the formation of Al-O-P bonds [37], with the resulting $AlPO_4$ units having the same structure and thus similar refractive properties as SiO_2. The formation of Al-O-P bonds is also likely for the glasses of the present study, as shown during the discussion of spectroscopic results.
A question remaining is whether metaphosphate groups which are not bound to aluminium may have a major contribution to the decreasing refractive index upon increasing phosphate content. The refractive index of pure sodium metaphosphate glass ($NaPO_3$) at 546.1 nm is 1.4859 [51], just below the value measured for glass Si60P7.5 (1.4885). Although metaphosphate may thus contribute to the decreasing refractive index, the value for $NaPO_3$ glass should be approached more slowly in the absence of other effects. The Al-O-P contribution is thus considered more dominant than metaphosphate.

4.5 Solid-state MAS NMR spectroscopy

This section focusses on one-dimensional MAS NMR results only. A multi-dimensional MAS NMR analysis was performed by a collaboration partner [161] and will not be discussed here. The chemical shifts and shapes of the peaks for the three nuclei ^{27}Al, ^{29}Si and ^{31}P only showed minor changes for variation of glass composition (Figures 4.9 to 4.11). They all shifted towards more negative ppm values both for increasing phosphate and silica content.

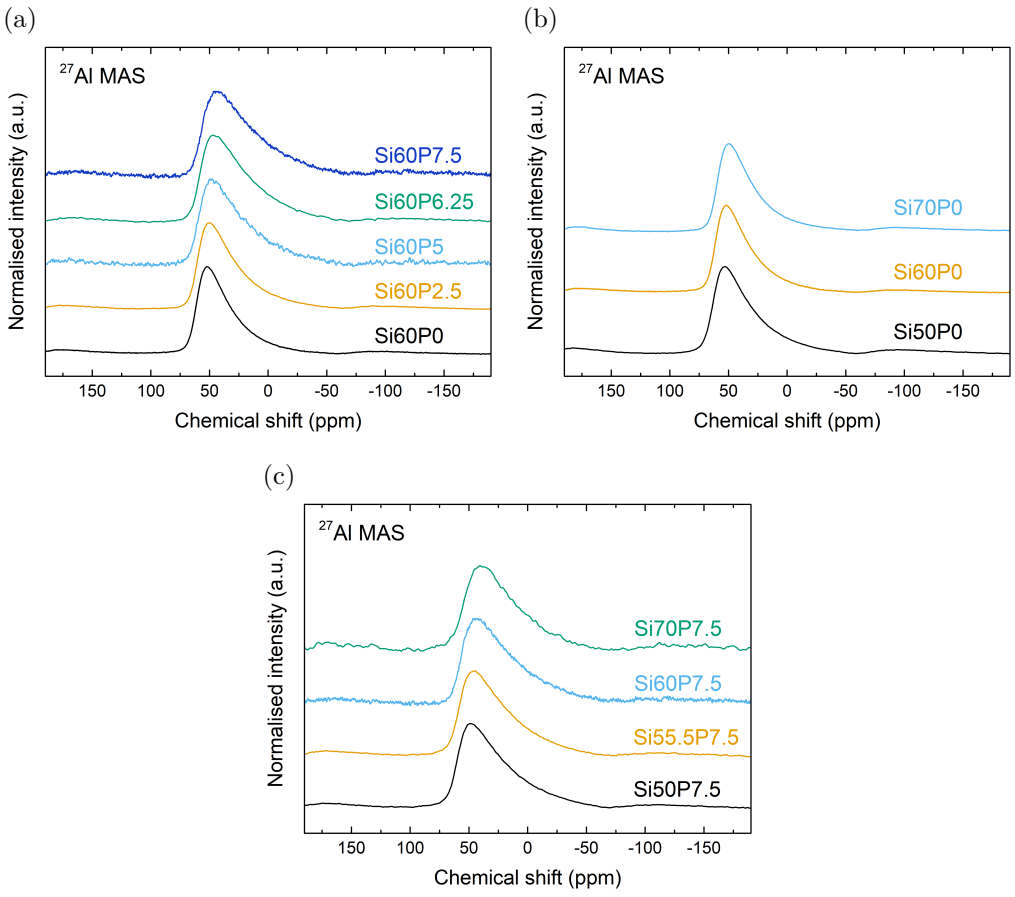

Figure 4.9: ^{27}Al MAS NMR spectra of the studied glasses. (a) Increasing P_2O_5 content and constant 60 mol% SiO_2. (b,c) Increasing SiO_2 content and constant P_2O_5 content of 0 (b) or 7.5 mol% (c). Signals were vertically shifted for easier comparison.

All ^{27}Al MAS NMR spectra displayed an asymmetric peak. This is caused by second order anisotropic effects of the quadrupolar ^{27}Al nucleus, see e.g. p. 321 of ref. [1]. The corresponding isotropic chemical shifts of ^{27}Al ranged from 65 to 55 ppm [161]. For increasing phosphate content the asymmetric shoulder of the peak increased in intensity (Figure 4.9a).
Chemical shifts were in the typical range for signals of four-coordinated aluminium, which is roughly centered at 60 ppm, see ref. [223] and p. 273 of ref. [125]. The asymmetric shoulder of the ^{27}Al MAS peak also covers regions that may be assigned to five- or six-coordinated aluminium, roughly from - 10 to + 30 ppm [3, 11, 223, 249]. MAS results alone could not exclude the presence of aluminium in coordination higher than four, but neither were such signals clearly distinguishable in the spectra. Even if five- or six-coordinated Al are present, the four-coordinated Al still is the predominant species here, thus contributing to the polymerisation of the network structure. The growth of the shoulder with increasing phosphate content could hint at an increasing fraction of higher-coordinated aluminium, but may also just reflect a larger diversity of the neighbouring atoms. The higher electron concentration of phosphate groups will have a chemical shielding effect on the ^{27}Al MAS signal, see also p. 273 of ref. [125]. This will cause a shift of the MAS NMR signal to more negative ppm values, giving rise to the shoulder.
More advanced experiments performed by a collaboration partner included multiple-quantum magic angle spinning (MQMAS), allowing to distinguish signals of higher-coordinated aluminium from the anisotropy shoulder [158, 249]. However, only four-coordinated aluminium was detected [161]. This indicated that changes of the peak anisotropy were not caused by Al in higher coordination but by increased diversity of neighbouring atoms owing to the phosphate incorporation. Based on these results we can conclude that here aluminium is present in fourfold coordination exclusively.

^{29}Si spectra had a low signal to noise ratio owing to the low natural abundance of the NMR-active ^{29}Si isotope, see e.g. p. 201 of ref. [125]. The isotropic chemical shifts of ^{29}Si ranged from -85 to -106 ppm. This range indicates fully polymerised silicate tetrahedra (Q^4_{Si}) [161]. Their signal would be expected at about - 110 ppm for pure vitreous silica, see p. 204 of [125]. The less negative signals obtained here are likely to be caused by the presence of aluminate tetrahedra connected to Q^4_{Si} groups, causing de-shielding of the ^{29}Si MAS signal [3]. In theory, the more positive chemical shifts found up to - 85 ppm could also indicate Q^3_{Si} groups, but in Al-free glasses only [27, 224]. In the presence of aluminium, Q^3_{Si} signals are typically shifted to ppm values even more positive than -85, which was not the case. This also agrees with the metaluminous composition of the glasses here.

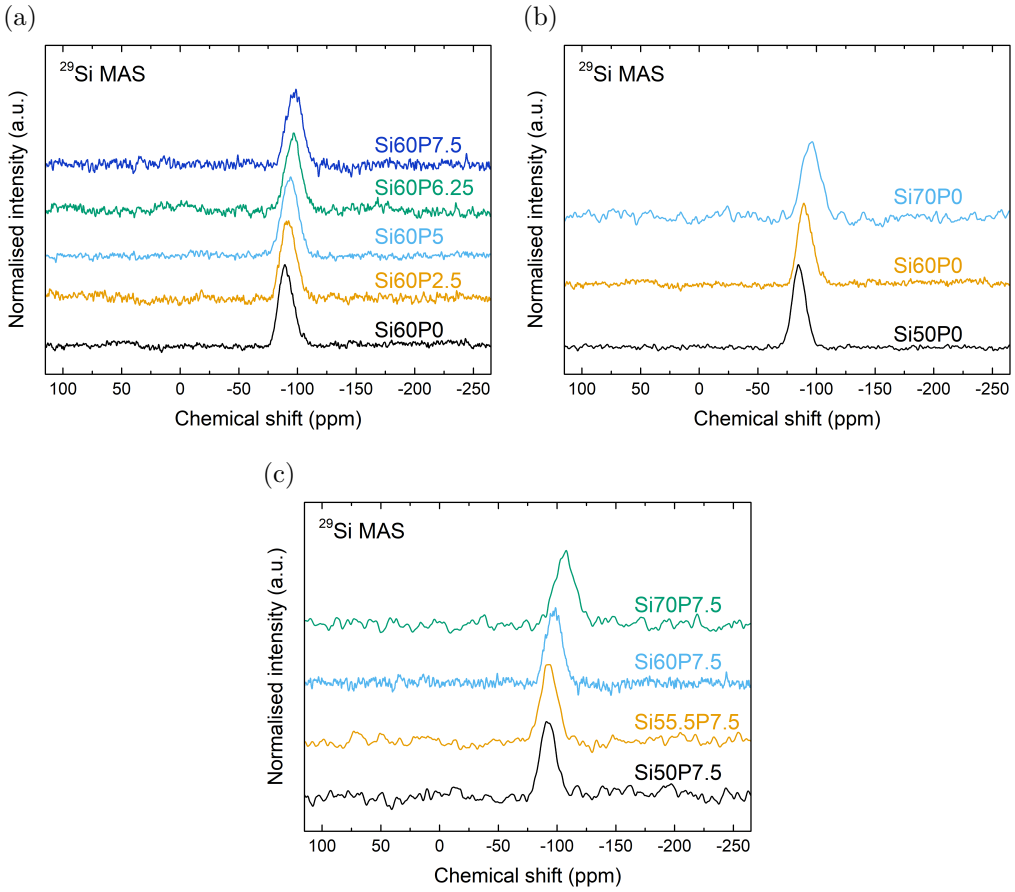

Figure 4.10: ^{29}Si MAS NMR spectra of the studied glasses. (a) Increasing P_2O_5 content and constant 60 mol% SiO_2. (b,c) Increasing SiO_2 content and constant P_2O_5 content of 0 (b) or 7.5 mol% (c). Signals were vertically shifted for easier comparison.

^{31}P peaks were slightly asymmetric. Their chemical shift maximum ranged from -10 to -16 ppm, indicating that phosphorus was present as Q^2_P groups [18]. Owing to the low phosphate contents of the studied glasses, less polymerised Q^1_P groups might also be expected. However, their corresponding MAS NMR signals at positive chemical shifts slightly above zero [18] could not be found. Still, the asymmetry of the ^{31}P MAS peaks indicates the presence of more than one chemical environment for phosphorus. The detailed analysis required a series of advanced 2D NMR experiments which are beyond the scope of this thesis and may be found in ref. [161]. The most important result of that analysis is that Q^2_P groups probably coexist with

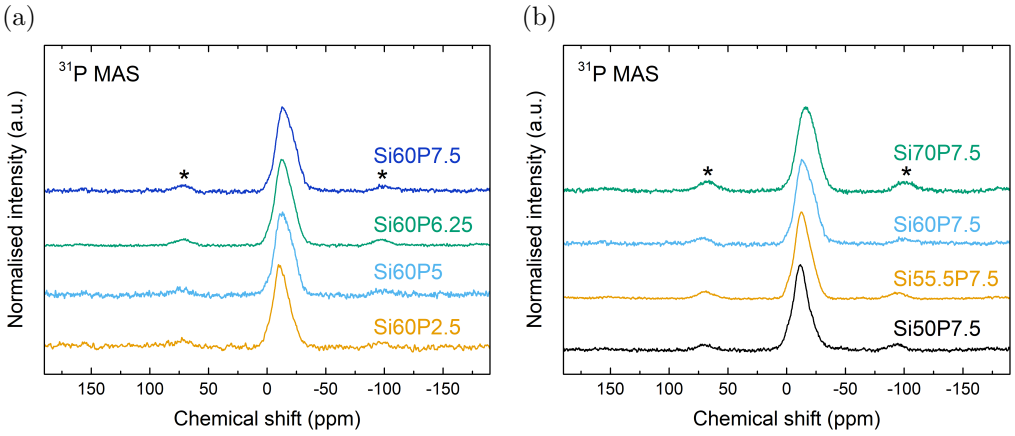

Figure 4.11: ^{31}P MAS NMR spectra of the studied glasses. (a) Increasing P_2O_5 content and constant 60 mol% SiO_2. (b) Increasing SiO_2 content and constant P_2O_5 content of 7.5 mol%. Asterisks (*) mark spinning side bands. Signals were vertically shifted for easier comparison.

$AlPO_4$ groups, i.e. Q^4_P groups like those found in the mineral berlinite. Additionally, a small contribution of Q^1_P groups ($<5\,\%$) could not be entirely excluded. The $AlPO_4$ groups are known to give rise to MAS signals at about - 25 ppm [62, 189], and their overlap with the Q^2_P signal causes the observed peak asymmetry. These findings are in agreement with the Raman results below which also could not clearly distinguish between metaphosphate and $AlPO_4$ units.

4.6 Vibrational spectroscopy

For a better overview, infrared spectra and VV and VH Raman spectra are presented together in Figures 4.12 to 4.14 for glasses with constant 60 mol% SiO_2, constant 0 mol% P_2O_5 and constant 7.5 mol% P_2O_5, respectively. Letters in the figures mark the identified bands. Most bands were common to all glasses. A summary is provided in Table 4.3.

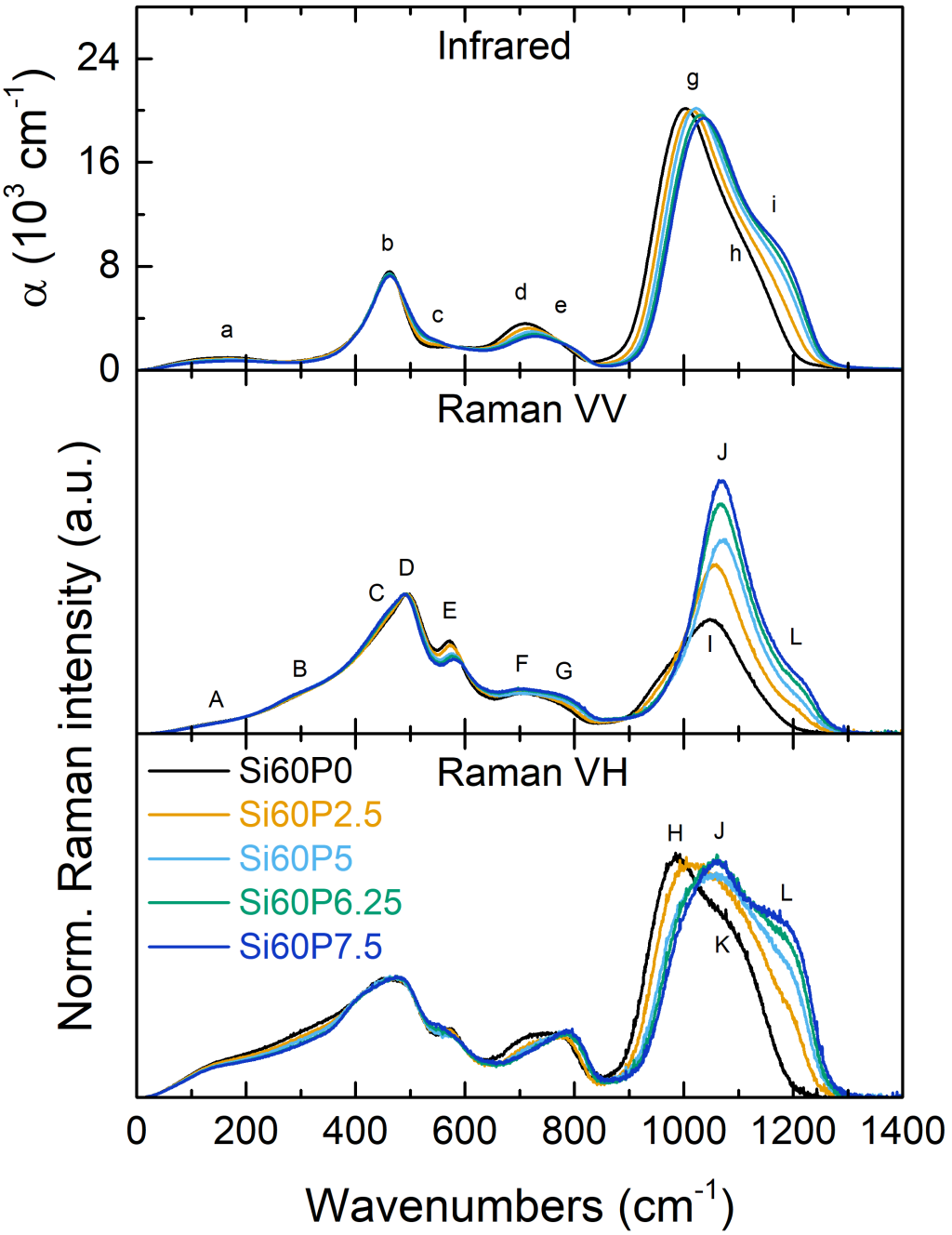

Figure 4.12: Infrared, Raman VV and Raman VH spectra (from top to bottom) for glasses with increasing P_2O_5 content and constant 60 mol% SiO_2. The letters mark identified bands. Band assignments are listed in Table 4.3 and discussed in Section 4.6.3.

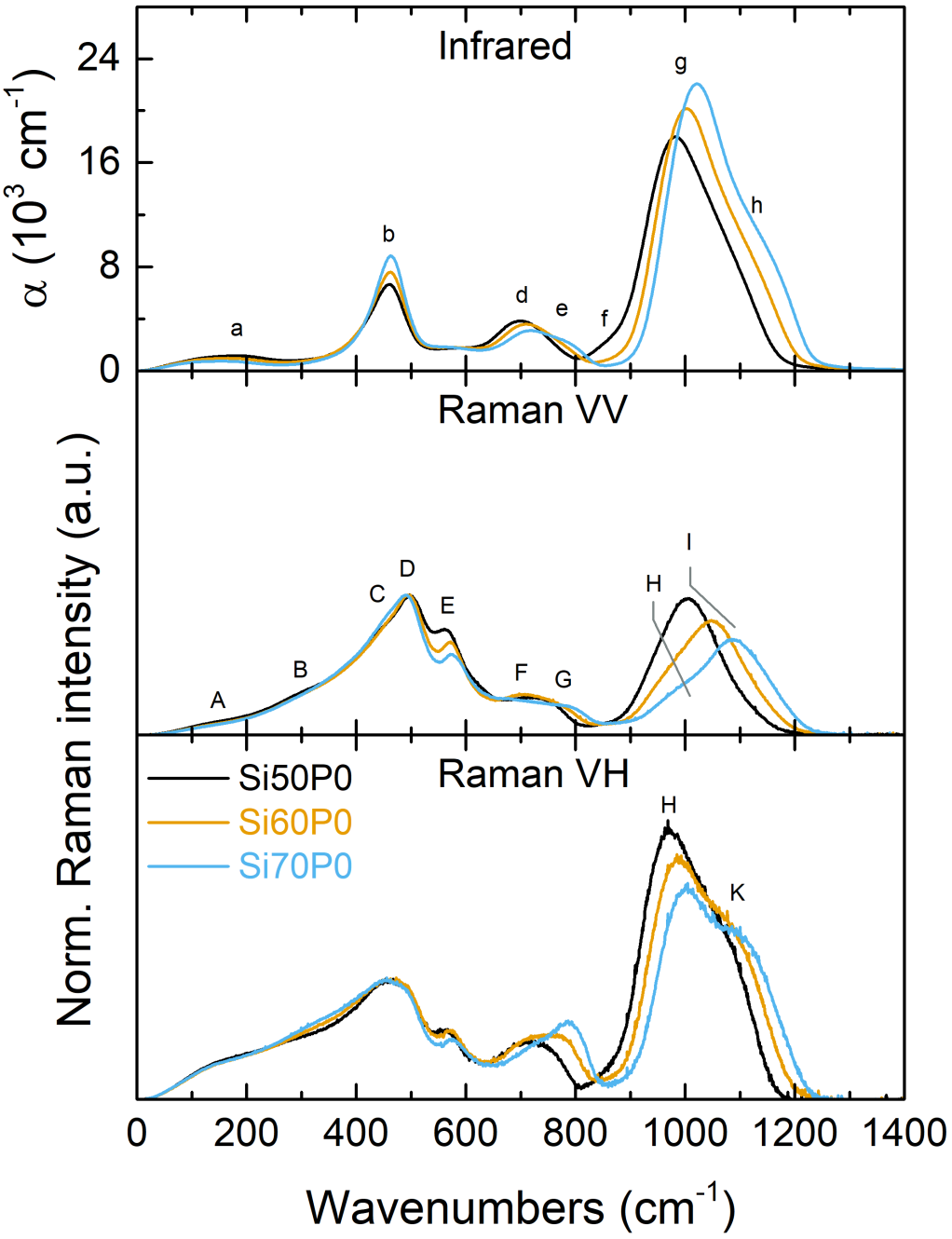

Figure 4.13: Infrared, Raman VV and Raman VH spectra (from top to bottom) for glasses with increasing SiO_2 content and constant 0 mol% P_2O_5. The letters mark identified bands. Band assignments are listed in Table 4.3 and discussed in Section 4.6.3.

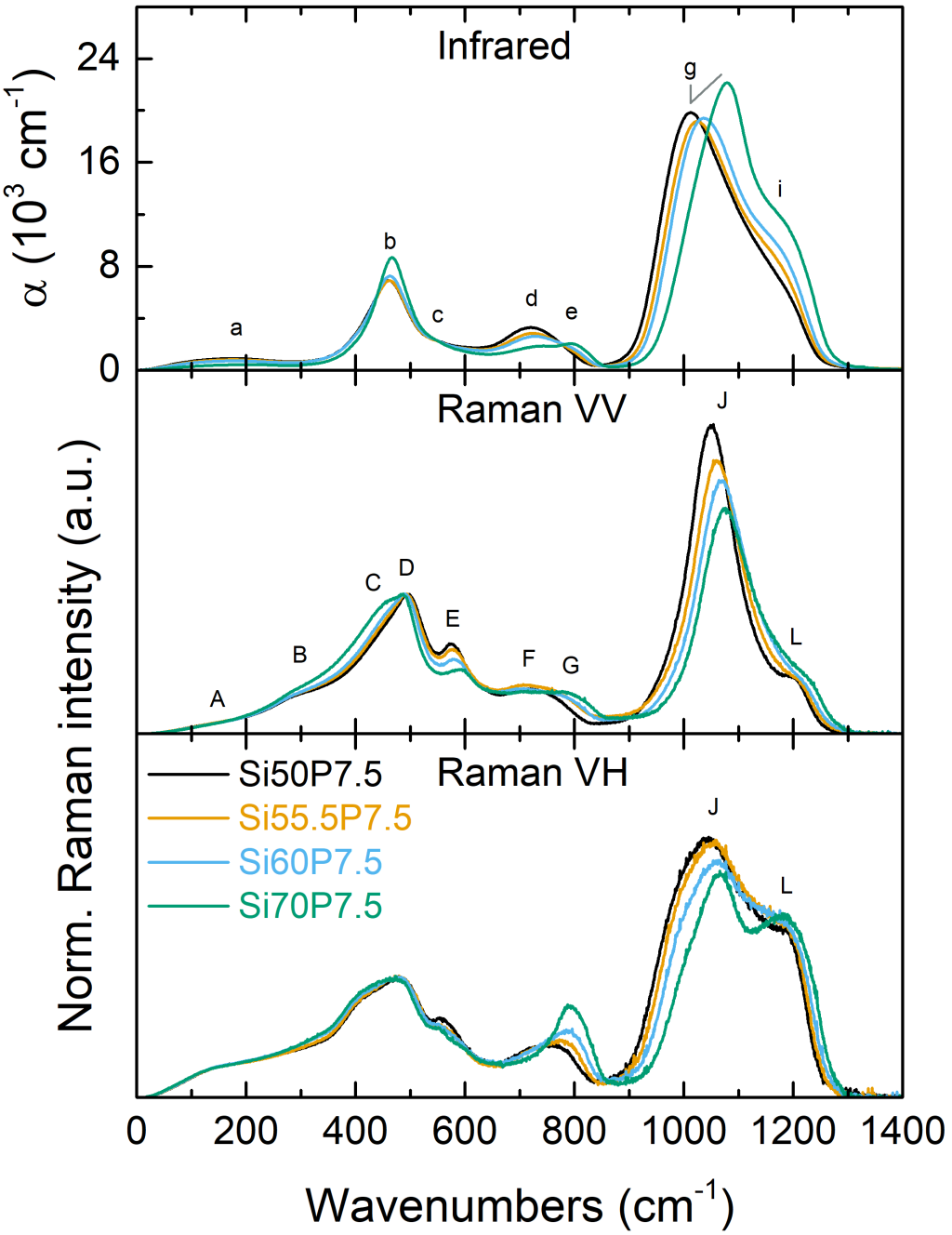

Figure 4.14: Infrared, Raman VV and Raman VH spectra (from top to bottom) for glasses with increasing SiO_2 content and constant 7.5 mol% P_2O_5. The letters mark identified bands. Band assignments are listed in Table 4.3 and discussed in Section 4.6.3.

Table 4.3: Overview of the IR and Raman band assignments. Wavenumber shifts of the bands are given for the three glass series with constant 60 mol% SiO_2, constant 0 mol% P_2O_5 and constant 7.5 mol% P_2O_5, respectively. All band shifts are summarised under *Total*. For details regarding assignments see text in Section 4.6.3.

Band	**Wavenumber range (cm^{-1})**				**Assignments**
	Total	60 mol% SiO_2	0 mol% P_2O_5	7.5 mol% P_2O_5	
Infrared					
a	**158-205**	166-182	182-158	174-205	Alkali cation (Na^+) in oxygen cage [82, 84, 139, 140, 234]
b	**460**	460	460	460	Si-O rocking [56, 79, 86, 95, 168] Si-O bending [30] Bending of $[AlO_4]^-$ tetrahedra [83] Al-O stretching [234]
c	**535-545***	535-540	-	540-545	P-O bending [234] Si-O-Al bonds with six-coordinated Al [32, 214]
d	**700**	700	700	700	Antisymmetric stretching of $[AlO_4]^-$ tetrahedra [83]
e	**780-800***	780	780	780-800	Si-O-Si bending [79, 83, 86, 247]
f	**860***‖	-	860‖	-	Stretching of $[AlO_4]^-$ tetrahedra [124, 212]
g	**982-1079**	1003-1037	982-1021	1013-1079	Q^4_{Si} antisymmetric stretching [75, 79, 86, 209]
h	**1100-1150***	1100-n.d.¶	1100-1150	n.d.	Q^4 units [75, 209]
i	**1130-1170***	1170	-	1130-1170	Antisymmetric P-O stretching in Q^2_P units [67, 100, 234]
Raman					
A	**85** §	85	85	85	Boson peak [4, 14, 129, 258]
B	**300***	300	300	300	Breathing of six-membered rings [94] Al-O stretching [234] P-O bending [234]
C	**460***	460	460	460	Six-membered rings of mixed SiO_4 and $[AlO_4]^-$ [49, 201]
D	**486-498**	496-490	498-490	496-486	Breathing of four-membered rings [200] T-O-T bending (T: tetrahedral centre) [155] Si-O-Al bridges [83, 135]
E	**562-593**	570-579	562-575	575-593	Breathing of three-membered rings [132]
F	**700**	700	700	700	Stretching of $[AlO_4]^-$ tetrahedra [76, 83, 134]
G	**760-790**†	780-790	760-785	775-790	Si-O-Si bending [83]
H	**970-1027**†	985-1027††	970-1000	n.d.	T_{2s} tetrahedral mode‡ [109, 135, 157, 160, 163]
I	**1005-1088**	1048-n.d.	1005-1088	n.d.	$Q^{4,low}_{Si/Al}$ tetrahedral mode‡‡ [109, 135, 157, 160, 163]
J	**1050-1076**	1056-1068	-	1050-1076	Q^2_P symmetric stretching [20, 67, 100, 167, 234, 251] Al-O-P bonds [62, 102, 144, 150] Q^1_P antisymmetric stretching [67, 234] Si-O-P bonds [24, 102, 144, 150, 203, 247]
K	**1040-1090***†	1070-n.d.	1040-1090	n.d.	$Q^{4,high}_{Si/Al}$ tetrahedral mode‡‡ [109, 135, 157, 160, 163]
L	**1195-1215***	1200-1215	-	1195-1210	Q^2_P antisymmetric stretching [20, 67, 100, 167, 234, 251] Al-O-P bonds [62, 102, 144, 150] Si-O-P bonds [24, 102, 144, 150, 203, 247]

* Higher error of band position ($\sim \pm 20\,cm^{-1}$), because only shoulders were available for determination.

‖ Only found for glass Si50P0.

¶ n.d.: Not distinguishable because band was hidden underneath phosphate-related bands.

§ Position of the Boson peak was determined prior to spectral reduction and thus appears shifted compared to the shoulder after reduction.

† Position determined from VH Raman spectra.

†† Position determined from spectra measured at 514 nm excitation instead of 488 nm. At 488 nm the band was not clearly distinguishable because of luminescence.

‡ Stretching of TO_4 tetrahedra with two O moving towards T and the other two O moving away from it.

‡‡ Stretching of $Q^4_{Si/Al}$ units with larger ($Q^{4,high}_{Si/Al}$) or smaller ($Q^{4,low}_{Si/Al}$) intertetrahedral angles.

4.6.1 Description of the infrared bands

Infrared bands of glasses with constant 60 mol% SiO_2 The IR spectra of the glasses with constant 60 mol% SiO_2 (Figure 4.12) can be split into four regions: (1.) The far-infrared (FIR) region below 300 cm^{-1}, (2.) the low frequency region from 300 to 650 cm^{-1}, (3.) the middle frequency region from 650 to 850 $cm^{-1}$and (4.) the high frequency region above 850 cm^{-1}. The FIR region (enlarged in Figure 4.15) contained one broad band (a).[16] Upon P_2O_5 incorporation and thus decreasing Al_2O_3 and Na_2O contents the intensity of this band decreased and its maximum[17] shifted from 166 to 182 cm^{-1}. The low frequency region was characterised by a band at 460 cm^{-1} (b). An additional shoulder emerged at 535 cm^{-1} (c) upon P_2O_5 addition and shifted to 540 cm^{-1} with increasing P_2O_5 content. The maximum of the middle frequency region at 700 cm^{-1} (d) decreased upon increasing P_2O_5 content while a shoulder at 780 cm^{-1} (e) gained intensity. The high frequency region contained the main infrared band (g). This band had its maximum at 1003 cm^{-1} for 0 mol% P_2O_5 which shifted to 1037 cm^{-1} with

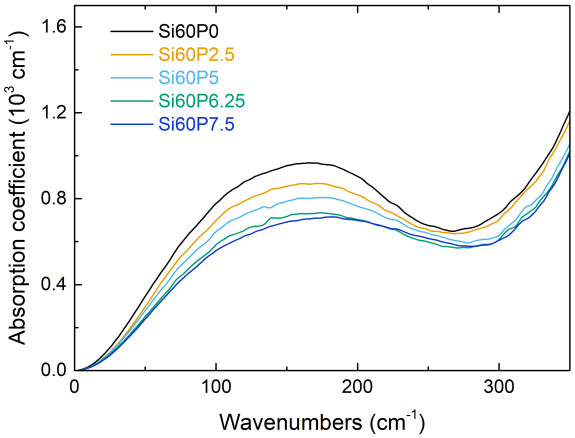

Figure 4.15: Enlarged FIR spectra for glasses with increasing P_2O_5 content and constant 60 mol% SiO_2.

[16] An overview of band letters is provided in Figures 4.12 to 4.14 and Table 4.3.

[17] As will be discussed in Section 4.6.4, the FIR band (a) is not a single band but a superposition of many bands which describe the manifold appearances of the environment surrounding Na^+. The shift of the FIR band maximum thus describes an averaged effective change in the Na^+ environment. Also, the FIR band partially overlaps with band b, which may contribute to the observed shift of band a. However, the contribution of band b to the shift is considered small as band b itself did not shift.

P_2O_5 content increasing up to 7.5 mol%. At the same time, the intensity of band g slightly decreased with increasing phosphate content, with the exception of the glass with 5 mol% P_2O_5 (Si60P5), which did not match the decreasing trend. At 1100 cm^{-1}, a shoulder (h) was visible for 0 mol% P_2O_5. Upon increasing P_2O_5 content, this shoulder either shifted towards higher wavenumbers or a new, phosphate-related band (i) appeared at $\sim$1170 cm^{-1} and gained intensity.

Infrared bands of glasses with constant 0 mol% P_2O_5 The bands observed for glasses with constant 0 mol% P_2O_5 (Figure 4.13) were similar to those of the glasses with constant 60 mol% SiO_2. For increasing SiO_2 content and thus decreasing Al_2O_3 and Na_2O contents the intensity of the FIR band a (enlarged in Figure 4.16) decreased and its maximum shifted from 182 to 158 cm^{-1}. Band b (460 cm^{-1}) gained intensity upon increasing silica content. A shift of band b to higher wavenumbers fell within the resolution limit (4 cm^{-1}) of the measurement. The envelope of bands d and e (650 - 800 cm^{-1}) shifted towards higher wavenumbers with increasing SiO_2 content, with band e gaining intensity compared to band d. The high frequency region above 800 cm^{-1} comprised the main band g, the shoulder h, and - only for glass Si50P0 - also a weak shoulder (f) at 860 cm^{-1}. Band g shifted from 982 to 1021 cm^{-1} and increased in intensity with increasing SiO_2 content. Furthermore, the shoulder h shifted from 1100 to 1150 cm^{-1}.

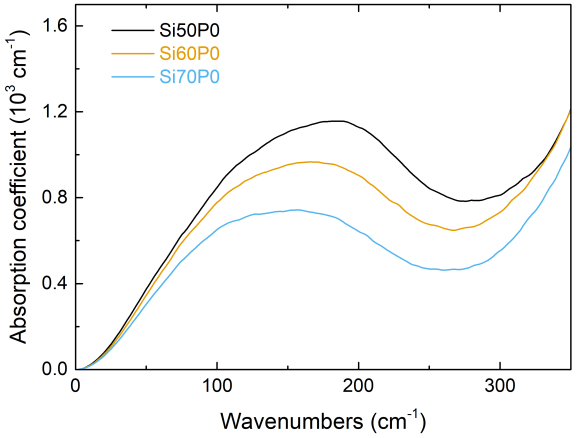

Figure 4.16: Enlarged FIR spectra for glasses with increasing SiO_2 content and constant 0 mol% P_2O_5.

Infrared bands of glasses with constant 7.5 mol% P_2O_5 Most band trends observed for glasses with 7.5 mol% P_2O_5 with increasing SiO_2 content (Figure 4.14) were similar to those for glasses with 0 mol% P_2O_5. One exception was the FIR band a (enlarged in Figure 4.17). Here, this band shifted from 174 to 205 cm^{-1}, while in case of the phosphate-free glasses the shift was in the opposite direction. Band b (460 cm^{-1}) gained intensity with increasing SiO_2 content and shifted towards higher wavenumbers, though almost remaining within the resolution limit. The strong intensity increase of band b from 60 to 70 mol% SiO_2 indicates a possible outlier for glass Si70P7.5. This composition showed a much larger concentration of bubbles which may have influenced the reflection experiment. The weak shoulder c was visible between 540 and 545 cm^{-1} for all glasses of this series. Band d (700 cm^{-1}) lost intensity with increasing silica content while band e gained intensity and shifted from 780 to 800 cm^{-1}. For 70 mol% SiO_2, band e became the new maximum of the middle frequency region. In the high frequency region, the band envelope consisted of the maximum g and the shoulder i. Band g shifted from 1013 to 1079 cm^{-1} with increasing SiO_2 content and shoulder i shifted from 1130 to 1170 cm^{-1}. While the intensity of shoulder i continuously increased with increasing SiO_2 content, the intensity of band g showed a possible outlier for 70 mol% SiO_2. This outlier, too, is likely to be caused by the higher concentration of bubbles in glass Si70P7.5.

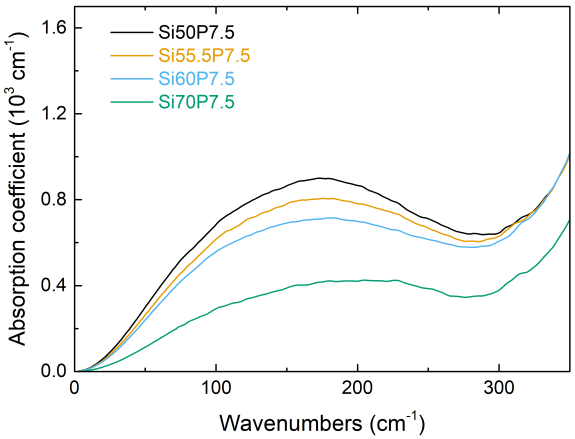

Figure 4.17: Enlarged FIR spectra for glasses with increasing SiO_2 content and constant 7.5 mol% P_2O_5.

4.6.2 Description of the Raman bands

Raman bands of glasses with constant 60 mol% SiO_2 After the Long reduction (Equation 3.4), the shape of the VV and VH Raman spectra resembled that of the infrared spectra (Figure 4.12). The Boson peak (A), which is typically observed in Raman spectra of glasses around 80 to 100 cm^{-1}, was reduced to a weak shoulder by the Long reduction.[18] It will not be analysed further in this thesis. The remaining part of the Raman spectra (Figures 4.12 to 4.14) can be divided into three regions: (1.) The low frequency region from 200 to 650 cm^{-1}, (2.) the middle frequency region from 650 to 850 cm^{-1} and (3.) the high frequency region above 850 cm^{-1}.

The low frequency region of all studied glasses was dominated by a band maximum at 490 cm^{-1} (D) and a second maximum of lower intensity at $\sim$570 cm^{-1} (E). For increasing P_2O_5 content, the dominant maximum D shifted from 496 to 490 cm^{-1} and the secondary maximum E shifted from 570 to 579 cm^{-1} while its intensity relative to band D decreased. Furthermore, the low frequency region had two weak shoulders at 300 (B) and 460 cm^{-1} (C) which both slightly increased in intensity with respect to band D upon increasing P_2O_5 content. However, the VH counterpart of band B decreased in intensity with increasing P_2O_5 content. The VH intensity of bands D and E with respect to the high frequency bands was lower than in the VV spectra. This shows that the bands D and E correspond to highly symmetric vibrations.

The middle frequency region consisted of a weak, broad band envelope with its maximum around 700 cm^{-1} (F) and a shoulder at 780 cm^{-1} (G). Upon increasing P_2O_5 content, the intensity of the shoulder G increased relative to the maximum F. In all VH spectra, the intensity of band G became higher than that of band F. Therefore, the vibration corresponding to band F must be more symmetric than the one corresponding to band G.

As regards the high frequency band envelope, the phosphate-free glass differed from the rest. Its high frequency envelope appeared as one broad, asymmetric band with a maximum (I) at 1048 cm^{-1}. The asymmetric shape suggests the presence of at least two additional bands underneath this main band. The presence of these two bands was supported by the VH spectrum showing a maximum (H) at 985 cm^{-1} and a shoulder (K) at 1070 cm^{-1}. The VV band maximum (I) did not appear in the VH spectrum and thus corresponds to vibrations that are more symmetric compared to those of the

[18] After Long reduction, the Boson peak also appeared shifted to higher wavenumbers slightly above 100 cm^{-1}. The value of 85 cm^{-1} in Table 4.3 was determined prior to Long reduction.

bands H and K.
Upon phosphate addition, two new bands appeared, one as a shoulder at 1200 cm^{-1} (L) and one becoming the new maximum of the high frequency envelope at 1056 cm^{-1} (J). For a further increase in phosphate content up to 7.5 mol%, the shoulder L shifted from 1200 to 1215 cm^{-1} and the maximum J shifted from 1056 to 1068 cm^{-1}. The shift of band J appeared to be linear. As an exception, glass Si60P5 showed an outlier towards a slightly higher frequency of band J. The outlier was, however, within the error limit. Band I of the phosphate-free glass could not be distinguished any more once a glass contained P_2O_5, meaning its intensity relative to that of the phosphate-related bands was too low.
The two phosphate-related bands J and L were also visible in the VH spectra. For glass Si60P2.5 they appeared as shoulders at 1060 and 1200 cm^{-1}, respectively. However, the assignment of the 1060 cm^{-1} VH band to vibration J was not unambiguous in spectra measured at 488 nm excitation because of minor luminescence overlapping with the high frequency region. The 1060 cm^{-1} VH band could also be linked to vibration K. To clarify this and to identify influence of luminescence, the high frequency VV and VH envelopes were compared for two different excitation wavelengths, 488 and 514 nm (Figure 4.18). The identified VH bands were marked in Figure 4.18 by their assigned letters (H, J, K, L). Vertical lines link the VV maximum J to the position where band J is to be expected in the VH spectra. The 514 nm spectra showed less influence of luminescence, thus their slightly differing shape. Bands H and J appeared to be affected the most by luminescence.
At 488 nm excitation for glass Si60P2.5 (Figure 4.18, left column, orange line), the phosphate-related band J seemed to coincide with the aluminosilicate band K. The VH maximum was still band H for glass Si60P2.5. However, band J became the VH maximum for higher phosphate contents, while the aluminosilicate bands H and K were no longer distinguishable. The assignment of the new maximum to band J instead of K was backed by the coincidence of its position with the VV band J (indicated by vertical lines in Figure 4.18). Both bands H and K should still be present in the phosphate-containing glasses, because their network was still mainly made up by SiO_4 and $Na^+[AlO_4]^-$ tetrahedra.
At 514 nm excitation (Figure 4.18, right column), the spectrum of Si60P2.5 clearly showed four bands: the maximum H and three shoulders assigned to J, K and L. The shoulder which had the same position as the VV maximum could be linked to band J (indicated by vertical lines in Figure 4.18). The shoulder situated between bands J and L could be correlated with band K. At 514 nm excitation, band J still increased in intensity with increasing phosphate content but did not dominate band H, probably because of lower

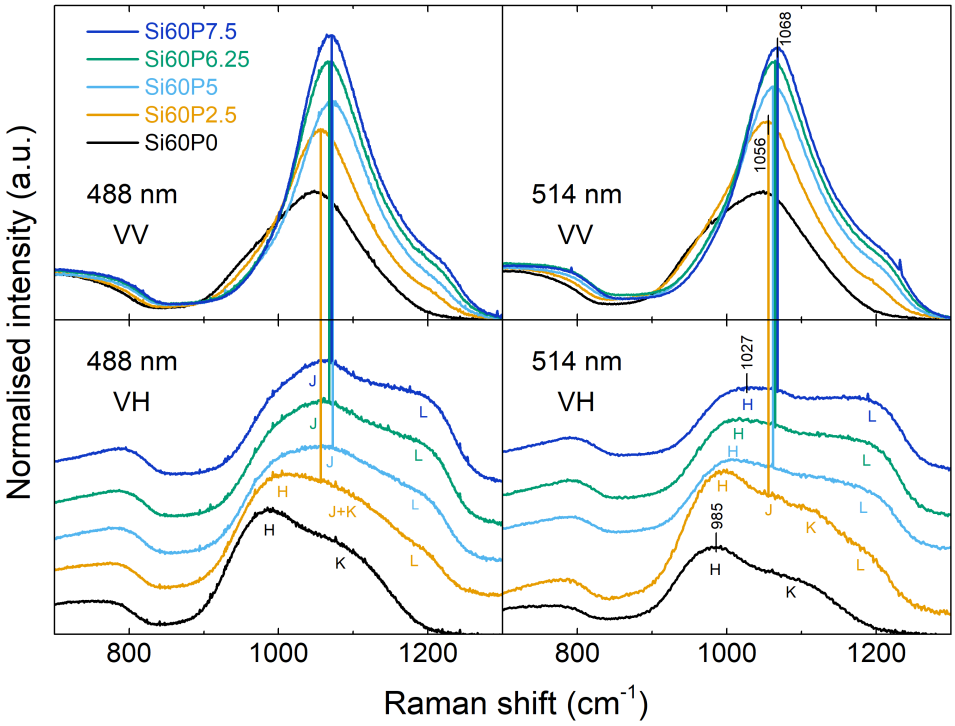

Figure 4.18: VV and VH high frequency Raman spectra (top and bottom line) of glasses with 60 mol% SiO_2 and increasing phosphate content, measured with 488 (left column) and 514 nm (right column) lasers. Differences in VH spectra are caused by luminescence at 488 nm excitation. VH spectra were vertically shifted for easier comparison. Vertical coloured lines indicate the position of band J in the VH spectra. Indicated band positions (right column) show that the phosphate band J shifted less than the aluminosilicate band H. The VH spectra of glass Si60P2.5 (orange line) hold the most information because the phosphate lines J and L were still too weak to dominate the spectra.

luminescence when compared to 488 nm excitation.
All high frequency bands shifted to higher wavenumbers in agreement with the shift of the envelope of the high frequency Raman spectra. Interestingly, the phosphate band J shifted much less than the aluminosilicate band H (band positions are indicated in Figure 4.18). This observation will be subject of discussion in Section 4.8.
Among the two phosphate-related bands J and L, band J corresponds to the

more symmetric vibration because its intensity relative to band L strongly decreased upon cross-polarisation.

Raman bands of glasses with constant 0 mol% P_2O_5 The Raman spectra of the glasses with 0 mol% P_2O_5 (Figure 4.13) were all similar to the spectrum of glass Si60P0 described above. Variation of the silica content resulted in band shifts and relative intensity changes. The relative degrees of symmetry of the vibrations, found by comparing VV and VH spectra, did not change.
In the low frequency region, upon increasing SiO_2 content, the VV band D shifted from 498 to 490 cm^{-1} and the shoulder C at 460 cm^{-1} slightly increased in intensity compared to D. At the same time, band E shifted from 562 to 575 cm^{-1} and its intensity relative to band D decreased. The intensity decrease of band E could also be observed in the VH spectra. The VH counterpart of band B showed a slight intensity increase with respect to the VH band D, while the VV band B did not markedly change in intensity.
In the middle frequency region, the intensity of band F relative to band G decreased with increasing mol% SiO_2. This was visible more clearly in the VH spectra. In the VV spectra, band F seemed to shift to lower wavenumbers because it partially overlapped with the much stronger band E. In the VH spectra, no shift of the 700 cm^{-1} band F to lower wavenumbers could be confirmed. The intensity of band G relative to band D increased with increasing mol% SiO_2.
In the high frequency region, all VV and VH bands shifted towards higher wavenumbers with increasing SiO_2 content and - except for the VH band K - lost intensity compared to the low frequency bands. The VV band I shifted from 1005 to 1088 cm^{-1}. The VH band H shifted from 970 to 1000 cm^{-1} and the corresponding VV shoulder H became more visible with increasing SiO_2 content. The VH shoulder K shifted from 1040 to 1090 cm^{-1} and its VH intensity increased relative to the VH band H.

Raman bands of glasses with constant 7.5 mol% P_2O_5 The Raman spectra of all glasses with 7.5 mol% P_2O_5 were similar, differing only in band shifts and relative intensity changes (Figure 4.14). The bands were the same as identified above for the glasses with 60 mol% SiO_2 and higher phosphate contents. The relative degree of symmetry of the vibrations, found by comparing VV and VH spectra, did not change. The changes with increasing SiO_2 content were the same as described for the glasses with 0 mol% P_2O_5.
In the low frequency VV region (below 650 cm^{-1}), the band maximum D

shifted from 496 to 486 cm^{-1} and the shoulder C gained intensity relative to band D.[19] Band E lost intensity compared to band D and shifted from 575 to 593 cm^{-1}. Band B slightly increased in intensity with respect to band D. The VH spectra followed similar relative intensity changes as the VV spectra upon increasing SiO_2 content.
In the middle frequency region (650 - 850 cm^{-1}), band F lost intensity relative to band G with increasing SiO_2 content. This became more clear in the VH spectra, because in the VV spectra band F partially overlapped with band E. The intensity of band G relative to band D increased with increasing mol% SiO_2.
In the high frequency region (above 850 cm^{-1}), all VV and VH bands shifted towards higher wavenumbers with increasing SiO_2 content and all distinguishable bands except for band L lost intensity compared to the low frequency bands. For glass Si70P7.5 the VH intensity difference between bands J and L became so small that band L appeared as an individual VH band maximum instead of a shoulder. The VV band J shifted from 1050 to 1076 cm^{-1}. The VV shoulder L shifted from 1195 to 1210 cm^{-1}. The VH bands J and L shifted in a way similar to their VV counterparts.

4.6.3 Band assignments

As seen above, most of the identified infrared and Raman bands (Figures 4.12 to 4.14 and Table 4.3) were common to all studied glasses. For many bands, more than one possible assignment was found, making extensive discussion necessary.

Infrared band assignments Bands in the FIR region correspond to local motion of alkali cations situated in their oxide sites, or *oxygen cages* [82, 84, 139, 140, 234]. They may contain information about whether the alkali ions are acting as network modifiers or as charge balancing ions [140]. The FIR band a (158 - 205 cm^{-1}) is thus assigned to vibrations of Na^+ ions. This matches the decrease of the FIR band intensity that occurred whenever the Na_2O content of the glasses decreased, owing to substitution by either

[19] The intensity gain of band C relative to band D was so strong that in case of the glass Si70P7.5, if no data reduction by the Long equation was applied, band C replaced D as maximum of the low frequency region.

phosphate or silica. The FIR band position also matched well with the position found by Kamitsos et al. in an earlier infrared spectroscopic study on sodium aluminosilicate glasses [83].
Band b (460 cm^{-1}, Figures 4.12 to 4.14) has been related either to the bending mode of $[AlO_4]^-$ tetrahedra [83] or to Al-O stretching [234]. However, this cannot be the only contribution because band intensity increased with decreasing Al_2O_3 content in the glass series with increasing silica content. This suggests a strong contribution from silicon-containing units. Bands in this region have also been assigned to Si-O rocking [30, 56, 79, 86, 95, 168] or to Si-O bending [30], based on multiple approaches such as neutron scattering [168], infrared spectroscopy [86] and molecular dynamics simulations [30]. Here, Si-O rocking will be considered the most important contribution as suggested by Galeener [56], but without entirely excluding the other assignments.
The weak shoulder c (535 - 545 cm^{-1}) only appeared for phosphate-containing glasses. This suggests a link to P-O bending vibrations that have been found in this region for metaphosphate glasses [234]. Additionally, this band has been assigned to Si-O-Al bonds involving six-coordinated aluminium by comparison with a layered aluminosilicate mineral [32, 214]. However, as solid-state NMR results confirmed aluminium to be present in fourfold coordination exclusively (Section 4.5), band c is probably related to P-O bonds. The shifts of band c with respect to its weak intensity were too small to allow for meaningful interpretation.
Band d (700 cm^{-1}) has been assigned to the antisymmetric stretching of $[AlO_4]^-$ tetrahedra [83]. This is in agreement with its decrease in intensity relative to the 780 cm^{-1} band e with decreasing Al_2O_3 content. Band e (780 - 800 cm^{-1}) can be assigned to Si-O-Si bending in agreement with a similar band in the infrared spectrum of vitreous silica [79, 83, 86, 247]. Its shift towards higher wavenumbers for the glasses with 7.5 mol% P_2O_5 may be associated with a decreasing Al/Si ratio affecting the associated force constants. Similar shifts were not observed for the other two glass series, but only because the band was too weak there. Shifts of the corresponding Raman band G suggest that band e also shifted in all three glass series.
Band f (860 cm^{-1}) was only found for glass Si50P0. Of all studied glasses, this is the composition with the largest amount of Al_2O_3. Therefore, band f may be related to aluminium. An exact assignment is difficult because aluminate bands are typically weak compared to silicate and phosphate bands. Band f is tentatively assigned to stretching of $[AlO_4]^-$ tetrahedra in agreement with calculations and measurements on mullite [124] as well as similar findings for aluminium in mixed network former oxide glasses [212].
In the high frequency IR region, any aluminosilicate-related bands found

in phosphate-free glasses will be assumed to still be present in phosphate-containing glasses, coexisting with phosphate-related bands. Furthermore, the new IR phosphate bands are not assumed to be much stronger in intensity than the IR aluminosilicate bands. A dominating intensity of phosphate bands is only to be expected for VV Raman bands, owing to the polarisability selection rule.

Band g (982 - 1079 cm^{-1}) in phosphate-free glasses is assigned to antisymmetric Si-O stretching in Q^4_{Si} units [75, 79, 86, 209]. The mode has to be antisymmetric in order to yield such a strong infrared signal. The cited references assumed Q^4_{Si} vibrations to be found at higher wavenumbers, but their glasses did not contain aluminium. The presence of Al will reduce the average force constant of the glass network and thus shift the Q^4_{Si} vibrations to lower wavenumbers because Al-O bonds are weaker than Si-O bonds, see refs. [32, 83, 140, 157, 163, 194] and p. 367 of ref. [54]. In this thesis, the presence of depolymerised silicate units such as Q^3_{Si}, which alternatively may be present at $\sim 1000\,cm^{-1}$, is considered unlikely because of the metaluminous glass compositions.

The shoulder h (1100 - 1150 cm^{-1}) in phosphate-free glasses is also assigned to a vibration of Q^4 units [75, 209]. Having two different bands both assigned to Q^4 units agrees with many Raman spectroscopic studies on aluminosilicate glasses and can be interpreted as the presence of two different sets of preferred intertetrahedral bond angles within the Q^4 network [109, 157, 163, 194].

The shoulder i (1130 - 1170 cm^{-1}) in phosphate-containing glasses is assigned to antisymmetric P-O stretching in Q^2_P units [67, 100, 234]. The cited references found this mode present at higher wavenumbers of 1250 - 1270 cm^{-1} for metaphosphate glasses. The shift to lower wavenumbers in the aluminosilicate glass system can be justified by the same argument described above to explain the shift of the SiO_4 stretch band g to lower wavenumbers.[20] The presence of silicon and aluminium lowers the overall force constant of the glass compared to a pure metaphosphate glass. Therefore, the phosphate-related band is also shifted to lower wavenumbers. Mysen and Cody [146] have argued that phosphate-related bands will shift if their corresponding phosphate groups are linked to the aluminosilicate network. Furthermore, the assignment of band i to metaphosphate units is supported by the NMR results which indicate a high proportion of phosphorus to be present as Q^2_P units (Section 4.5).

[20] In contrast to the metaphosphate glasses from abovementioned refs. [67, 100, 234], a Q^2_P group in this study is not necessarily linked to two other phosphate tetrahedra, but may also be linked to silica or aluminate tetrahedra [27, 146, 161].

Raman band assignments Band A (Figures 4.12 to 4.14) represents the reduced Boson peak; this feature is common to Raman spectra of all amorphous materials [4, 14, 129, 258]. Although there have been recent attempts to link the Boson peak to medium range order [4], its nature is still not satisfactorily clarified. Here, the Boson peak will not be further taken into account because a full investigation would be beyond the scope of this thesis. The broad band envelope of the low frequency region is associated with ring statistics in silicate glasses [57, 58, 159, 201], showing vibrations related to rings of several connected tetrahedral units. The larger the rings, the more open the glass network structure will be. Therefore, changes in the low frequency region may be correlated with densification of glasses, as discussed in detail in Section 4.10.2.
The bands D (486 - 498 cm^{-1}) and E (562 - 593 cm^{-1}) are assigned to the ring breathing modes of four-membered [110, 163, 200] and three-membered rings [110, 132, 163], respectively. Ring breathing vibrations are very symmetric as they imply simultaneous movement of the bridging oxygens of the rings [58, 70]. This is in agreement with the high intensity loss of bands D and E upon cross-polarisation. Band D has also been assigned to T-O-T bending in general [155] (T = Si, Al) or alternatively to the presence of Si-O-Al bridges [83, 135]. However, these assignments do not exclude the ring breathing assignment. The shifts of band D upon compositional change were too small to allow for meaningful interpretation and may also be caused by overlap with band C. The shifts of band E for all three glass series, on the other hand, may be associated with a decreasing Al/Si ratio if three-membered rings of mixed tetrahedral species are present.
The shoulder B (310 cm^{-1}) may be assigned to the breathing of six membered rings as in the mineral beryl [94]. However, such a symmetric mode is unlikely considering the low VV intensity of band B. Other assignments for this shoulder are Al-O stretching and P-O bending [234]. Unfortunately, the compositional variation of band B is too weak to identify a trend linked to either Al_2O_3 or P_2O_5 content. Hehlen and Neuville [71] have recently proposed that a VH band of silicate and aluminosilicate glasses in the wavenumber range of band B (300 - 350 cm^{-1} [71]) can be assigned to alkaline ions fulfilling the role of network modifier. For the glasses studied in this thesis, the question whether sodium plays the role of modifier or charge-balance is of importance for the understanding of glass structure. However, the increase of VH band B with increasing silica content and thus decreasing sodium content is not in favour of an assignment to sodium. Furthermore, the studied glasses are assumed to contain mostly charge-balancing sodium, owing to their amounts of Na being equal or lower than the combined amounts of Al and P.
Band C (460 cm^{-1}) is assigned to six-membered rings of mixed SiO_4 and

$[AlO_4]^-$ tetrahedra [49], but not necessarily their breathing mode, which is assigned to band B [94]. This is in agreement with the earlier finding that albite glass contains mainly six-membered rings [201]. The composition of albite glass (in mol% 75 SiO_2 - 12.5 Al_2O_3 - 12.5 Na_2O) is close to the studied glasses with 70 mol% SiO_2, in which band C reached its highest intensity.
The assignment of bands F (700 cm^{-1}) and G (760 - 790 cm^{-1}) in the middle frequency region is simplified significantly if VH spectra are taken into account. For decreasing Al_2O_3 content (increase in either SiO_2 or P_2O_5 content), the 700 cm^{-1} VH band decreased in intensity with respect to band G. Band F is therefore assigned to stretching of $[AlO_4]^-$ tetrahedra [83, 134]. This is a symmetric vibration, which agrees with the intensity difference between VV and VH spectra. For phosphate glasses, a band at this position has also been assigned to symmetric P-O-P stretching [19, 20, 167]. However, this assignment does not fit the observed decrease of VH band intensity with increasing P_2O_5 content. Band G is assigned to Si-O-Si bending. This fits well with its increasing intensity with increasing SiO_2 content and is supported by a similar assignment by Kamitsos et al. for sodium aluminosilicate glasses [83]. The shifts of band G may be associated with decreasing Al/Si ratio. The similarities between Raman bands F and G and IR bands d and e, as well as their similar band assignments, indicate that those vibrations are partially IR and Raman active, i.e. being only partially symmetric.
Regarding the high frequency Raman region, five different bands need to be discussed. Two of them, J and L, are clearly related to phosphate as they only appeared upon P_2O_5-incorporation. The other three bands, H, I and K, made up the high frequency envelope in the phosphate-free glasses and therefore correspond to vibrations of the aluminosilicate network. They are also present in the phosphate-containing glasses, but here the phosphate bands J and L dominate the VV spectra.
In studies of aluminosilicate glasses, the high frequency bands are often ascribed to stretching modes of Q^2, Q^3 and Q^4 groups of either Si or Al [144, 147, 204, 209]. However, that assignment assumes depolymerisation of the aluminosilicate network. In this thesis, all glasses were designed to have fully polymerised aluminosilicate networks. Gan and Hess also have argued in favour of fully polymerised aluminosilicate networks in their study of phosphate-containing potassium aluminosilicate glasses [62]. Earlier studies on phosphate-free metaluminous glasses [109, 135, 157, 160, 163, 168, 194] derived a plausible assignment of all high frequency bands to Q^4 units of either Si or Al. The idea can be traced back to the theoretical work by Sen and Thorpe [196]. They proposed a central force model to analytically predict the band structure of vitreous silica depending on the intertetrahedral bond angles and force constants. According to this model and to further

development by Galeener [56], the spectrum of vitreous SiO_2 contains bands corresponding to two different sets of intertetrahedral bond angles. Seifert et al. [194] have identified this bond angle difference to be 5 to 10° and have introduced the idea that these two structural sets differing only by bond angle will also be maintained in metaluminous aluminosilicate glasses. Since then, this idea has been nurtured by several authors [109, 135, 157, 160, 163] and supported by neutron scattering [168]. The distinction of structural units only by intertetrahedral angle implies a uniform distribution of Al and Si atoms [160, 194] which has been supported by X-ray scattering [222]. Following the assignments in the abovementioned literature and the notation of ref. [163], the bands I (1005 - 1088 cm^{-1}) and K (1040 - 1090 cm^{-1}) are assigned to the stretching of Q^4 units of either Si or Al. Band K will be called $Q^{4,high}_{Si/Al}$ and corresponds to stretching of units with larger intertetrahedral angles. Band I will be called $Q^{4,low}_{Si/Al}$ and corresponds to stretching of units with smaller intertetrahedral angles. As band I lost more intensity upon cross-polarisation, the smaller intertetrahedral angles seem to result in higher local symmetry. Band H (970 - 1027 cm^{-1}) is assigned to the T_{2s} mode of Q^4 units, regardless of their intertetrahedral angle. In this vibrational mode, two oxygen atoms move towards the central Si or Al atom of a tetrahedron while the other two oxygen atoms move away from the tetrahedral centre. This vibration is less symmetric than the $Q^{4,high}_{Si/Al}$ and $Q^{4,low}_{Si/Al}$ modes, which fits with the observation that band H was the strongest high frequency band in the VH spectra.

The phosphate-related bands J and L could not be assigned unambiguously. According to many studies focussing on phosphate glasses [20, 67, 100, 167, 234, 251] both bands J (1050 - 1076 cm^{-1}) and L (1195 - 1215 cm^{-1}) can be assigned to metaphosphate units (Q^2_P). In these references, the metaphosphate bands were found at higher wavenumbers of about 1180 and 1280 cm^{-1}, respectively. The shift towards lower wavenumbers can be justified with the high (Si+Al)/P ratio of the studied glasses, assuming that the metaphosphate units are well distributed and connected to the aluminosilicate network. Alternatively, band J could also be assigned to the antisymmetric stretching of Q^1_P units [67, 234]. However, this assignment can be dismissed based on the solid-state NMR results indicating little to no Q^1_P (Section 4.5) and on the observation that the vibration of band J is symmetric.

A second potential assignment links bands J and L to Al-O-P bonds. Many studies on phospho-aluminosilicate glasses agreed that there should be preferred formation of Al-O-P bonds compared to Si-O-Al bonds because of a strong tendency for charge-balancing between aluminate and phosphate tetrahedra [62, 102, 144, 150, 184]. Kosinski et al. [102] have linked the

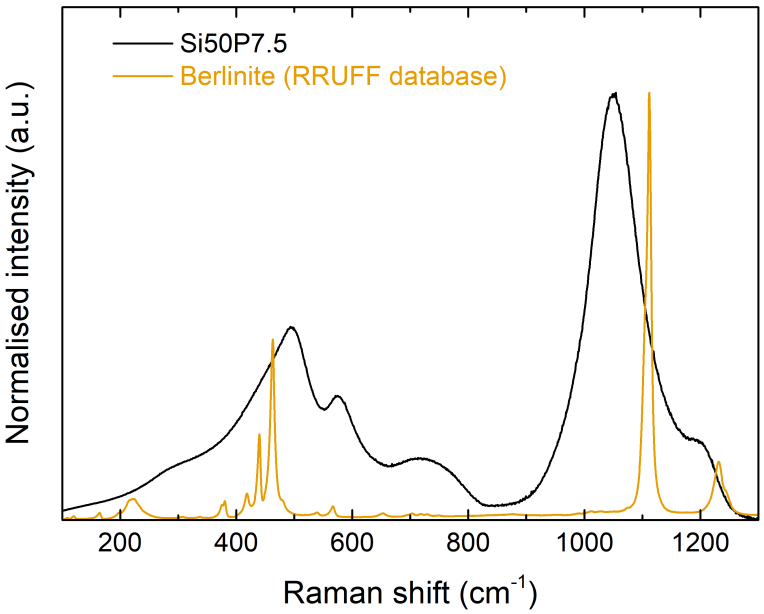

Figure 4.19: Comparison of the Raman spectra of glass Si50P7.5 and the mineral berlinite ($AlPO_4$, mineral Raman data from the RRUFF database, entry R130243 [106]). Both spectra were reduced by the Long equation and normalised to the maximum intensity.

high intensity of these bands to the high polarisability of Al-O-P bonds and have compared them with the high frequency bands of the mineral berlinite ($AlPO_4$), which consists only of Al-O-P bonds in a quartz-like structure. Interestingly, the berlinite Raman spectrum has a pair of high frequency Raman bands at 1112 and 1232 cm^{-1} which match very well with the phosphate-related bands J and L as regards relative band intensity. This is illustrated in Figure 4.19, which compares the Raman spectra of glass Si50P7.5 and berlinite, the berlinite spectrum being extracted from the RRUFF mineral database (entry R130243) [106]. Both spectra were reduced by the Long equation and normalised to the maximum intensity. The shift between the bands of berlinite and Si50P7.5 may be explained by the presence of Si in Si50P7.5 and its reduced P_2O_5 content compared to berlinite.
The difficulty in assigning the phosphate-related bands to either Al-O-P bonds (Q^4_P) or metaphosphate groups (Q^2_P) has been pointed out in earlier Raman studies [62, 144, 146]. They have suggested a coexistence of Q^4_P and Q^2_P, reasoning that Al-O-P bond formation will liberate sodium that formerly was required for charge-balancing $[AlO_4]^-$ tetrahedra and which may alternatively charge-balance Q^2_P groups. Such a coexistence of Q^2_P and Q^4_P

has also been supported by NMR spectroscopy in the literature [96, 189] as well as NMR measurements on the glasses studied here (Section 4.5).
The only phosphate species that can be excluded by Raman spectroscopy with some certainty is Q^3_P because it carries a P=O double bond. In phosphate glasses, this bond gives rise to a distinct band at $1380\,cm^{-1}$ [19] separated from the high frequency envelope, but such a separate band was not found for the glasses of this study. The band could be shifted to lower wavenumbers owing to the aluminosilicate environment, thus vanishing underneath band L. However, as will be discussed in Section 4.6.4, the far-infrared band shifts suggest a much more likely association of phosphate with sodium, creating $Q^{i<3}_P$.
Besides association of phosphate with Na or Al, an association with Si is also possible. Si-O-P bonds have been considered as assignment in studies on phospho-silicate glasses [24, 203] as well as on phospho-aluminosilicate glasses [102, 144, 150]. However, while the Si-O-P bond assignment mostly remained a tentative one in the cited references, some of them have delivered strong arguments for Al-O-P bonds [102, 144]. Thermodynamic studies have found the Si-O-P bond formation unlikely compared to Al-O-P bonds [119, 184]. A multi-dimensional solid-state NMR analysis performed on the glasses studied here also found Si-O-P bonds to be unlikely [161].
Taking all of the above discussion into account, the bands J and L will be assigned equally to metaphosphate (Q^2_P) units and Al-O-P bonds (Q^4_P). Band J is therefore assigned to the symmetric stretching and band L to the antisymmetric stretching of Q^2_P units.
Concluding from this, the network structure of the studied glasses most likely consists of uniformly distributed silica and aluminate Q^4 groups, with small amounts of phosphate groups of either Q^4_P or Q^2_P state linked either to other phosphate groups or to aluminate groups. Silica groups will be linked to aluminate or other silica groups. Aluminate groups will be linked to silica or phosphate groups. The possibility of neighbouring aluminate groups, opposing the Löwenstein rule [118], is discussed in Section 4.6.4.
The high frequency Raman bands shifted to higher wavenumbers with increasing silica and phosphate contents. For phosphate-free aluminosilicate glasses, this shift was explained by a good mixing of aluminate and silicate tetrahedra and by the stronger Si-O bonds compared to Al-O bonds [150, 157, 163, 194]. For this thesis, the same argument should be considered valid when replacing either Al-O or Si-O bonds with P-O bonds because the bond strength increases in the order Al-O < Si-O < P-O, see refs. [167, 184] and p. 33 of ref. [230]. These shifts appear to be an indicatior of strength of chemical bonds within the glasses, and they will be analysed in greater detail in Section 4.8.

4.6.4 The IR sodium band

The shift of the FIR band a (Figures 4.15 to 4.17, summarised in Figure 4.20) bears information about the role of sodium in the studied glasses. A shift of the FIR band to higher wavenumbers corresponds to a higher vibrational frequency of the sodium ions within their oxygen cages, meaning they are exposed to stronger chemical bonds. As the bonds involving sodium are mostly ionic, the shift to higher wavenumbers indicates a higher net negative charge of the environment surrounding sodium [78, 80, 84, 85].
Within the studied glasses, sodium is assumed to take a charge-balancing role, either for aluminate ($[AlO_4]^-$) or for metaphosphate (Q^2_P) groups. The role of network modifier, forming NBO with silicate groups, is considered unlikely because of the excess of groups requiring charge-balancing, i.e. (Al+P)/Na ≥ 1. The different potential chemical environments of Na^+ correspond to different FIR frequencies that overlap to form the FIR band [80–84, 253].
The shifts of the FIR band may thus be interpreted as a competition between aluminate and metaphosphate groups for charge-balancing sodium. Both groups bear the same formal charge of -1, but Na^+ is assumed to associate with the region of highest electron density for each group. For the metaphosphate group, Na^+ will associate with NBO, for the aluminate group with BO. As NBO carry a higher negative charge density than BO, the phosphate group will provide a more negative environment for Na^+. This corresponds to a higher frequency of the FIR band.[21]
The FIR band a shifted towards higher wavenumbers both with increasing phosphate content (Figure 4.20a) and with increasing silica content for glasses with 7.5 mol% P_2O_5 (Figure 4.20b, orange circles). Interestingly, the band shift observed with increasing SiO_2 content for phosphate-free glasses (Figure 4.20b, black squares) was opposite to that for phosphate-containing glasses, i.e. directed towards lower wavenumbers. Such opposing trends for phosphate-free and phosphate-containing glasses were also found for T_g (Figure 4.2, p. 55). Knowledge of the structural role of sodium may thus be helpful in understanding the T_g trends.
The shift of the FIR band to higher wavenumbers with increasing phosphate content (Figure 4.20a) is a result of an increasing ratio of P/Al when P_2O_5

[21] In reality, sodium ions will be coordinated by several structural groups providing a combined negative environment. Nevertheless, the hypothetical discussion of sodium associated with just one structural group at a time helps to provide a qualitative understanding of the groups' relative contributions to the bonding of sodium.

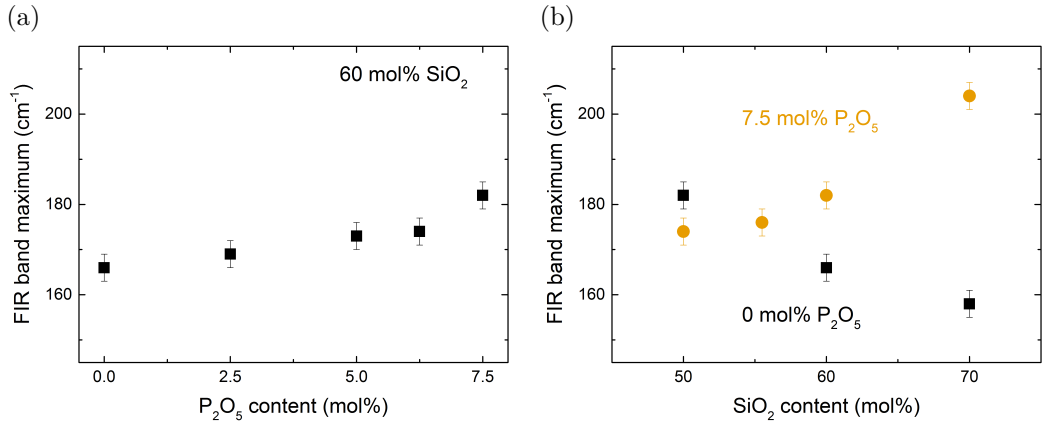

Figure 4.20: Dependence of the FIR band position on glass composition. (a) Increasing P_2O_5 content and constant 60 mol% SiO_2. (b) Increasing SiO_2 content and constant P_2O_5 contents of 0 mol% (black squares) and 7.5 mol% (orange circles).

is substituted for $NaAlO_2$. From the remaining sodium ions, a higher percentage will associate with phosphate groups instead of aluminate groups. The FIR band shift of phosphate-free glasses to lower frequencies with increasing SiO_2 content (Figure 4.20b, black squares) indicates that for substitution of SiO_4 for $Na^+[AlO_4]^-$ tetrahedra, the remaining sodium is bound more weakly, even though each sodium ion should still be associated with one aluminate tetrahedron. This may be explained by the fact that the FIR band frequency does not correspond to the strength of a single type of sodium-oxygen bond but to an averaged negative charge of all Na^+ sites in a glass. Sodium-oxygen bonds are largely ionic and therefore non-directional. Even if each sodium ion is associated with its nearest aluminate tetrahedron, it may still be influenced by the negative charge of other aluminate tetrahedra in the vicinity. This is very likely for glass Si50P0, because for this composition the amount of $Na^+[AlO_4]^-$ tetrahedra equals the amount of SiO_4 tetrahedra. Each sodium ion will have more than one aluminate tetrahedron in its vicinity. For glass Si70P0, the ratio of Al/Si has decreased from unity to less than 0.5. The average distance between aluminate tetrahedra will thus be higher. Sodium ions will be less influenced by the more distant aluminate groups because ionic interaction is governed by Coulomb's law, which scales by distance^{-2}. Therefore, the net charge of sodium sites will be less negative. This hypothesis may explain the observed FIR band shift to lower wavenumbers. To further verify this hypothesis, one may measure the FIR spectra of metaluminous glasses with less than 50 mol% SiO_2, i.e.

with a ratio of Al/Si > 1. If such glasses can still be produced with all Al in fourfold coordination, then the shift of the FIR band should be saturated as soon as an Al/Si ratio is reached for which sodium ions are only surrounded by aluminate tetrahedra.
In contrast to the phosphate-free glasses, the FIR band of the phosphate-containing glasses (Figure 4.20b, orange circles) shifted to higher frequencies with increasing silica content. This may be explained by a changing Al/P ratio. Upon substitution of SiO_4 for $Na^+[AlO_4]^-$ tetrahedra, the amount of sodium and aluminium ions in the glasses is reduced while the amount of phosphate remains constant. Therefore, the relative contribution of aluminate environments to the FIR band compared to the contribution of the metaphosphate environment will decrease. This will effectively shift the FIR band towards the higher frequencies associated with the strong interaction between sodium and phosphate.
This leaves the question why T_g decreased for those glasses upon increasing SiO_2 content, even if a higher fraction of Na^+ was bound more strongly. The interaction between sodium ions and their oxygen cage is not long-ranged. Although the Na-O bond strength will have some contribution to T_g, the creation of NBO by depolymerisation will have a larger impact on T_g [81, 143, 253].
However, if the phosphate content is kept constant and SiO_4 tetrahedra are substituted for $Na^+[AlO_4]^-$ tetrahedra, both polymerisation and T_g should remain constant. The observed decrease in T_g spanned only about 30 K and thus was small when compared to the 80 - 120 K drop occurring upon increasing P_2O_5 content from 0 to 7.5 mol% (Figure 4.2). A potential change in polymerisation associated with this small T_g decrease will also be small. One possible scenario involves the formation of oxygen triclusters. Such oxygen triclusters have been suggested to exist in aluminosilicate glasses [21, 104, 105, 172, 210, 211, 229] and the multi-dimensional solid-state NMR experiments on the present glasses, performed by Alina Nizamutdinova as part of a collaboration, also suggest the possible presence of oxygen triclusters here [161].
Upon increasing SiO_2 content and decreasing Al/P ratio in glasses with constant 7.5 mol% P_2O_5, Na^+ likely associates with phosphate rather than aluminate. Given that multi-dimensional solid-state NMR and vibrational spectroscopy found phosphate both as Q^2_P and Q^4_P groups, the latter with Al-O-P bonds, the association with Na^+ should increase the amount of Q^2_P at the expense of Al-O-P bonds. The remaining aluminate groups will require another charge-balance or have to assume a higher coordination state. NMR spectroscopy indicated all Al to remain in fourfold coordination (Section 4.5). To still achieve charge-balance, an aluminate tetrahedron may form an oxygen

tricluster by sharing a common BO with two other tetrahedra. The resulting positive partial charge on the oxygen tricluster could at least partially compensate the negative charge of the aluminate tetrahedron, see e.g. p. 113 of ref. [230]. Such a tricluster formation would conserve all bonds of the affected aluminate tetrahedron while creating one additional bond on the tricluster oxygen. The simultaneous creation of Q^2_P from Q^4_P would create two NBO. In total, the glass structure would lose one bond in this scenario and thus depolymerise, which could explain the observed slight decrease in T_g.

4.6.5 Deconvolution of Raman spectra

For phosphate-free metaluminous glasses, well-discussed deconvolutions may be found in refs. [109, 160, 163]. First deconvolution attempts on phosphoaluminosilicate glasses have been published [144, 148, 150], but they all originate from the same author. Out of these references, only one shows deconvoluted spectra that address phosphate addition to metaluminous glasses [150]. However, this reference disagrees with more recent publications on phosphate-free glasses [109, 163] regarding the number of bands fitted to the phosphate-free reference glass.

In the deconvolution attempt presented here, the number of fitted bands was chosen to match the number of bands identified in the VV/VH Raman spectra. The phosphate-free glasses were thus deconvoluted with three bands assigned to the vibrations T_{2s} (970 - 1027 cm^{-1}), $Q^{4,low}_{Si/Al}$ (1005 - 1088 cm^{-1}) and $Q^{4,high}_{Si/Al}$ (1040 - 1090 cm^{-1}, details in Table 4.3, p. 70). They will be referred to as aluminosilicate bands and were also used for the deconvolution of the phosphate-containing glasses, along with two additional bands assigned to symmetric (ν_s, 1050 - 1076 cm^{-1}) and antisymmetric stretching (ν_{as}, 1195 - 1215 cm^{-1}) of Q^2_P units.[22]

The phosphate-free glass series was deconvoluted first (Figure 4.21). A comparison with previous studies on metaluminous aluminosilicate glasses [26, 109, 160, 163] allowed to assess the quality of the obtained fits. Afterwards, the more challenging deconvolution of phosphate-containing glasses was studied for the glass series with constant 60 mol% SiO_2 (Figure 4.22).

While each spectrum of the phosphate-free glasses was deconvoluted individually, the evaluation of the entire glass series provided a means to judge the

[22] For the sake of simplicity, the other potential assignments of the phosphate bands (Table 4.3) were omitted here.

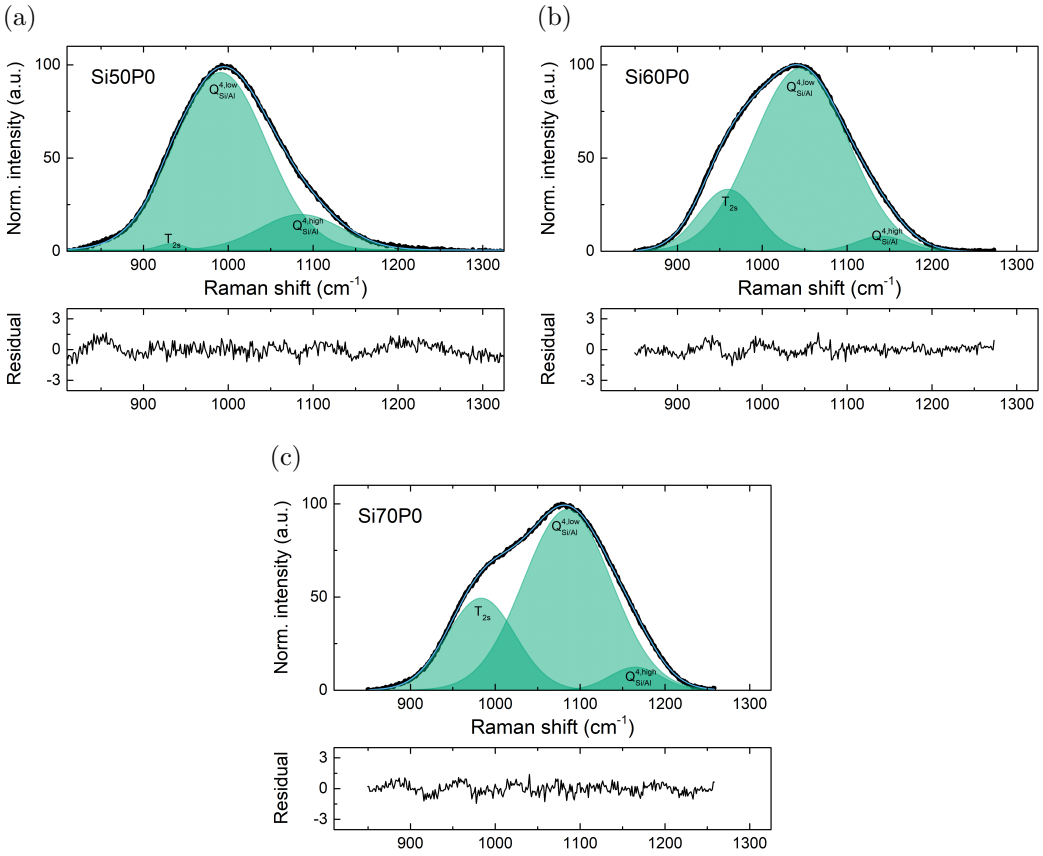

Figure 4.21: Deconvoluted high frequency Raman spectra and residuals for the glasses with 0 mol% P_2O_5. (a) Si50P0. (b) Si60P0. (c) Si70P0. Experimental data is presented in black, bands contributing to the deconvolution in green and the sum curve of the fitted model in blue. Band assignments are indicated.

physical consistency of the results. Depending on the variation of the starting parameters, more than one mathematical solution was possible for each of the glasses. The presented solutions (Figure 4.21) were chosen for yielding consistency between the three glasses, as this implies that the three glasses have very similar network structure, which is reasonable for metaluminous glasses of constant ratio Al:Na = 1. Also, the chosen fits matched with those reported in the literature [26, 109, 160, 163], including similarly low residuals and a similar remaining non-randomness of the residuals.

For the phosphate-containing glasses (Figure 4.22), the deconvolution with five bands was less straightforward. Their spectra only showed two to three visible bands, and the remaining hidden bands would therefore need to be

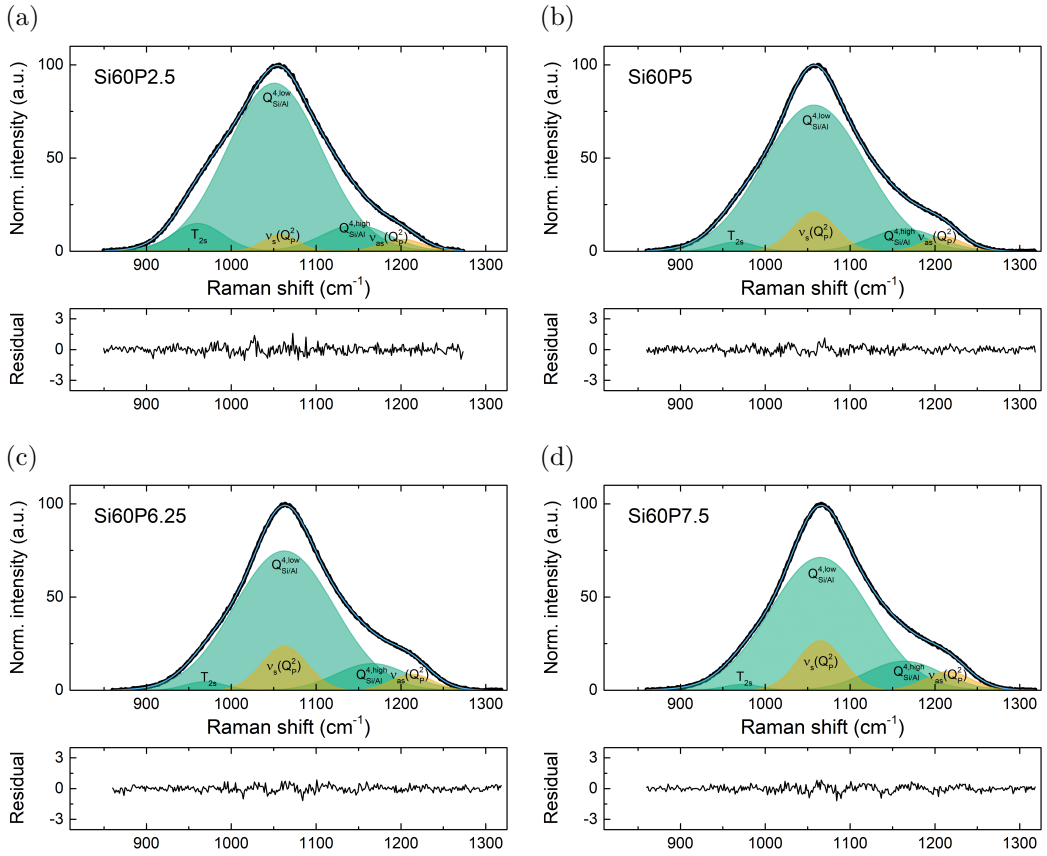

Figure 4.22: Deconvoluted high frequency Raman spectra and residuals for the phosphate-containing glasses with 60 mol% SiO_2. (a) Si60P2.5. (b) Si60P5. (c) Si60P6.25. (d) Si60P7.5. For Si60P0 see Figure 4.21b. Experimental data is presented in black, bands contributing to the deconvolution in green (aluminosilicate bands) and orange (phosphate bands) and the sum curve of the fitted model in blue. Band assignments are indicated.

rather weak, thus giving a large number of possible mathematical fits. A fit that was consistent within the glass series and with the VV/VH data could only be achieved when selecting the starting parameters within a narrow window. This is undesirable, but within the given limit of selecting parameters manually no better result could be obtained during the time frame of this thesis. For future deconvolution attempts, it might be beneficial to implement an automated exploration of the starting parameter space; however this may significantly increase the required computational time. Alternatively, a more efficient model will have to be found, possibly by changing

the peak shape. For example, the use of peak shapes with partial Lorentzian and Gaussian character appears to be beneficial [9], whereas pure Lorentzian peaks seem to yield less accurate fits [87, 194]. Further development of the model is, however, beyond the scope of this thesis.
In spite of these limitations, a set of fits could be found (Figure 4.22) which was consistent with the increasing phosphate content and with the reference fit of glass Si60P0. For increasing P_2O_5 content, the three aluminosilicate bands gradually decreased in intensity while the phosphate bands, especially $\nu_s(Q_P^2)$, increased in intensity. These results were considered to carry enough physical validity to justify their further analysis.
All presented deconvolutions showed a good agreement between experimental data and fitted models (black and blue lines in Figures 4.21 and 4.22). The residuals remained low, below 3 % of the maximum spectral intensity. They were more random for the phosphate-containing glasses than for the phosphate-free ones. However, this is probably caused by their larger number of fitted bands. The highest non-randomness of the residual was found for glass Si50P0 and may be caused by the luminescence that was typically observed for this glass.
All deconvoluted bands of the phosphate-free glasses (Figure 4.23a) shifted to higher wavenumbers with increasing silica content, matching similar observations for the measured IR and Raman spectra. For the glass series with increasing phosphate content (Figure 4.23b), similar band shifts were found. Here, the shifts were less pronounced, possibly owing to the different compositional changes. A discussion of the shifts with respect to glass composition will follow in Section 4.8.
A direct comparison of the deconvoluted band positions with experimental data was possible for the three bands which showed a clear maximum in the experimental VV or VH spectra. These were $Q_{Si/Al}^{4,low}$ in the phosphate-free glasses, $\nu_s(Q_P^2)$ and T_{2s}. A good agreement only occurred for the first two bands, which were at VV maximum positions. In case of the VH maximum, T_{2s}, the deconvoluted band positions were significantly lower than the experimental positions and also their total shifts for changing composition differed. Apparently the mathematical fitting of band T_{2s} was imprecise, because the band was hidden in the spectra used for deconvolution. Based on this, it is concluded that deconvoluted band positions should be treated with caution whenever shoulders or hidden bands are concerned. The deconvoluted band position observed for $Q_{Si/Al}^{4,high}$ in phosphate-containing glasses with ≥ 5 mol% P_2O_5 remained roughly constant, with increasing error of the deconvolution. This may originate from the same limitations of fitting hidden bands.
Also, the band positions of $\nu_s(Q_P^2)$ and $Q_{Si/Al}^{4,low}$ appeared to be equal for all

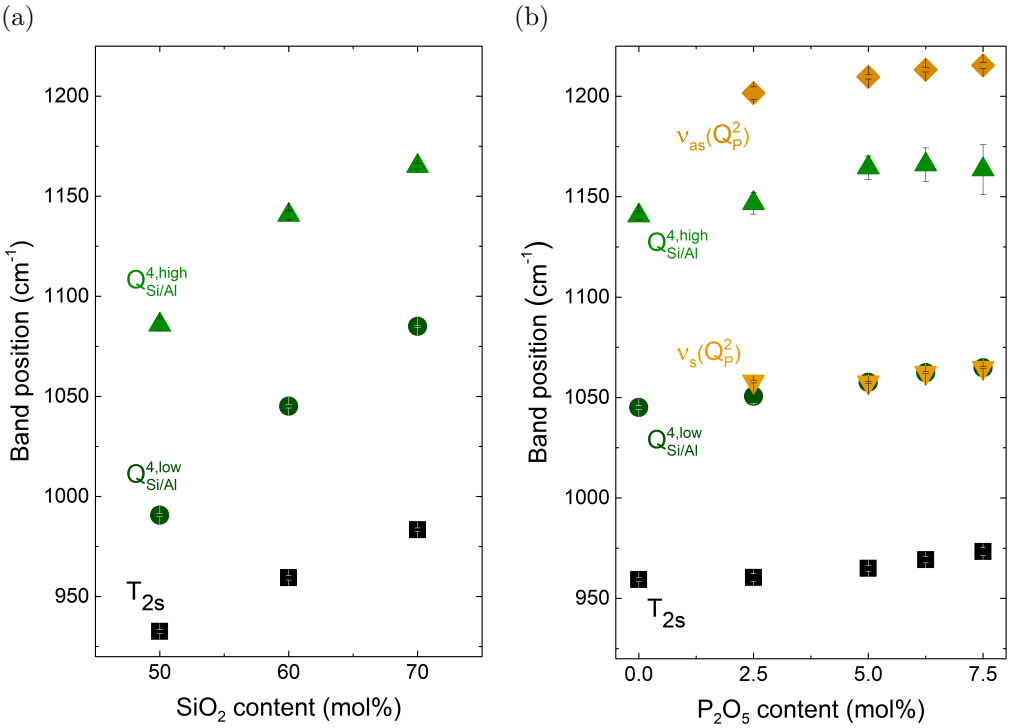

Figure 4.23: Positions (in cm^{-1}) of the deconvoluted Raman bands (assignments indicated) depending on glass composition. (a) Phosphate-free glasses and increasing SiO_2 content. (b) Constant 60 mol% SiO_2 and phosphate content increasing from 0 to 7.5 mol%.

glasses with ≥ 5 mol% P_2O_5. This is probably an artifact of the fitting process and may indicate that the fitting parameters were not independent of each other, even though no parameter constraints were exerted on individual Gaussians. This could mean that five bands are too many for a fit of these spectra, because only two to three of the five experimentally observed bands are discernible from the envelope. Alternatively, the equal band positions could indicate that Gaussian peaks are too simple for this fitting problem. A test with peaks of mixed Lorentzian and Gaussian character [9] was, however, beyond the scope of this thesis.

Besides band positions, the individual areas of the deconvoluted bands are of interest. In a simple glass with only one type of network former, their share of the total fitted area is usually assumed to correspond to the fraction of their respective structural groups within the glass [147]. This is not the case for systems with several network formers as they differ in polarisability and

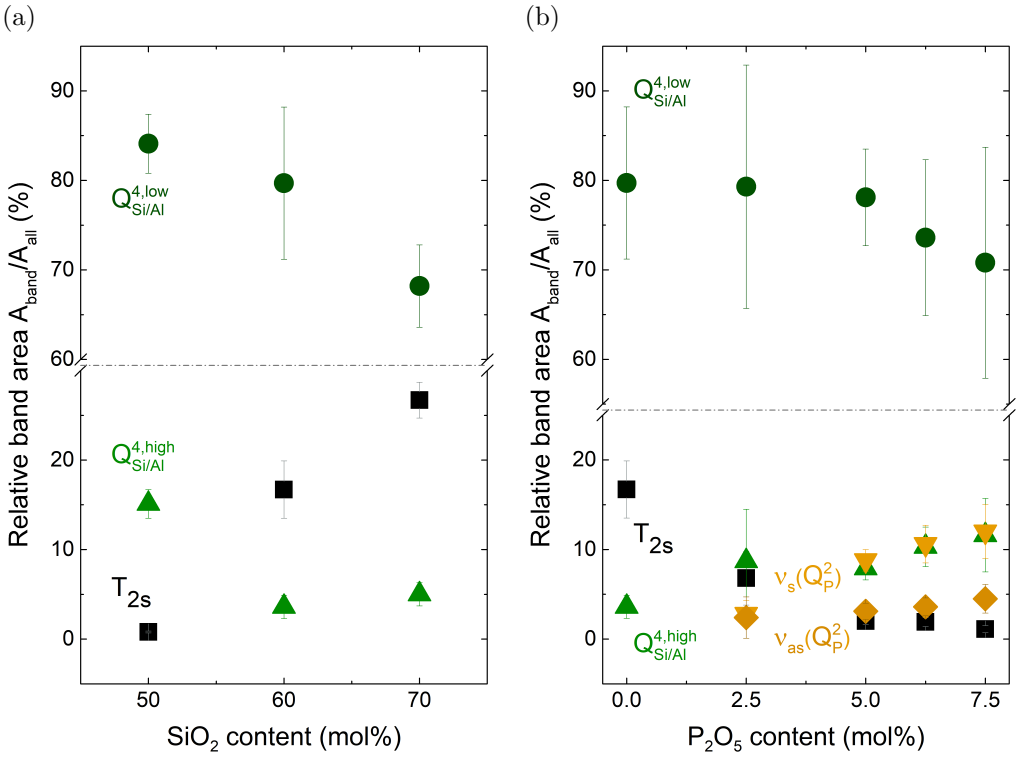

Figure 4.24: Relative areas of the deconvoluted Raman bands, in percent of the sum of all band areas, depending on glass composition. (a) Phosphate-free glasses and increasing SiO_2 content. (b) Constant 60 mol% SiO_2 and phosphate content increasing from 0 to 7.5 mol%.

thus in Raman scattering cross-section, see e.g. p. 126 of ref. [121]. Actually, also different Q groups differ in polarisability but this is sometimes ignored in the literature. As regards the glasses in this thesis, phosphate groups have a higher scattering cross-section than silicate or aluminate groups. Therefore, no quantitative analysis of the different amounts of structural groups can be derived from this deconvolution. Nevertheless, a comparison of relative band areas may yield information on the glass structure or on the quality of the deconvolution. For the sake of simplicity, the scattering cross-sections of silicate and aluminate groups will be assumed to be roughly equal. They will be treated together as aluminosilicate groups, following refs. [160, 163]. For phosphate-free glasses and increasing silica content (Figure 4.24a) the relative areas of the bands corresponding to the high symmetry vibrations $Q^{4,high}_{Si/Al}$ and $Q^{4,low}_{Si/Al}$ decreased with respect to the band of the less symmet-

Table 4.4: Relative area (in %) of the phosphate-related bands with respect to the sum of all band areas from deconvolution.

Glass	mol% P_2O_5	$\frac{A_{\nu_s+\nu_{as}(Q_P^2)}}{A_{\text{all bands}}}$ (%)
Si60P0	0	0 ± 0
Si60P2.5	2.5	5.2 ± 3.8
Si60P5	5	12.0 ± 2.1
Si60P6.25	6.25	14.2 ± 3.1
Si60P7.5	7.5	16.5 ± 4.6

ric T_{2s} mode. At the same time, the area ratio between $Q_{Si/Al}^{4,high}$ and $Q_{Si/Al}^{4,low}$ changed. A structural interpretation of these observations is difficult. Changing symmetries could indicate a changing medium range order. More likely though, the deconvoluted areas of T_{2s} and $Q_{Si/Al}^{4,high}$ are not reliable because of the abovementioned problem when trying to fit hidden bands. In a previously published deconvolution of metaluminous glasses [163], the relative areas of $Q_{Si/Al}^{4,high}$ and T_{2s} also seemed to arbitrarily change with glass composition, which may be owing to similar fitting difficulties. For the glass series with increasing phosphate content (Figure 4.24b), the area ratio $Q_{Si/Al}^{4,high}/T_{2s}$ increased. However, here the band areas have to be regarded as even less reliable as five bands were fitted to spectra with only one clear maximum. Therefore, no further deductions in terms of glass symmetry seem appropriate. Also, any interpretation of the relative band area of $Q_{Si/Al}^{4,low}$ will be refrained from because its value, except for glass Si70P0, remained within the limits of a large fitting error for both glass series (Figure 4.24).
Interestingly, for glass Si60P2.5 the errors of relative band area of $Q_{Si/Al}^{4,high}$ and $Q_{Si/Al}^{4,low}$ were noticeably larger than for the other glasses. Also, in this glass the relative areas of $\nu_s(Q_P^2)$ and $\nu_{as}(Q_P^2)$ were almost similar, whereas for higher phosphate contents the area of $\nu_s(Q_P^2)$ always was about three times that of $\nu_{as}(Q_P^2)$. Most probably, the fitting process was more ambiguous for Si60P2.5 because the phosphate bands were still weak.
The further development of the two phosphate bands (Figure 4.24b) matched the glass compositions, as their areas increased with increasing mol% P_2O_5. Interestingly, the area ratio of the combined phosphate bands relative to the sum of all fitted bands (Table 4.4) always was about two times the mol% of P_2O_5 within the glasses, thus reflecting the high Raman scattering cross-section of phosphate.
All deconvoluted bands presented here were rather broad, even though they

matched with previously published bands on phosphate-free glasses. Especially the phosphate bands were expected to be higher but more narrow. Constraining the bands to be more narrow may be beneficial for the physical meaning of the band assignments [9]. This was initially tried but discontinued because of convergence problems. A further improvement of this deconvolution including more narrow bands is desirable, but will require more elaborate work on the fitting process. The convergence problems may potentially be avoided by only constraining the band width for the first few fitting iterations. This may bring the fitted model close to a local minimum of χ^2 which is associated with physically meaningful constraints. Then, the constraints may be released for all following iterations, allowing the fitted model to converge into said local minimum.

4.7 Polarisability and optical basicity

The molar electronic polarisability, α_m, calculated using the Lorentz-Lorentz relationship (Equation 2.2), showed a pronounced increase with increasing phosphate content (Figure 4.25a) and decreased with increasing silica content (Figure 4.25b).

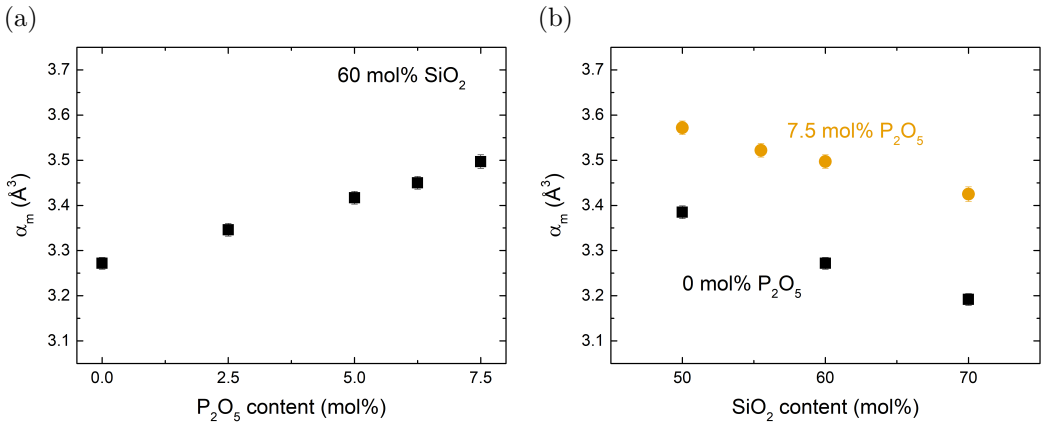

Figure 4.25: Dependence of the molar electronic polarisability on glass composition. (a) Increasing P_2O_5 content and constant 60 mol% SiO_2. (b) Increasing SiO_2 content and constant P_2O_5 contents of 0 mol% (black squares) and 7.5 mol% (orange circles).

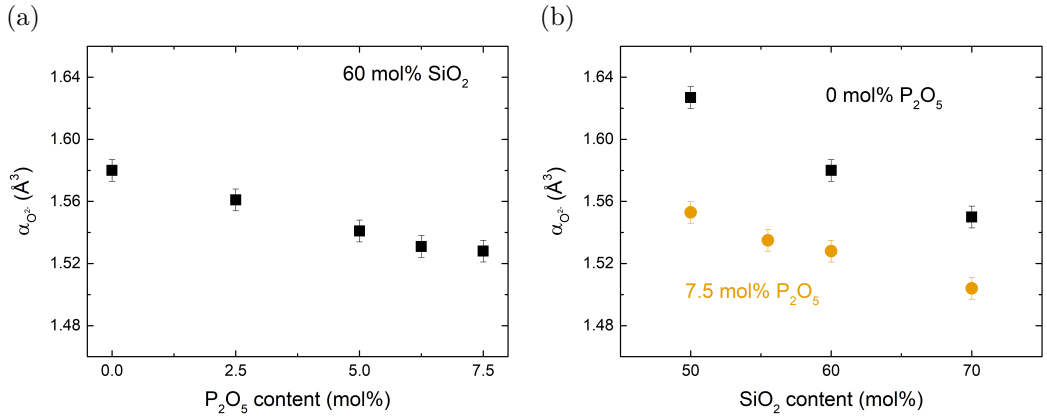

Figure 4.26: Dependence of the oxygen polarisability on glass composition. (a) Increasing P_2O_5 content and constant 60 mol% SiO_2. (b) Increasing SiO_2 content and constant P_2O_5 contents of 0 mol% (black squares) and 7.5 mol% (orange circles).

The partial molar oxygen polarisability, $\alpha_{O^{2-}}$, was calculated from α_m, removing the cationic contributions to polarisability (see Section 2.5). The oxygen polarisability decreased both with increasing phosphate and increasing silica content (Figure 4.26).
The theoretical optical basicity, Λ_{th}, calculated using Equation 2.1, represents an alternative measure of the electron density around the oxygen atoms and decreased both with increasing phosphate content and increasing silica content (Figure 4.27).

The molar electronic polarisability has a considerable impact on the intensity of Raman scattering. The high frequency region of the VV Raman spectra increased in intensity with increasing phosphate content in the glasses with 60 mol% SiO_2 (Figure 4.12). This increase in intensity is not only caused by the increasing phosphate content but also reflects the high Raman scattering power of phosphate that originates from its polarisability. Figure 4.25a confirms the intensity trend of the Raman spectra as the molar electronic polarisability increased with increasing phosphate content. Furthermore, the decrease in molar electronic polarisability with increasing silica content (Figure 4.25b) is also reflected in decreasing intensities of the VV Raman high frequency region with increasing silica content (Figures 4.13 and 4.14). For increasing silica content, more ionic $Na^+[AlO_4]^-$ tetrahedra are replaced by more covalent SiO_4 tetrahedra. This means a reduction of ionic bonding character. As a result, the electronic polarisability decreases,

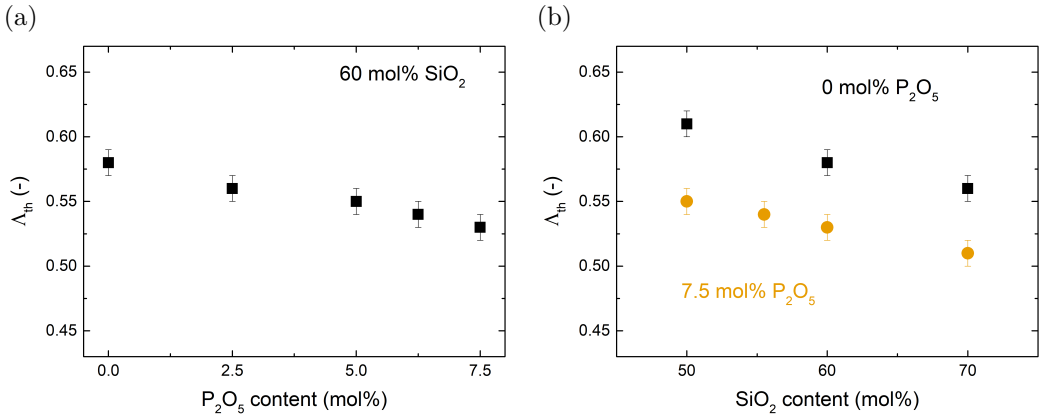

Figure 4.27: Dependence of the optical basicity on glass composition. (a) Increasing P_2O_5 content and constant 60 mol% SiO_2. (b) Increasing SiO_2 content and constant P_2O_5 contents of 0 mol% (black squares) and 7.5 mol% (orange circles).

because in covalent bonds the electron density is more evenly distributed between two atoms. Electron displacement by an external electromagnetic wave will therefore be less pronounced.
The above argument about the degree of ionic bonding was supported by the partial molar oxygen polarisability and the theoretical optical basicity. Both properties showed a clear decrease with increasing silica and phosphate content (Figures 4.26 and 4.27). This decrease corresponds to a shifting character of the chemical bonds from ionic to covalent (see Section 2.5). For the case of increasing silica content the increasing covalency is caused by the substitution of SiO_4 for $Na^+[AlO_4]^-$ tetrahedra.

Interestingly, with increasing phosphate content up to 7.5 mol%, the decrease in the optical basicity was comparable to that observed for varying the silica content over a range of 20 mol%. This cannot easily be explained by a simple withdrawal of Al^{3+} and Na^+ ions from the glasses as was done for the increasing silica content. Furthermore, with increasing phosphate content the oxygen polarisability decreased while the molar electronic polarisability increased (Figures 4.25a and 4.26a). The reason for phosphate incorporation decreasing the degree of ionic bonding of oxygen and at the same time increasing the electronic polarisability of the glasses may be explained by the strong Lewis acid character of P^{5+} cations. As strong electron acceptors they withdraw electron density from the surrounding oxygen anions. This may be illustrated in the following way: The bridging

oxygens within a PO_4 tetrahedron are deprived of electron density and thus can form more covalent bonds. The electron density that was withdrawn from the bridging oxygens migrates towards the central P^{5+} ion and is added to the delocalised electron system spanning from the P^{5+} ion over the non-bridging oxygens of the tetrahedron. The increased delocalised electron density adds to the overall electronic polarisability of the glass.

As oxygen polarisability and optical basicity are two different means to probe the electron density around oxygen, an analysis of the relationship between the two properties is worthwile. Duffy, one of the creators of the optical basicity concept [40, 43–46], found an empirical relationship between theoretical optical basicity, Λ_{th}, and oxygen polarisability, $\alpha_{O^{2-}}$, for oxide glasses [41]:

$$\Lambda_{th} = \frac{(3.133\ \alpha_{O^{2-}} - 2.868)^{\frac{1}{2}}}{1.567} - 0.362 \tag{4.1}$$

Equation 4.1 was first established for binary calcium silicate glasses [41] and since then has been applied to further oxide glass systems [88, 244], including simple aluminosilicate glasses [42]. For some coloured glasses the refractive index cannot easily be measured. In that case, Equation 4.1 has been successfully used to calculate electronic polarisability and refractive index from optical basicity [244]. However, a study by Velli et al. on oxyfluoride glasses showed that Equation 4.1 is not valid for all glass systems [235]. Also, Equation 4.1 is only strictly defined for optical basicities between 0.4 and 0.7 [41]. Fortunately, all glasses of the current study fell within that range.
All studied glasses matched well with Duffy's equation for simple oxide glasses (Figure 4.28). Minor deviations can only be seen under magnification (inset of Figure 4.28). This result is interesting because higher deviations were expected considering the complexity of different possible bond formations between the three network formers and the sodium. Taking this as an indicator for structural analysis, the overall treatment of the studied glasses as altered (alumino)silicate glasses may be justified.

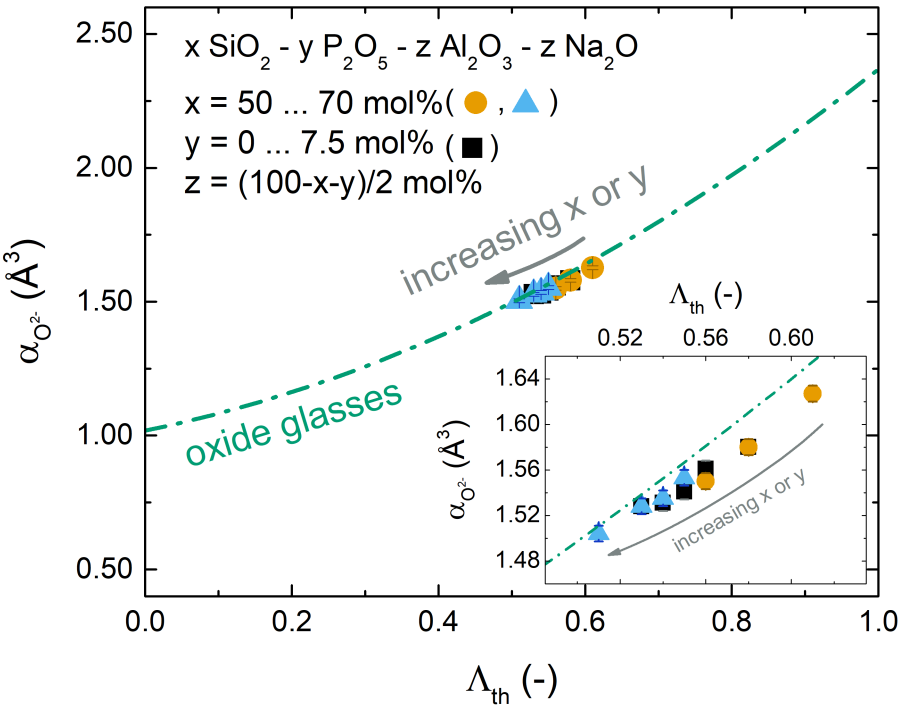

Figure 4.28: Relationship between oxygen polarisability and optical basicity for the studied glasses. The influence of compositional changes is indicated by the grey arrow. The green dash-dotted line represents Equation 4.1 as reported by Duffy [41] for simple oxide glasses. The inset shows a magnification of the studied compositional range. (Black squares) Glasses with 60 mol% SiO_2 and varying P_2O_5 content. (Orange circles) Glasses with 0 mol% P_2O_5 and (blue triangles) glasses with 7.5 mol% P_2O_5 and varying SiO_2 content.

4.8 Vibrational shifts and bonding

The shifts of the infrared and Raman high frequency region were linked to the changing ratios of the different network formers and the associated changes of average bond force constant which are owing to different strengths of the Al-O, Si-O and P-O bonds [167, 184]. While this correlation is established for changing Al/Si ratio [109, 141, 150, 160], its expansion to include phosphorus is new and invites the study of shifts in more detail.
IR and Raman high frequency envelopes shifted to higher wavenumbers both

with increasing SiO_2 and P_2O_5 content (Figures 4.12 to 4.14). The cross-polarisation analysis of Figure 4.18 suggests that all bands of the high frequency envelope shifted, not just individual ones. This is also supported by the results of Raman deconvolution (Section 4.6.5). This observation may be explained by a change in the average force constant upon changing glass composition if one assumes that all high frequency vibrations are coupled with each other, i.e. if the different network formers are evenly distributed. An even distribution of Si and Al atoms in phosphate-free metaluminous glasses has been supported by X-ray scattering experiments [222]. The shift of phosphate Raman bands for changing Al/Si ratio in Figures 4.12 and 4.14 suggests that phosphate is also linked to the aluminosilicate network.
However, the analysis of Figure 4.18 (p. 76) showed that the phosphate Raman band J shifted less than the aluminosilicate band H. While only Q^4 aluminosilicate units are expected in this glass system, the phosphate band J was partially assigned to Q^2_P units. Owing to the reduced connectivity of the Q^2_P unit to the network, frequency shifts of neighbouring aluminosilicate units may have less influence on the vibrational frequency of the phosphate band.
Interestingly, even in phosphate-free glasses not all bands shifted equally. The VV Raman high frequency maximum I shifted much stronger with changing Al/Si ratio than the IR maximum g (Figure 4.13 and Table 4.3). The VV Raman maximum corresponds to symmetric vibrations, the IR maximum to antisymmetric ones. Apparently the symmetric vibrations were more affected by the changing Al/Si ratio than the antisymmetric ones. Potentially not all vibrational modes were equally shared between the different network formers. Cicconi et al. [26] have suggested that aluminate tetrahedra in sodium aluminosilicate glasses rather become $Q^{4,low}$ units (smaller intertetrahedral bond angle) than $Q^{4,high}$ units. Their Raman analysis was supported by earlier molecular orbital calculations and X-ray scattering experiments [153], finding that an increase in aluminium content in a metaluminous system would decrease the average intertetrahedral bond angle. In infrared and VH Raman spectra, the high frequency maximum corresponded to different bands than $Q^{4,low}$, which may explain why they shifted less with changing Al/Si ratio.
Considering the findings above, the shift of the high frequency envelope cannot just be characterised by the shift of one band, but all bands should be taken into account. This was solved by calculating the centre of gravity (COG) of the high frequency envelope, after prior subtraction of a linear baseline from the integrated region. The shift of the COG represents an average of the shifts of all individual high frequency bands. In order to verify if the COG calculation is justified or if it oversimplifies the analysis of the band shifts, the COG shift had to be correlated with an independent measure of

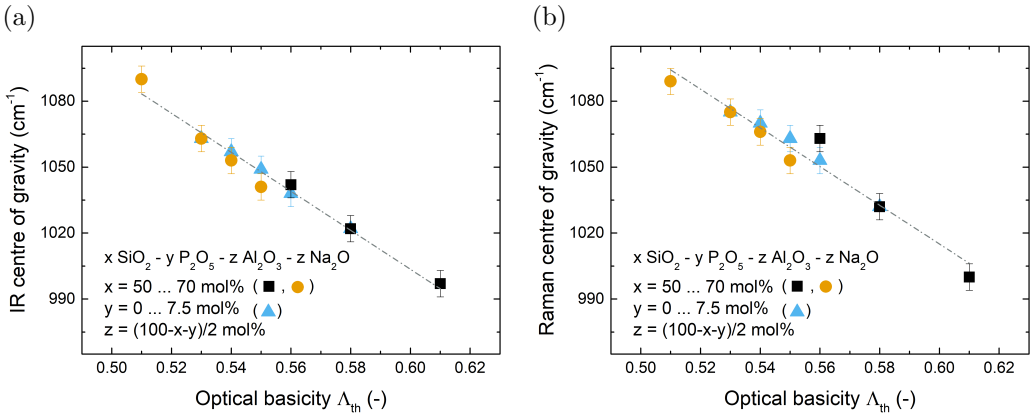

Figure 4.29: Shift of the centre of gravity (COG) of the high frequency envelope of IR (a) and Raman (b) spectra with respect to the optical basicity. Dash-dotted lines are merely guides to the eye. Blue triangles: 60 mol% SiO_2 and varying P_2O_5 content. Black squares: 0 mol% P_2O_5 and varying SiO_2 content. Orange circles: 7.5 mol% P_2O_5 and varying SiO_2 content.

vibrational frequency. A simple correlation of the COG shift with Al/Si ratio would neglect contributions by P and Na. In order to take all elements of the glasses into account, the theoretical optical basicity was chosen as an alternative measure of compositional change. Its link to the degree of covalent bonding also allowed to further approach the notion of bond force constants within this discussion. A decreasing optical basicity indicates a higher degree of covalent bonding (see Section 2.5). Since the more covalent bond is more directional, the bond strength along the bond axis increases [245]. This corresponds to a higher average bond force constant with decreasing optical basicity, which should result in higher vibrational frequency of the high frequency envelope.

Figure 4.29 shows an overview of the COG shift with variation of theoretical optical basicity. All three glass series are shown together in one diagram for infrared (4.29a) and Raman data (4.29b), but should first be discussed separately. Depending on the glass series, a decrease in optical basicity corresponds to either increasing SiO_2 or P_2O_5 content. For each series, Both the IR and Raman high frequency centres of gravity shifted roughly linearly towards higher wavenumbers with decreasing optical basicity. This matches with the above reasoning that a reduced degree of ionic bonding should lead to higher average bond strength and higher vibrational frequency.

Interestingly, the trends of IR and Raman COG shifts of all series almost fell

onto one line. This is indicated by the grey, dash-dotted lines in Figure 4.29, which are only meant to guide the eye and to highlight deviations. In case of the Raman data (Figure 4.29b) the three glass series showed higher deviation from a common slope. The reason for the deviating slopes of Raman data is that the Raman high frequency envelope was subject to major changes upon phosphate incorporation and shifts of the phosphate bands differed from the aluminosilicate band shifts, thus also influencing the COG shift. The infrared data appeared to agree better to a common slope (Figure 4.29a).
The good correlation between COG shifts of IR and Raman spectra with the theoretical optical basicity confirms that the calculation of the COG shift is a valid step to summarise the vibrational shifts of all glass components. However, caution is required considering the coincidence of the trends of the different glass series on one line. There are several limitations to the assumption of a linear correlation between optical basicity and spectroscopic shifts. First of all, a direct correlation between the changing average bond strength and the shifts of vibrational frequencies may only be true in the absence of network polymerisation changes. The only major depolymerisation in this thesis was found for increasing P_2O_5 content. However, depolymerisation should shift the high frequency envelope to lower wavenumbers [144, 147, 152, 204, 209], not to the observed higher ones. The increasing average bond strength caused by phosphate incorporation seems to outweigh the influence of depolymerisation on the vibrational shifts. Depolymerisation may, however, be responsible for the deviation of the Raman COG shift from the common line in Figure 4.29b. Another potential influence may be the different Raman scattering cross-sections of the three network formers, especially phosphate. The scattering power affects Raman band intensities, so that the deviation of the phosphate band shifts has a larger contribution to the COG calculation than contributions from aluminosilicate bands. This may also explain why the IR data (Figure 4.29a) showed less deviation from a common slope. The change in optical basicity may also be influenced by the coordination numbers of the network formers, see refs. [46, 216, 253] and p. 9 of ref. [25]. However, no coordination changes were detected by NMR spectroscopy (Section 4.5).
To the knowledge of the author, no study so far has compared Raman or IR high frequency shifts with optical basicity. Still, there is a model that successfully links certain vibrational band shifts to force constants and bond angles. The central force model by Sen and Thorpe [196] was already mentioned during the assignment of Raman bands (Section 4.6.3). In short, this model describes the development of two broad bands that can be correlated with the experimental low frequency and high frequency IR and Raman bands in highly polymerised glasses [56, 196]. Interestingly, their model predicts

that with increasing intertetrahedral bond angles and increasing bond force constants, the high frequency band will shift to higher frequencies and the low frequency band to lower frequencies. With regard to the results here, the shift of the high frequency band agrees with the observed COG shifts (Figure 4.29). The predicted shift of the low frequency region is interesting for the discussion of glass densification which will follow in Section 4.10.2. The model has also found application for calculation of bond angles and force constants of metaluminous glasses, following the assumption that they still resemble the fully polymerised network structure of vitreous silica [109, 194]. A key finding of those studies, supported by X-ray scattering [222], was that an increasing Al/Si ratio results in a decreasing average bond force constant and decreasing intertetrahedral bond angle [109, 194]. Although those studies did not consider optical basicity, their results are in qualitative agreement with the argument for Figure 4.29 that links higher vibrational frequency to higher bond force constants or lower optical basicity.
Nevertheless, the reason for the coincidence of the trends of the high frequency COG over optical basicity for all three glass series remains unclear. A reasonable next step would be to investigate this correlation for simple binary glass systems such as silicate and phosphate glasses. For these systems, the polymerisation and network former coordination are well known, so that their influence on the correlation between high frequency band shifts and optical basicity may be analysed. Depending on the outcome of these investigations, more complex glasses from the aluminosilicate or silicophosphate system may be tested. Based on that, the presented trends for phosphoaluminosilicate glasses may become easier to interpret.

4.9 Elastic response

For glasses with constant 60 mol% SiO_2 and increasing phosphate content (Figures 4.30 and 4.33a), G, K and E all decreased with increasing P_2O_5 content while ν remained roughly constant. For increasing silica content in phosphate-free glasses (Figures 4.31 and 4.33b) as well as glasses with 7.5 mol% P_2O_5 (Figures 4.32 and 4.33b), the trends were less unambiguous. G remained roughly constant for both glass series with 0 and 7.5 mol% P_2O_5. K and E decreased with increasing silica content, regardless of the phosphate content. However, the decrease in E was weak. For K, on the other hand, the decrease upon increasing silica content reached similar

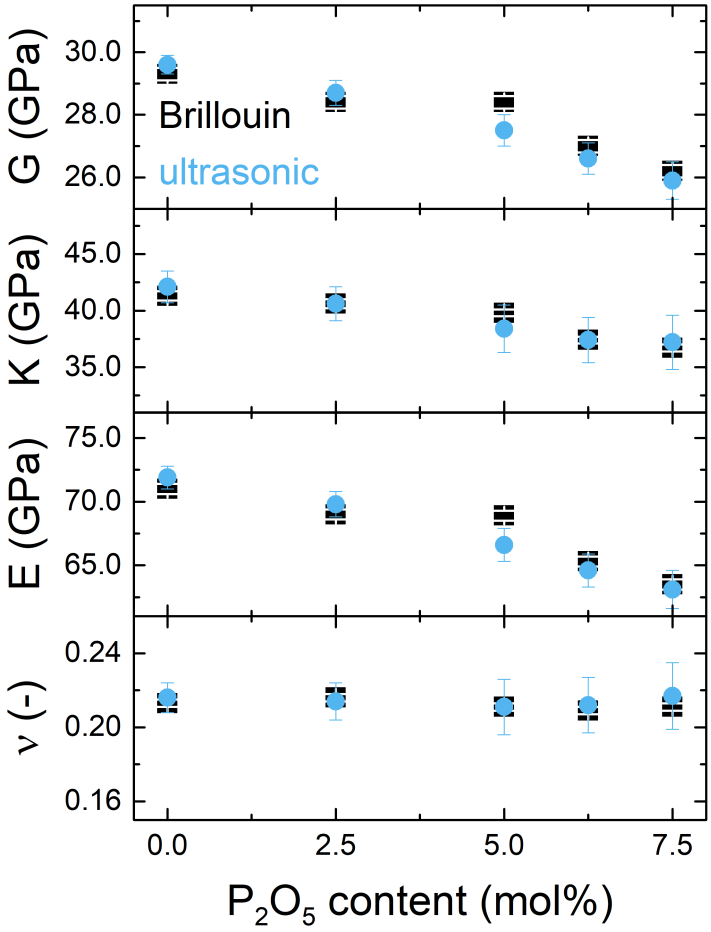

Figure 4.30: Comparison of elastic properties obtained by Brillouin spectroscopy (black squares) and ultrasonic echometry (blue circles) for glasses with constant 60 mol% SiO_2 and varying phosphate content. (From top to bottom line) Shear modulus (G), bulk modulus (K), Young's modulus (E) and Poisson's ratio (ν).

magnitudes as the decrease with increasing phosphate content. Poisson's ratio appeared to slightly decrease with increasing silica content.
Elastic properties obtained by ultrasonic echometry and Brillouin spectroscopy were in good agreement (Figures 4.30 to 4.32), reflecting the fact that both probed the sound velocities. As an exception of this observation, glass Si60P5 (5 mol% P_2O_5 in Figure 4.30) typically showed higher values of G, K and E for Brillouin spectroscopy than for ultrasonic echometry. This is most probably an outlier of the Brillouin sample of Si60P5, because all other data points followed a roughly linear trend. A Raman spectrum measured on the same sample and same spot also showed an outlier of the

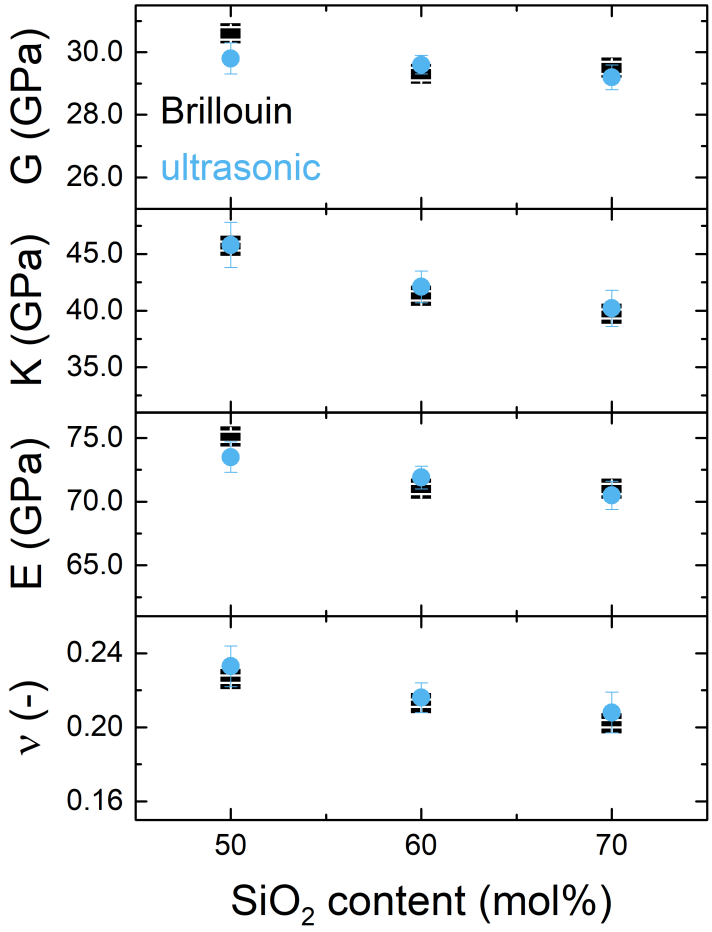

Figure 4.31: Comparison of elastic properties obtained by Brillouin spectroscopy (black squares) and ultrasonic echometry (blue circles) for glasses with constant 0 mol% P_2O_5 and varying silica content. (From top to bottom line) Shear modulus (G), bulk modulus (K), Young's modulus (E) and Poisson's ratio (ν).

frequency of phosphate band J (VV spectrum of Si60P5 in Figure 4.12, p. 67). An EDX analysis of this sample showed no significant compositional deviation with respect to the other glasses. However, the EDX and Brillouin measurements were carried out on different areas of the sample. Therefore, local compositional inhomogeneities may have led to the outlier.
The trends of nanoindentation modulus (Figure 4.33) agreed well with those found by ultrasonic echometry and Brillouin spectroscopy. Here as well, the sample with 5 mol% P_2O_5 was off the trend, indicating an outlier. The values of E obtained from nanoindentation were systematically lower by up to 5 GPa than the values from the other two methods. The difference is

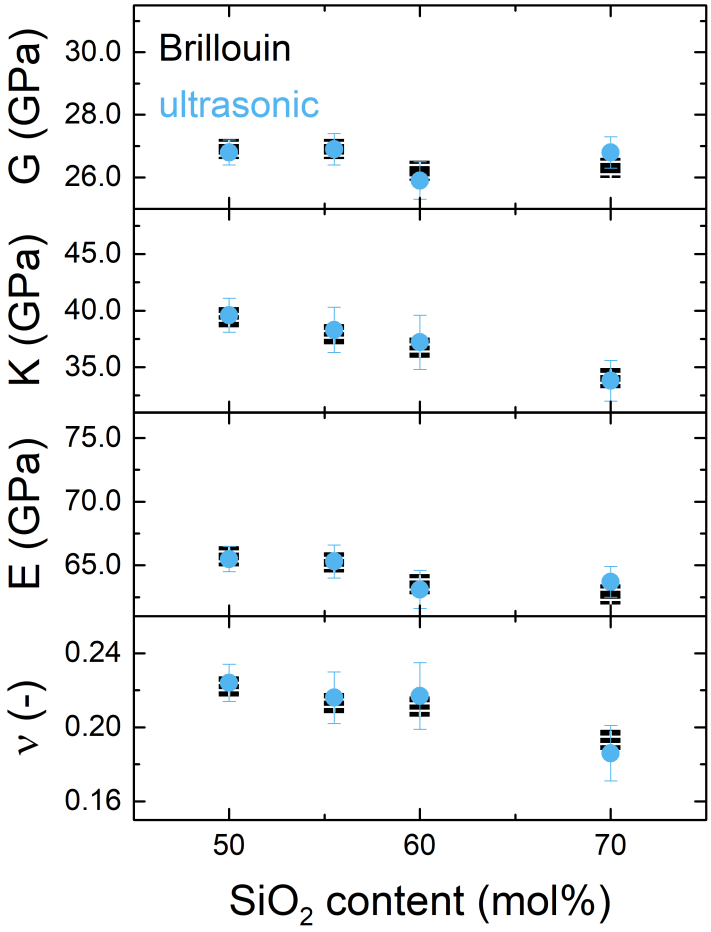

Figure 4.32: Comparison of elastic properties obtained by Brillouin spectroscopy (black squares) and ultrasonic echometry (blue circles) for glasses with constant 7.5 mol% P_2O_5 and varying silica content. (From top to bottom line) Shear modulus (G), bulk modulus (K), Young's modulus (E) and Poisson's ratio (ν).

small, however, and reflects differences in testing geometry as well as the fact that nanoindentation can only probe surface properties, which may be altered by contact with the atmosphere.

The absolute values obtained for the elastic properties agreed well with literature data on phosphate-free metaluminous glasses. For glass compositions Si50P0 and Si60P0, values of Young's modulus from 72 to 74 GPa have been reported (this thesis: 71 - 75 GPa) as well as Poisson's ratios from 0.2 to 0.228 (this thesis: 0.213 - 0.233) [225, 239]. To the knowledge of the author, no elastic properties have been reported so far

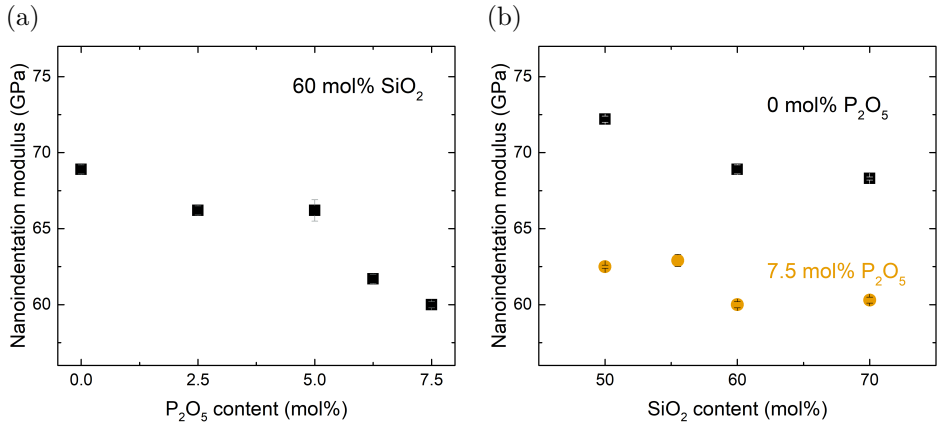

Figure 4.33: Dependence of the nanoindentation modulus on glass composition. (a) Increasing P_2O_5 content and constant 60 mol% SiO_2. (b) Increasing SiO_2 content and constant P_2O_5 contents of 0 mol% (black squares) and 7.5 mol% (orange circles).

on phospho-aluminosilicate glass compositions with relevance to this work. Only peralkaline basaltic glasses with negligible phosphate contents of 0.2 mol% have been investigated [116].

The decrease in E, G and K with increasing phosphate content (Figure 4.30) may be interpreted as decreasing network polymerisation. Additionally, the decrease may be correlated with a decreasing packing density upon phosphate incorporation, as suggested by Makishima and MacKenzie [128]. According to Rouxel, the packing density shows a non-linear correlation with elastic properties for a wide range of glass types [180, 181]. For increasing silica content, the polymerisation should remain unchanged, at least in the phosphate-free glasses. In case of phosphate-containing glasses, interactions between Na, P and Al may slightly influence polymerisation, as discussed in Section 4.6.4. If little to no change in polymerisation is assumed then the elastic properties should remain largely constant. This reasoning works well for G and still in an acceptable way for E (Figures 4.31 and 4.32). A clear contrast may be recognised between small changes of G and E upon increasing silica content, both for glasses with constant 0 mol% and 7.5 mol% P_2O_5, compared to larger changes with increasing phosphate content. However, the clear decrease in K with increasing silica content cannot be explained by constant polymerisation and neither can the small decreases of E and G.

The decreasing moduli may be explained by the decreasing packing density of the two glass series with 0 and with 7.5 mol% P_2O_5 (Figure 4.1, p. 52).

Even though the molar volume remained constant, indicating constant polymerisation, the decrease in packing density with increasing silica content indicates an increase in *free* volume. A glass with more free volume will be more compliant towards elastic deformation.
The changing degree of ionic bonding may not explain the decreasing moduli with increasing silica content. The increasing silica content results in an increasingly covalent bond character (Section 4.7). This should increase the strength of individual chemical bonds and thus raise the elastic moduli, which opposes the measured trends. Apparently the decreasing packing density has a much higher influence on the moduli than bond strength.
To conclude, there may be several contributions to modulus changes, but a change in packing density is the only one that may explain all measured trends.
Poisson's ratio remained constant with increasing P_2O_5 content (Figure 4.30) and thus decreasing polymerisation, even though Rouxel predicted an increase in ν for decreasing polymerisation [180]. However, his data showed wide scattering for highly polymerised glasses. Rouxel's predictions also include a decrease in Poisson's ratio with decreasing packing density [180]. For the glass series with increasing phosphate content, the packing density showed a clear decrease which cannot be correlated with the constant Poisson's ratio. However, the slight decrease in ν with increasing SiO_2 content (Figures 4.31 and 4.32) coincides with the simultaneously decreasing packing density, thus supporting Rouxel's findings [180]. The lack of change in ν with increasing phosphate content is mathematically justified, considering that ν includes a division of E by G (Equation 2.13). As the changes in E and G were very similar, no change in ν was to be expected.
As seen above and discussed in Section 2.8.1, the use of Poisson's ratio in the determination of glass structure is difficult. One additional observation may be noted, though. Rouxel's correlation between ν and packing density [180] apparently worked for substitution of SiO_4 for $Na^+[AlO_4]^-$ i.e. when the overall amount of network forming ions did not change. The correlation between ν and packing density did not succeed for the glasses with increasing phosphate content. In this series, the overall amount of network forming ions increased with increasing phosphate content, as $NaAlO_2$ was substituted by P_2O_5. However, whether the overall ratio of network formers to network modifiers correlates well with ν needs to be tested over a much wider range of glass compositions and systems and is beyond the scope of this thesis.

4.10 Plastic response

4.10.1 Hardness

General trends from micro- and nanoindentation agreed well and yielded decreasing hardness values with increasing phosphate content (Figures 4.34a and 4.35a). For increasing silica content (Figures 4.34b and 4.35b), hardness remained roughly constant for both methods, regardless of the phosphate content. However, Vickers hardness showed a slight decrease with increasing silica content in phosphate-free glasses. The hardness values measured by nanoindentation were always higher than the corresponding Vickers hardness by approximately 1 GPa. This may be ascribed to differences between the two methods. Microhardness only probes plastic deformation while nanohardness probes the combined plastic and elastic deformation, thus yielding higher hardness values [165].
The decrease in hardness with increasing phosphate content can be ascribed to lower network polymerisation, caused by P_2O_5 incorporation. The constant hardness with increasing silica content may be explained by constant network polymerisation upon substitution of SiO_4 for $Na^+[AlO_4]^-$ tetrahe-

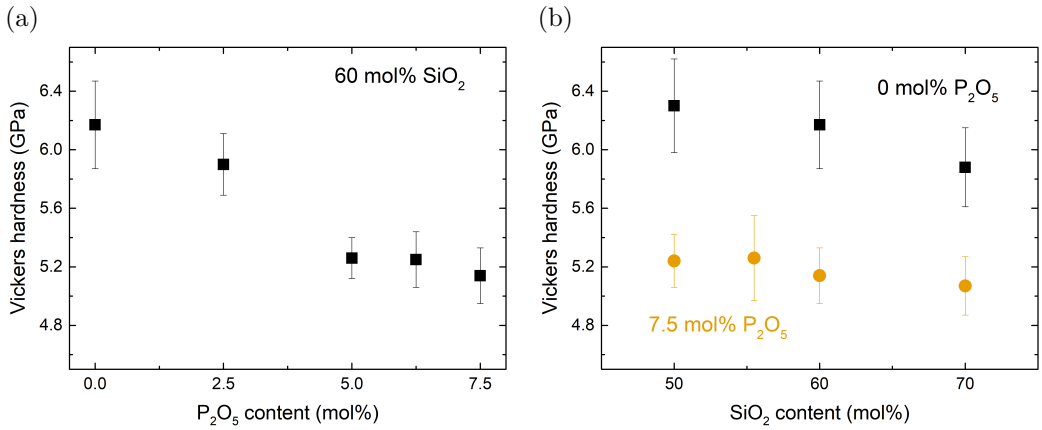

Figure 4.34: Dependence of Vickers microindentation hardness on glass composition. (a) Increasing P_2O_5 content and constant 60 mol% SiO_2. (b) Increasing SiO_2 content and constant P_2O_5 contents of 0 mol% (black squares) and 7.5 mol% (orange circles).

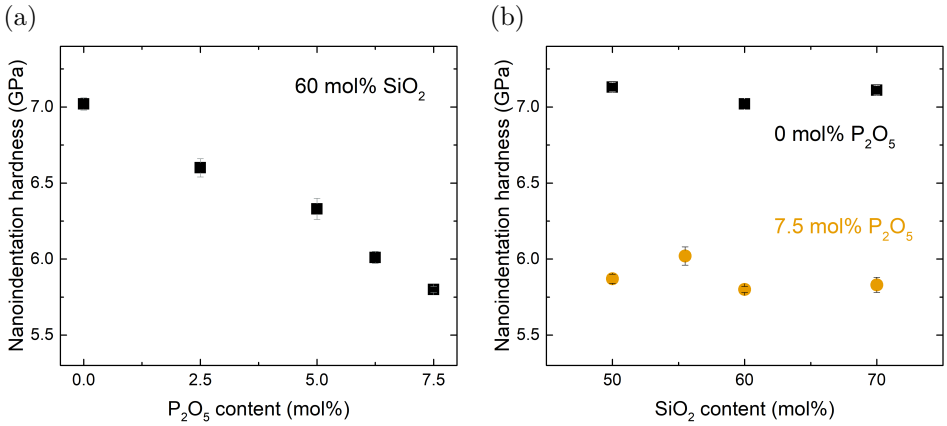

Figure 4.35: Dependence of the nanoindentation hardness on glass composition. (a) Increasing P_2O_5 content and constant 60 mol% SiO_2. (b) Increasing SiO_2 content and constant P_2O_5 contents of 0 mol% (black squares) and 7.5 mol% (orange circles).

dra. However, Möncke et al. [143] have illustrated that polymerisation alone may not always be sufficient to explain hardness trends. Lönnroth and Yue [116] have noted a weak correlation between hardness and density in peralkaline aluminosilicate glasses. Here, compositional trends of hardness were similar to those of E, thus also supporting a correlation of hardness with packing density [128]. Such a correlation of hardness with packing density was found for increasing P_2O_5 content, but not for increasing SiO_2 content. Instead, the constant hardness with increasing silica content could be correlated with constant molar volume (Figures 4.1 and 4.35b). The decreasing hardness with increasing P_2O_5 content (Figure 4.35b) was accompanied by increasing molar volume. For the studied glass system, a large molar volume appears to correlate with low hardness.

A similar decrease in hardness with increasing phosphate content up to more than 8 mol% has been reported by Tarragó et al. for basaltic glasses [220]. Zeng et al. [256] found hardness values between 5 and 5.5 GPa for peralkaline glasses with 5 mol% P_2O_5. This range agrees with the Vickers hardness of most phosphate-containing glasses of this thesis. The average Vickers hardness values found for the phosphate-free glasses (6 - 6.3 GPa) are in good agreement with a value of about 6 GPa reported by Tiegel et al. [225] for a glass of Si60P0 composition. Other literature hardness values of metaluminous glasses with various alkaline constituents ranged from 5.6 to 7.4 GPa [11, 206, 225].

4.10.2 Densification

The values found here for Poisson's ratio, ν, ranged between 0.2 and 0.24. Following the relationship between ν and plastic deformation mechanism reported by Yoshida et al. [254] and Sellappan et al. [195], this indicates that densification is the dominant plastic deformation mechanism. Additionally, a portion of shear deformation may also be expected.

Application of Raman spectroscopy to densification analysis Changes in the low frequency Raman region have been correlated with bond angle changes and thus with density changes [29, 36, 56, 183]. Densification shifts this region towards higher wavenumbers; however, the theoretical basis for this correlation has only been strictly defined for one-component glasses such as vitreous silica [56, 196]. The phospho-aluminosilicate glasses studied here carry three different network formers, all of them possessing different Raman scattering cross-sections. This may influence the Raman spectral shifts to currently unpredictable degrees. Even so, in the past the analysis of densification with Raman spectroscopy has not only been exercised on vitreous silica [29, 70, 77], but also on soda-lime silicate glasses [36, 90], borosilicate glasses [243] and aluminosilicate glasses [11, 172]. To the knowledge of the author, no correlation between densification and Raman spectra has yet been published for phospho-aluminosilicate glasses. All of the abovementioned studies correlated changes of the low frequency Raman region with densification. Even the studies on borosilicate and aluminosilicate glasses have not tackled the issue of having more than one network former. Instead, a phenomenological approach has been chosen for these glass systems. As long as silica remained the main network former, the shape of the low frequency Raman envelope was close enough to that of vitreous silica to assume similar behaviour. The same assumption will be considered valid for the phospho-aluminosilicate glasses of this thesis, because of their high degree of polymerisation and the clearly observable changes of the low frequency Raman region upon densification.
Changes in the medium frequency region (Figure 3.4, Raman band F at $700\,\mathrm{cm}^{-1}$, $[AlO_4]^-$ stretching) were not taken into account here. There was no reason to assume a change in aluminium coordination upon Vickers indentation that would affect Raman band F for a metaluminous composition. The formation of higher-coordinated aluminium upon compression is likely for peralkaline compositions but not for metaluminous ones [11, 74]. A weak

intensity increase in the medium frequency region upon densification is assumed to be caused by partial overlap with the low frequency bands instead.

Densification analysis A Raman map of a Vickers indentation (Figure 4.36, colour indicates position of the centre of gravity) showed that there was a clear shift of the low frequency centre of gravity (COG) towards higher wavenumbers when comparing the indentation region (light blue to yellow) with the non-indented glass (dark blue). The highest COG shift was found in the centre of the indentation. The indentation centre was assumed to be more densified than outer regions. This was also shown by Kassirbodon et al. [90] using finite element simulation. The finding of highest COG shifts in the indentation centre therefore supports the above argument that Raman spectral shifts can be applied to quantify densification in phospho-aluminosilicate

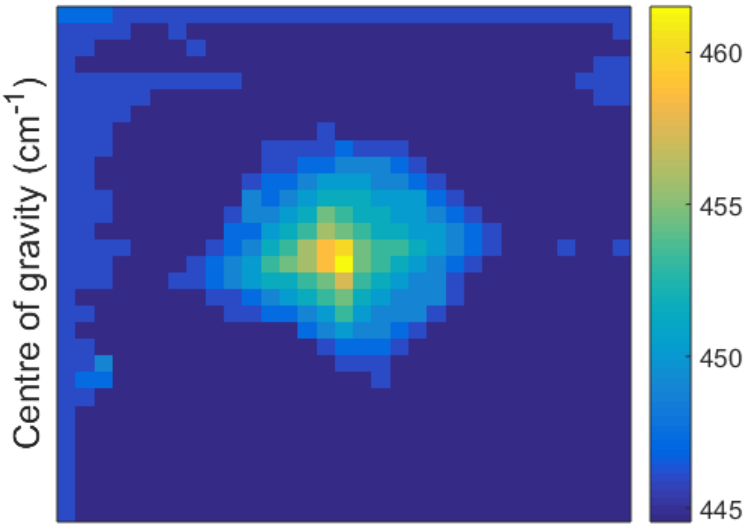

Figure 4.36: Raman map of a Vickers indentation (load 981 mN) on a selected glass. Each pixel corresponds to one Raman spectrum. The distance between two pixels is 1 μm, giving total dimensions of $31 \times 31\,\mu m^2$. The colour code shows the position of the low frequency centre of gravity for each pixel. The centre of the indentation (yellow), which corresponds to highest densification, displays the highest shift of the centre of gravity compared to non-indented glass (dark blue).

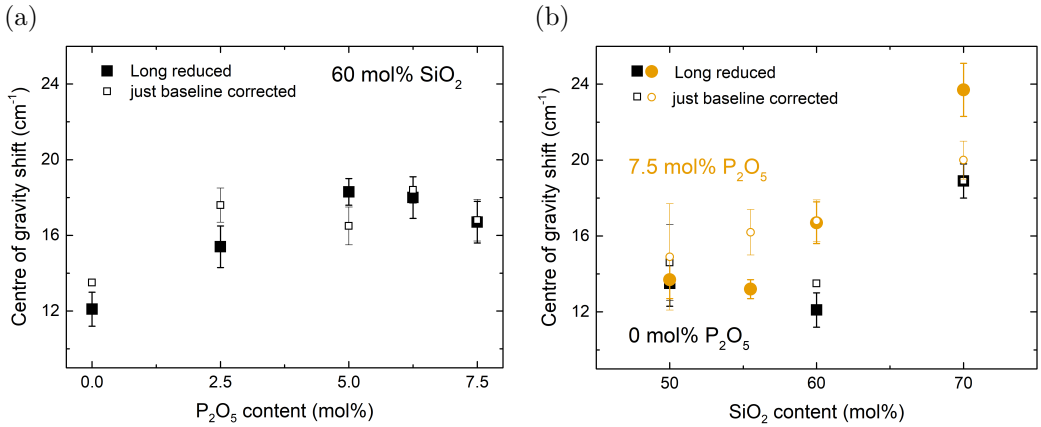

Figure 4.37: Shift of the low wavenumber centre of gravity (COG) upon Vickers indentation (981 mN) for the studied glass compositions. (a) Increasing P_2O_5 content and constant 60 mol% SiO_2. (b) Increasing SiO_2 content and constant P_2O_5 contents of 0 mol% (black squares) and 7.5 mol% (orange circles). Filled and empty symbols refer to spectral processing routes with and without Long reduction, respectively.

glasses.

Two different spectral processing routes were compared to assess the influence of spectral treatment on densification analysis (for details see Section 3.10.2). One route was a simple baseline correction, the other one additionally involved the Long reduction (Equation 3.4). The absolute COG positions typically differed by 30 to 40 cm^{-1} for the two different routes, but the corresponding COG shifts upon indentation differed by less than 4 cm^{-1} (filled and empty symbols in Figure 4.37). As a conclusion, the Long reduction does not seem to overly affect the evaluation of densification and both data processing routes may be regarded as equally applicable.

For increasing phosphate content (Figure 4.37a), the COG shift seemed to increase to a constant value for the baseline-treated data while the data obtained after Long reduction showed a maximum of the COG shift for 5 mol% P_2O_5. Here, however, the decrease of the COG shift towards 7.5 mol% P_2O_5 was low.

For increasing silica content (Figure 4.37b), the COG shift seemed to increase non-linearly. The phosphate-free glass series showed a minimum of the COG shift at 60 mol% SiO_2 for both processing routes. The minimum was within the error range for the data that was not subjected to the Long reduction.

For the glasses with 7.5 mol% P_2O_5, an increasing silica content led to an

increase in the COG shift for both processing routes. The only exception was an apparent minimum of the COG shift for the glass with 55.5 mol% SiO_2 (Figure 4.37b, orange filled circles). This minimum was within the error range, though.
As an additional observation, an increase in phosphate content did not significantly affect the COG shift for the glasses with 50 mol% SiO_2 (Figure 4.37b), regardless of the processing route.
The increasing COG shift upon phosphate incorporation in glasses with 60 mol% SiO_2 (Figure 4.37a) indicates higher densification upon indentation and may be explained by the lower packing density of the phosphate-containing glasses (Figure 4.1, p. 52). When equally loaded, a less densely packed glass should be more readily densified than a densely packed one. This, however, does not explain why the COG shift remained unchanged for the glasses with 50 mol% SiO_2 upon phosphate incorporation (Figure 4.37b), despite decreasing packing density. Potentially, the deformation mechanism changes with SiO_2 content.
The non-linear trends of the COG shift with increasing P_2O_5 content (either maximum trend or reaching of a constant value, depending on the processing route, Figure 4.37a) may be related to increasing glass depolymerisation upon increasing P_2O_5 content. As shown by Bechgaard et al. [11], the degree of polymerisation may affect the deformation mechanism of aluminosilicate glasses.
The increasing COG shift with increasing silica content may be explained by the lower packing density of the high-silica glasses. The apparent non-linearity of this trend towards lower silica contents (Figure 4.37b) may be related to the observation that phosphate incorporation did not significantly affect the COG shift of glasses with low silica content. Potentially, the non-linearities may be caused by underlying changes of the deformation mechanism. A more elaborate nanoindentation study may help to identify such a change in deformation mechanism: One may study the pileup volume around nanoindentations, which should become larger the more shearing and the less densification is involved in the deformation [254].

4.11 Cracking response

Crack resistance did not show any trend for increasing phosphate content (Figure 4.38a). Data scattered between crack resistances of 4 to 8 N. By con-

trast, two different trends could be found for the glasses with constant 0 and 7.5 mol% P_2O_5 when increasing the silica content (Figure 4.38b). The crack resistance of glasses with 0 mol% P_2O_5 slightly increased with increasing silica content. For the glasses with 7.5 mol% P_2O_5, crack resistance decreased markedly from 50 to 55.5 mol% SiO_2 and then decreased within the error limit for further increasing silica content.
The slight increase in crack resistance with increasing silica content in phosphate-free glasses confirms findings by ref. [73]. However, as the concept of crack resistance is rather new [91], there is only little literature data available on the crack resistance of aluminosilicate glasses. Bechgaard et al. [11] have recently reported crack resistances between 1 and 3 N for a glass of Si50P0 composition. This is in agreement with the value found in this thesis (3.1 N). Unfortunately no literature data was found that could confirm the trends of crack resistance upon increasing silica content with comparable glass compositions. Also, there was no literature data available on the crack resistance of phospho-aluminosilicate glasses.
The range of data scattering observed for increasing phosphate content (Figure 4.38a) is similar to the range spanned by the crack resistance trends for increasing silica content (Figure 4.38b). Therefore, the apparent trends in Figure 4.38b may be coincidental and will not be discussed further.
To improve reliability of crack resistance measurements, an even higher number of indentations would be needed to improve statistics. Also, atmospheric

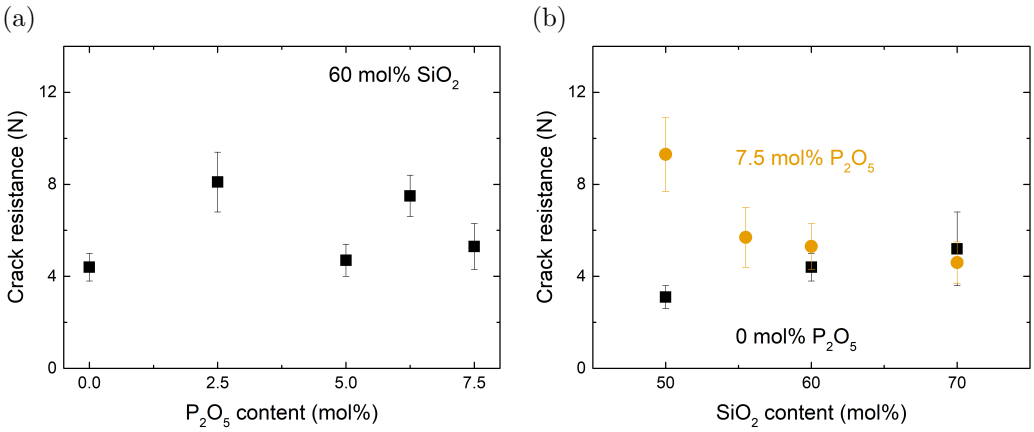

Figure 4.38: Dependence of the crack resistance on glass composition. (a) Increasing P_2O_5 content and constant 60 mol% SiO_2. Data scattering is discussed in the text. (b) Increasing SiO_2 content and constant P_2O_5 contents of 0 mol% (black squares) and 7.5 mol% (orange circles).

humidity may affect the measurements and should be avoided by measuring under protective atmosphere or vacuum. Moreover, cracks usually span larger distances (several μm) than the phenomena governing the other properties measured in this study. Therefore, crack resistance is probably also affected by sample inhomogeneity. Measures to increase glass homogeneity should be taken to improve the reliability of crack resistance experiments in spite of the high viscosity of the melts, such as using larger batches and longer melting times.

4.12 Rate-dependent response

For increasing phosphate content (Figure 4.39a) the strain rate sensitivity slightly increased. For both glass series with constant 0 and 7.5 mol% P_2O_5 the strain rate sensitivity showed a maximum value in the range between 50 and 60 mol% SiO_2 (Figure 4.39b).
All resulting strain rate sensitivities in this thesis fit well within the relationship between strain rate sensitivity and Poisson's ratio for glasses shown by Limbach et al. [114]. The strain rate sensitivities ranged from 0.012 to 0.018 for ν values between 0.20 and 0.24, agreeing with similar values for

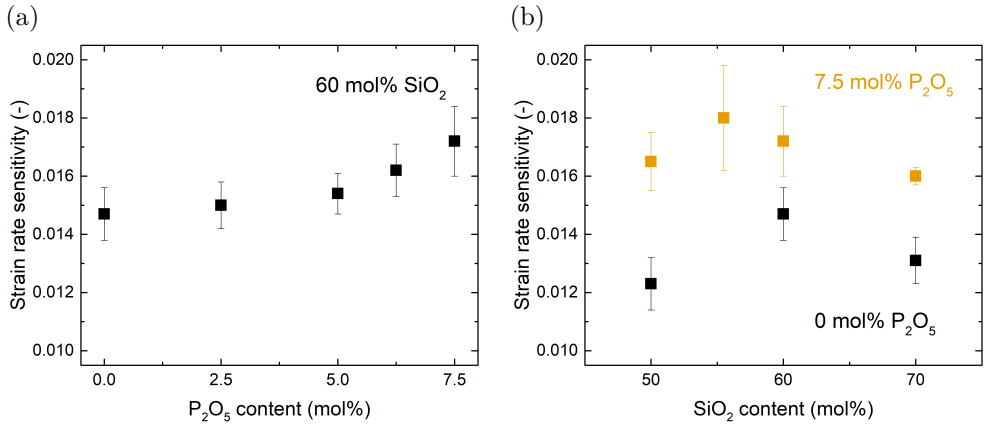

Figure 4.39: Dependence of the strain rate sensitivity on glass composition. (a) Increasing P_2O_5 content and constant 60 mol% SiO_2. (b) Increasing SiO_2 content and constant P_2O_5 contents of 0 mol% (black squares) and 7.5 mol% (orange circles).

soda lime silicate glasses [114]. These strain rate sensitivities are rather low, yet common over many different glass systems [114].
The increasing strain rate sensitivity with increasing phosphate content (Figure 4.39a) may potentially be explained by the decreasing packing density and network polymerisation upon phosphate incorporation. Both trends should account for more free volume within the glass. This additional free volume might allow atoms to undergo local displacement and therefore react more easily when faced with sudden increases of indentation strain rate. On the other hand, closely packed atoms cannot easily relocate upon strain. Therefore any sudden increase in strain rate should lead to an immediate material response in the form of a hardness increase.
Nevertheless, a complete structural explanation of the increased strain rate sensitivity has to be more complex. For increasing silica content, the results show no correlation between strain rate sensitivity and density. Here, the non-linearity of strain rate sensitivity correlates with no other property measured in this thesis.
A tentative structural hint may be obtained from metaluminous minerals of stoichiometry comparable to that of the phosphate-free glasses. Glass Si50P0 has the same stoichiometric composition as the mineral nepheline ($NaAlSiO_4$). The composition of glass Si60P0 lies between nepheline and jadeite ($NaAlSi_2O_6$), the latter corresponding to 66.67 mol% SiO_2. The composition of glass Si70P0 lies between jadeite and albite ($NaAlSi_3O_8$), with albite corresponding to 75 mol% SiO_2. The crystal structures of nepheline, jadeite and albite are hexagonal, monoclinic and triclinic, respectively, see e.g. the RRUFF mineral database, entries R040025.1, R050220 and R040068.1 [106]. Potentially, the maximum in strain rate sensitivity upon increasing silica content may correspond to an underlying change within the glasses' medium range structure which bears similarities to the change of the corresponding crystal structure. However, this is a mere hypothesis. If there really is a change in medium range structure then a supporting measurement would be required. As a suggestion for further structural insight, the rate-dependent mechanical response should be studied accompanied by an in-situ structural probe. The strain rate sensitivity in metals is sometimes correlated with a theoretical activation volume that is needed by the rate-dependent deformation mechanism [6, 236]. In the past the densified volume of glasses under indentation has been simulated and measured ex-situ by analysing the pile-up volume around indentations [10, 182, 195, 254]. An in-situ sampling of densified volume during strain rate jump tests might be feasible using e.g. X-ray microscopy in combination with an indenter.

5

Conclusion

The aim of this thesis was to examine the effect of phosphate on the mechanical properties of metaluminous aluminosilicate glasses with a particular focus on the underlying changes in the structural setup. Three series of glasses were prepared to investigate the effects of increasing phosphate content and variation of silica content in phosphate-containing glasses as well as phosphate-free reference glasses. Glass synthesis was found to be feasible without significant losses of P_2O_5.
All glasses were extensively characterised in terms of mechanical properties by measuring elastic properties and hardness with several experimental approaches each. Furthermore, densification, crack resistance and strain rate sensitivity were studied. Apart from the mechanical properties, thermal behaviour, density and refractive index were measured to aid in the interpretation of structural changes. Glass structure was characterised by a combined spectroscopic approach of infrared, Raman (parallel polarised and cross-polarised) and solid-state NMR spectroscopy, the latter by a collaboration partner. Interpretation of the glass structure was carried out following the notions of network polymerisation, packing density and the degree of ionic bonding.

- The combined use of IR, Raman and solid-state NMR spectroscopy showed that phosphate associated with both sodium and aluminium, thus forming charge-balanced groups of depolymerised Q^2_P units (metaphosphate) and fully polymerised Q^4_P units (Al-O-P bonds). This is in agreement with previous studies on phosphate bonding in metaluminous aluminosilicate glasses [62, 119, 146]. SiO_4 and $[AlO_4]^-$ tetrahedra maintained their Q^4 state.
  The combination of infrared with VV and VH Raman spectra and their respective information on group symmetry allowed to establish a detailed band assignment for the glasses, which further paved the way for the use of vibrational spectra in the analysis of densification and ionicity. VV and VH Raman spectra also revealed that a phosphate Raman band shifted less compared to aluminosilicate bands upon compositional change. This was attributed to reduced coupling of the Q^2_P groups to the rest of the network, owing to their NBO. The observation that this phosphate band also shifted upon changing silica content indicated that phosphate was incorporated into the aluminosilicate network.
  While IR and Raman spectroscopy could not distinguish between Q^2_P and Q^4_P groups, solid-state NMR provided a complementary approach for their identification [161]. An even more detailed structural analysis could be feasible by supporting the complementary spectroscopic techniques with simulations of the vibrational spectra, as was already done for other complex glasses [30].

- The incorporation of phosphate by substituting P_2O_5 for $NaAlO_2$ was assumed to increase molar volume and decrease polymerisation. The molar volume increase was confirmed by density data, the decreasing polymerisation by spectroscopy and by a strong decrease of the glass transition temperature.
  A simultaneous decrease of hardness was attributed partially to decreasing polymerisation and partially to increasing molar volume. Refractive index and elastic moduli were also found to decrease, which was mainly attributed to the decrease in density. However, the decreasing refractive index may also partially be caused by the formation of Al-O-P bonds [37]. Furthermore, the degree of ionic bonding was found to decrease with increasing phosphate content.
  The significant decrease in T_g will allow for easier processing of these glasses when compared to phosphate-free aluminosilicate glasses. Another advantage is the fact that phosphate impeded glass crystallisa-

tion. This was attributed to Al-O-P bond formation and thus integration of phosphate into the network structure, and is confirmed by previous findings on the stability of phospho-aluminosilicate glasses close to metaluminous composition [65].

- Variation of the silica content by substituting SiO_4 for $Na^+[AlO_4]^-$ was assumed to maintain nearly constant polymerisation. This was confirmed by constant hardness and molar volume, and also by nearly constant elastic moduli E and G. Also the glass transition temperature changed very little, indicating negligible change of polymerisation.
  A slight decrease of all elastic properties, most pronounced for the bulk modulus K, did not match the notion of constant polymerisation but could be explained by decreasing packing density [181]. A decreasing refractive index with increasing silica content could also be explained by decreasing density.
  The detailed changes of T_g were more complicated, though, showing an increase for phosphate-free glasses but a decrease for phosphate-containing glasses upon increasing silica content. As the degree of ionic bonding decreased with increasing silica content, the stronger covalent character of chemical bonds in high-silica content glasses may explain the slight increase of T_g in phosphate-free glasses.

- The decreasing glass transition temperature with increasing SiO_2 content in phosphate-containing glasses was interpreted as a competition between aluminate and phosphate groups for charge-balancing sodium. Such a competition may lead to slight changes of glass polymerisation which, as a result, affect T_g. This interpretation was supported by a shift of the far-infrared (FIR) sodium band, which indicated an association of sodium with phosphate for increasing SiO_2 content. In the glass series with increasing P_2O_5 content such a FIR band shift also indicated increasing association of sodium with phosphate.
  Interestingly, with increasing silica content in the phosphate-free glass series the FIR band indicated weaker bonds between Na and its environment, even though no change in the charge-balancing role of Na associated with Al was expected here. This may be explained by ionic interactions between neighbouring $Na^+[AlO_4]^-$ tetrahedra. Such interactions would become weaker with decreasing numbers of $Na^+[AlO_4]^-$ groups upon increasing SiO_2 content. This interpretation is tentative, though, and may be tested by synthesising metaluminous glasses with less than 50 mol% SiO_2. This would allow to investigate whether further FIR shifts occur for glasses with a larger number of $Na^+[AlO_4]^-$ than SiO_4 tetrahedra.

While many glass studies focussed on the network formers in glasses, the interest in the role of alkaline ions in aluminosilicate glasses has recently increased [110]. The successful linking of the FIR sodium band in this thesis with the anomalous T_g trend of phosphate-containing glasses showed that a more detailed study of the role of alkaline ions can yield advances in structural understanding. More insight could possibly be gained by studying Na-O bond length and Na coordination. Also, a deeper investigation of the competition between aluminate and phosphate for sodium is suggested. A quantification of the exact relative amounts of the various phosphate and aluminate species in the glasses and their association with sodium would be required to fully understand the interactions between the different network formers in phospho-aluminosilicate glasses.

- The degree of ionic bonding was determined by calculating oxygen polarisability and theoretical optical basicity, showing that the degree of ionic bonding decreased both with increasing P_2O_5 and increasing SiO_2 content. Furthermore, the relationship between optical basicity and oxygen polarisability was found to follow Duffy's empirical expression for simple oxide glasses [41]. This is remarkable considering the complexity of the studied system with three network formers. The calculation of oxygen polarisability and optical basicity required the assumption of glass composition matching the nominal values. In future work, the calculations could be supported by experimentally measuring the optical basicity, using glasses containing probe ions such as Pb^{2+}.

- One particularly interesting finding of this thesis was that optical basicity correlated with shifts of the high frequency bands of both IR and Raman spectra. The spectral shifts were interpreted in terms of changing glass composition, with P-O bonds increasing the average bond strength of the glasses when compared to Si-O and Al-O bonds. The observation that all high frequency bands shifted showed that the three network forming species underwent vibrational coupling and influenced each other's frequencies.
  Optical basicity seems to take this averaged bond strength into account by indicating changes from weaker ionic bonding to more directional and thus stronger covalent bonding. The correlation between optical basicity and vibrational shifts worked well over all three glass series, with minor deviations mostly for the Raman spectral shifts.
  So far, such shifts of high frequency IR and Raman bands have only been linked to either the strength of a single bond type (P-O bonds in phosphate glasses [167]) or to changing ratios of two network for-

mers (Al/Si ratio in aluminosilicate glasses [32, 140, 194]). None of these approaches can satisfactorily describe the situation in phosphoaluminosilicate glasses. The new correlation with optical basicity may be more versatile as basicity takes all glass components and their stoichiometry into account. However, such correlation needs to be investigated for more simple glass compositions first, to verify its wider applicability.

- The study of mechanical properties by indentation opened up the question of plastic deformation mechanism. Based on Poisson's ratio, the deformation mechanism of the studied glasses should be mainly densification, with some contributions from shearing [195]. The glass densification in Vickers indentations was investigated by determining the corresponding centre of gravity shifts of the low frequency Raman spectra. Glasses with lower initial density showed larger centre of gravity shifts upon densification, indicating higher densification. However, the results were non-linear over glass composition, which was tentatively attributed to a change in deformation mechanism. To further verify this, a study of the indentation volume pileup would be required to estimate the relative contributions of densification and shearing to the deformation of each glass [254].

- During mechanical analysis, the strain rate sensitivity and crack resistance were also investigated, but left some unanswered questions. While an increasing strain rate sensitivity with increasing phosphate content may be related to the corresponding depolymerisation and decrease in density, a non-linear trend of strain rate sensitivity found for increasing silica content could not yet be sufficiently explained. Considering that the determination of glass strain rate sensitivities is a recent technique [114], a better understanding may be possible in the future.
  Crack resistance scattered widely upon increasing phosphate content, rendering any interpretation in terms of composition pointless. Most likely, this problem may be overcome by synthesising samples of higher homogeneity and conducting the experiments under controlled atmosphere.

As a final remark, the investigation of glasses from the model composition SiO_2 - Al_2O_3 - Na_2O - P_2O_5 allowed to identify potential structural reasons behind the observed property trends. New, complex interactions were found which require further study, such as the competition between aluminate and

phosphate for charge-balancing by sodium. Nevertheless, the findings in this thesis provide a basis for tailoring thermal, optical and mechanical glass properties by simply varying the P_2O_5 or SiO_2 content. Furthermore, this thesis presents the first comprehensive analysis of the mechanical properties of metaluminous phospho-aluminosilicate glasses. The results may be useful for engineering applications as well as for geoscientific studies with regard to magmatic densification. So far, there is no comparable mechanical analysis available for phospho-aluminosilicate glasses of peralkaline or peraluminous compositions. An expansion of the presented dataset is thus desirable. The non-metaluminous compositions may open up even more different structural roles for sodium and aluminium.

Bibliography

[1] Affatigato, M., editor [2015]. *Modern Glass Characterization*. John Wiley & Sons, first edition. ISBN 978-1-118-23086-2.

[2] Aines, R. & G. Rossman [1984]. 'Water in minerals? A peak in the infrared.' *Journal of Geophysical Research*, **89**(B6), pp. 4059–4071.

[3] Aitken, B., R. Youngman, R. Deshpande & H. Eckert [2009]. 'Structure-Property Relations in Mixed-Network Glasses: Multinuclear Solid State NMR Investigations of the System $x\,Al_2O_3 : (30 - x)\,P_2O_5 : 70\,SiO_2$.' *Journal of Physical Chemistry C*, **113**, pp. 3322–3331.

[4] Ando, M., O. Benzine, Z. Pan, J.-L. Garden, K. Wondraczek, S. Grimm, K. Schuster & L. Wondraczek [2018]. 'Boson peak, heterogeneity and intermediate-range order in binary SiO_2 - Al_2O_3 glasses.' *Scientific Reports*, **8**, pp. 14.

[5] Ardia, P., A. Di Muro, D. Giordano, D. Massare, C. Sanchez-Valle & M. Schmidt [2014]. 'Densification mechanisms of haplogranite glasses as a function of water content and pressure based on density and Raman data.' *Geochimica et Cosmochimica Acta*, **138**, pp. 158–180.

[6] Asaro, R. & S. Suresh [2005]. 'Mechanistic models for the activation volume and rate sensitivity in metals with nanocrystalline grains and nano-scale twins.' *Acta Materialia*, **53**, pp. 3369–3382.

[7] Baasner, A., B. Schmidt & S. Webb [2013]. 'The effect of chlorine, fluorine and water on the viscosity of aluminosilicate melts.' *Chemical Geology*, **357**, pp. 134–149.

[8] Balzer, R., H. Behrens, S. Reinsch & M. Fechtelkord [2019]. 'Structural investigation of hydrous phosphate glasses.' *Physics and Chemistry of Glasses: European Journal of Glass Science and Technology Part B*, **60**, pp. 49–61.

[9] Bancroft, G., H. Nesbitt, G. Henderson, C. O'Shaughnessy, A. Withers & D. Neuville [2018]. 'Lorentzian dominated lineshapes and linewidths for Raman symmetric stretch peaks (800-1200 cm^{-1}) in Q^n (n = 1-3) species of alkali silicate glasses/melts.' *Journal of Non-Crystalline Solids*, **484**, pp. 72–83.

[10] Barlet, M., J. Delaye, T. Charpentier, M. Gennisson, D. Bonamy, T. Rouxel & C. Rountree [2015]. 'Hardness and toughness of sodium borosilicate glasses via Vickers's indentations.' *Journal of Non-Crystalline Solids*, **417-418**, pp. 66–79.

[11] Bechgaard, T., A. Goel, R. Youngman, J. Mauro, S. Rzoska, M. Bockowski, L. Jensen & M. Smedskjaer [2016]. 'Structure and mechanical properties of compressed sodium aluminosilicate glasses: Role of non-bridging oxygens.' *Journal of Non-Crystalline Solids*, **441**, pp. 49–57.

[12] Bell, D. & G. Rossman [1992]. 'Water in Earth's Mantle: The Role of Nominally Anhydrous Minerals.' *Science*, **255**, pp. 1391–1397.

[13] Bellot-Gurlet, L., F.-X. Le Bourdonnec, G. Poupeau & S. Dubernet [2004]. 'Raman micro-spectroscopy of western Mediterranean obsidian glass: one step towards provenance studies?' *Journal of Raman Spectroscopy*, **35**, pp. 671–677.

[14] Benzine, O., S. Bruns, Z. Pan, K. Durst & L. Wondraczek [2018]. 'Local Deformation of Glasses is Mediated by Rigidity Fluctuation on Nanometer Scale.' *Advanced Science*, **5**, pp. 1800916.

[15] Bottinga, Y., P. Richet & A. Sipp [1995]. 'Viscosity regimes of homogeneous silicate melts.' *American Mineralogist*, **80**, pp. 305–318.

[16] Bradtmüller, H., L. Zhang, C. de Araujo, H. Eckert, D. Möncke & D. Ehrt [2018]. 'Structural Studies of $NaPO_3$ - AlF_3 Glasses by High-Resolution Double-Resonance Nuclear Magnetic Resonance Spectroscopy.' *Journal of Physical Chemistry C*, **122**, pp. 21579–21588.

[17] Brooker, M., O. Nielsen & E. Praestgaard [1988]. 'Assessment of correction procedures for reduction of Raman spectra.' *Journal of Raman Spectroscopy*, **19**, pp. 71–78.

[18] Brow, R., R. Kirkpatrick & G. Turner [1993]. 'Nature of Alumina in Phosphate Glass: II, Structure of Sodium Aluminophosphate Glass.' *Journal of the American Ceramic Society*, **76**(4), pp. 919–928.

[19] Brow, R., D. Tallant, J. Hudgens, S. Martin & A. Irwin [1994]. 'The short-range structure of sodium ultraphosphate glasses.' *Journal of Non-Crystalline Solids*, **177**, pp. 221–228.

[20] Brow, R., D. Tallant, S. Myers & C. Phifer [1995]. 'The short-range structure of zinc polyphosphate glass.' *Journal of Non-Crystalline Solids*, **191**, pp. 45–55.

[21] Calas, G., G. Brown Jr., G. Waychunas & J. Petiau [1987]. 'X-ray absorption spectroscopic studies of silicate glasses and minerals.' *Physics and Chemistry of Minerals*, **15**, pp. 19–29.

[22] Callister Jr., W. & D. Rethwisch [2010]. *Materials Science and Engineering - An Introduction*. John Wiley & Sons, 8th edition. ISBN 978-0-470-41997-7.

[23] Cann, J. & C. Renfrew [1964]. 'The Characterization of Obsidian and its application to the Mediterranean region.' *Proceedings of the Prehistoric Society*, **30**, pp. 111–133.

[24] Chakraborty, I. & R. Condrate [1985]. 'The vibrational spectra of glasses in the Na_2O-SiO_2-P_2O_5 system with a 1:1 SiO_2 : P_2O_5 molar ratio.' *Physics and Chemistry of Glasses*, **26**(3), pp. 68–73.

[25] Chukanov, N. & A. Chervonnyi [2016]. *Infrared Spectroscopy of Minerals and Related Compounds*. Springer. ISBN 978-3-319-25347-3.

[26] Cicconi, M., D. Neuville, W. Blanc, J.-F. Lupi, M. Vermillac & D. de Ligny [2017]. 'Cerium/aluminum correlation in aluminosilicate glasses and optical silica fiber preforms.' *Journal of Non-Crystalline Solids*, **475**, pp. 85–95.

[27] Cody, G., B. Mysen, G. Sághi-Szabó & J. Tossell [2001]. 'Silicate-phosphate interactions in silicate glasses and melts: I. A multinuclear (^{27}Al,^{29}Si,^{31}P) MAS NMR and ab initio chemical shielding (^{31}P) study of phosphorous speciation in silicate glasses.' *Geochimica et Cosmochimica Acta*, **65**(14), pp. 2395–2411.

[28] Cook, R. & G. Pharr [1990]. 'Direct Observation and Analysis of Indentation Cracking in Glasses and Ceramics.' *Journal of the American Ceramic Society*, **73**, pp. 787–817.

[29] Cornet, A., V. Martinez, D. de Ligny, B. Champagnon & C. Martinet [2017]. 'Relaxation of densified silica glass.' *The Journal of Chemical Physics*, **146**, pp. 094504.

[30] Corno, M., A. Pedone, R. Dovesi & P. Ugliengo [2008]. 'B3LYP simulation of the full vibrational spectrum of 45S5 bioactive silicate glass compared to ν-silica.' *Chemistry of Materials*, **20**(17), pp. 5610–5621.

[31] Daniel, I., P. Gillet, B. Poe & P. McMillan [1995]. 'In-situ High-Temperature Raman Spectroscopic Studies of Aluminosilicate Liquids.' *Physics and Chemistry of Minerals*, **22**, pp. 74–86.

[32] Day, D. & E. Rindone [1962]. 'Properties of soda aluminosilicate glasses: I, refractive index, density, molar refractivity, and infrared absorption spectra.' *Journal of the American Ceramic Society*, **45**(10), pp. 489–496.

[33] Deák, T. & T. Czigány [2009]. 'Chemical Composition and Mechanical Properties of Basalt and Glass Fibers: A Comparison.' *Textile Research Journal*, **79**(7), pp. 645–651.

[34] Demtröder, W. [2006]. *Atoms, Molecules and Photons - An Introduction to Atomic, Molecular and Quantum Physics*. Springer. ISBN 3-540-20631-0.

[35] Dennis, J. & R. Schnabel [1996]. *Numerical Methods for Unconstrained Optimization and Nonlinear Equations (Classics in Applied Mathematics)*. Society for Industrial and Applied Mathematics. ISBN 0-89871-364-1.

[36] Deschamps, T., C. Martinet, J. Bruneel & B. Champagnon [2011]. 'Soda-lime silicate glass under hydrostatic pressure and indentation: a micro-Raman study.' *Journal of Physics: Condensed Matter*, **23**(3), pp. 035402.

[37] DiGiovanni, D., J. MacChesney & T. Kometani [1989]. 'Structure and properties of silica containing aluminum and phosphorus near the $AlPO_4$ join.' *Journal of Non-Crystalline Solids*, **113**, pp. 58–64.

[38] Duffy, J. [1986]. 'The refractivity and optical basicity of glass.' *Journal of Non-Crystalline Solids*, **86**, pp. 149–160.

[39] Duffy, J. [1990]. *Bonding, Energy Levels & Bands in inorganic Solids.* Longman Scientific & Technical. ISBN 0-582-03495-7.

[40] Duffy, J. [1993]. 'A review of optical basicity and its applications to oxidic systems.' *Geochimica et Cosmochimica Acta*, **57**, pp. 3961–3970.

[41] Duffy, J. [2002]. 'The electronic polarisability of oxygen in glass and the effect of composition.' *Journal of Non-Crystalline Solids*, **297**, pp. 275–284.

[42] Duffy, J. [2003]. 'Optical basicity and refractivity of aluminosilicate glasses.' *Physics and Chemistry of Glasses*, **44**(6), pp. 388–392.

[43] Duffy, J. & M. Ingram [1971]. 'Establishment of an optical scale for Lewis basicity in inorganic oxyacids, molten salts, and glasses.' *Journal of the American Chemical Society*, **93**, pp. 6448–6454.

[44] Duffy, J. & M. Ingram [1973]. 'Nephelauxetic Effect and Pauling Electronegativity.' *Journal of the Chemical Society - Chemical Communications*, pp. 635–636.

[45] Duffy, J. & M. Ingram [1975]. 'Optical Basicity - IV: Influence of Electronegativity on the Lewis Basicity and Solvent Properties of Molten Oxyanion Salts and Glasses.' *Journal of Inorganic and Nuclear Chemistry*, **37**, pp. 1203–1206.

[46] Duffy, J. & M. Ingram [1976]. 'An interpretation of glass chemistry in terms of the optical basicity concept.' *Journal of Non-Crystalline Solids*, **21**, pp. 373–410.

[47] Dupree, R., D. Holland & M. Mortuza [1988]. 'The role of small amounts of P_2O_5 in the structure of alkali disilicate glasses.' *Physics and Chemistry of Glasses*, **29**(1), pp. 18–21.

[48] Dupree, R., D. Holland, M. Mortuza, J. Collins & M. Lockyer [1989]. 'Magic Angle Spinning NMR of Alkali Phospho-Alumino-Silicate Glasses.' *Journal of Non-Crystalline Solids*, **112**, pp. 111–119.

[49] Dutta, P., D. Shieh & M. Puri [1987]. 'Raman spectroscopic study of the synthesis of zeolite Y.' *Journal of Physical Chemistry*, **91**, pp. 2332–2336.

[50] Efthimiopoulos, I., D. Palles, S. Richter, U. Hoppe, D. Möncke, L. Wondraczek, S. Nolte & E. Kamitsos [2018]. 'Femtosecond laser-induced transformations in ultra-low expansion glass: Microstructure and local density variations by vibrational spectroscopy.' *Journal of Applied Physics*, **123**, pp. 233105.

[51] Ehrt, D. [2015]. 'Phosphate and fluoride phosphate optical glasses - properties, structure and applications.' *Physics and Chemistry of Glasses: European Journal of Glass Science and Technology Part B*, **56**(6), pp. 217–234.

[52] Ehrt, D., M. Leister & A. Matthai [2001]. 'Polyvalent elements iron, tin and titanium in silicate, phosphate and fluoride glasses and melts.' *Physics and Chemistry of Glasses*, **42**(3), pp. 231–239.

[53] Ericson, J., A. Makishima, J. MacKenzie & R. Berger [1975]. 'Chemical and Physical Properties of Obsidian: A Naturally Occurring Glass.' *Journal of Non-Crystalline Solids*, **17**, pp. 129–142.

[54] Farmer, V., editor [1974]. *The Infrared Spectra of Minerals*. Mineralogical Society of Great Britain & Ireland. ISBN 0903056054.

[55] Fredholm, Y., N. Karpukhina, R. Law & R. Hill [2010]. 'Strontium containing bioactive glasses: Glass structure and physical properties.' *Journal of Non-Crystalline Solids*, **356**, pp. 2546–2551.

[56] Galeener, F. [1979]. 'Band limits and the vibrational spectra of tetrahedral glasses.' *Physical Review B*, **19**(8), pp. 4292–4297.

[57] Galeener, F. [1982]. 'Planar Rings in Vitreous Silica.' *Journal of Non-Crystalline Solids*, **49**, pp. 53–62.

[58] Galeener, F., R. Barrio, E. Martinez & R. Elliott [1984]. 'Vibrational Decoupling of Rings in Amorphous Solids.' *Physical Review Letters*, **53**(25), pp. 2429–2432.

[59] Galeener, F., A. Leadbetter & M. Stringfellow [1983]. 'Comparison of the neutron, Raman, and infrared vibrational spectra of vitreous SiO_2, GeO_2, and BeF_2.' *Physical Review B*, **27**(2), pp. 1052–1078.

[60] Galeener, F. & J. Mikkelsen [1979]. 'The Raman spectra and structure of pure vitreous P_2O_5.' *Solid State Communications*, **30**, pp. 505–510.

[61] Galeener, F. & P. Sen [1978]. 'Theory for the first-order vibrational spectra of disordered solids.' *Physical Review B*, **17**(4), pp. 1928–1933.

[62] Gan, H. & P. Hess [1992]. 'Phosphate speciation in potassium aluminosilicate glasses.' *American Mineralogist*, **77**, pp. 495–506.

[63] Gebert, W. [1972]. 'Die Kristallstruktur von $Ba_{13}Al_{22}Si_{10}O_{66}$.' *Zeitschrift für Kristallographie*, **135**, pp. 437–452.

[64] Giordano, D. & D. Dingwell [2003]. 'Non-Arrhenian multicomponent melt viscosity: a model.' *Earth and Planetary Science Letters*, **208**, pp. 337–349.

[65] Glatz, P., M. Comte, L. Cormier, L. Montagne, B. Doumert & G. Moore [2018]. 'Different roles of phosphorus in the nucleation of lithium aluminosilicate glasses.' *Journal of Non-Crystalline Solids*, **493**, pp. 48–56.

[66] Griebenow, K., C. Bragatto, E. Kamitsos & L. Wondraczek [2018]. 'Mixed-modifier effect in alkaline earth metaphosphate glasses.' *Journal of Non-Crystalline Solids*, **481**, pp. 447–456.

[67] Griebenow, K., U. Hoppe, D. Möncke, E. Kamitsos & L. Wondraczek [2017]. 'Transition-metal incorporation and Co-Sr/Mn-Sr mixed-modifier effect in metaphosphate glasses.' *Journal of Non-Crystalline Solids*, **460**, pp. 136–145.

[68] Griffith, A. [1920]. 'The Phenomena of Rupture and Flow in Solids.' *Philosophical Transactions of the Royal Society of London A*, **A 221**, pp. 163–198.

[69] Hecht, E. [2016]. *Optics*. Pearson Education, fifth edition. ISBN 978-1-292-09693-3.

[70] Hehlen, B. [2010]. 'Inter-tetrahedra bond angle of permanently densified silicas extracted from their Raman spectra.' *Journal of Physics: Condensed Matter*, **22**(2), pp. 025401.

[71] Hehlen, B. & D. Neuville [2015]. 'Raman response of network modifier cations in alumino-silicate glasses.' *Journal of Physical Chemistry B*, **119**(10), pp. 4093–4098.

[72] Hermansen, C., X. Guo, R. Youngman, J. Mauro, M. Smedskjaer & Y. Yue [2015]. 'Structure-topology-property correlations of

sodium phosphosilicate glasses.' *Journal of Chemical Physics*, **143**(6), pp. 64510.

[73] Hermansen, C., J. Matsuoka, S. Yoshida, H. Yamazaki, Y. Kato & Y. Yue [2013]. 'Densification and plastic deformation under microindentation in silicate glasses and the relation to hardness and crack resistance.' *Journal of Non-Crystalline Solids*, **364**, pp. 40–43.

[74] Hochella, M. & G. Brown Jr. [1985]. 'The structures of albite and jadeite composition glasses quenched from high pressure.' *Geochimica et Cosmochimica Acta*, **49**, pp. 1137–1142.

[75] Ingram, M., J. Davidson, A. Coats, E. Kamitsos & J. Kapoutsis [2000]. 'Origins of anomalous mixed-alkali effects in ion-exchanged glasses.' *Glastechnische Berichte - Glass Science and Technology*, **73**(4), pp. 89–104.

[76] Iwamoto, N., Y. Tsunawaki, T. Hattori & A. Mitsuishi [1978]. 'Raman spectra of Na_2O-SiO_2-Al_2O_3 and K_2O-SiO_2-AI_2O_3 glasses.' *Physics and Chemistry of Glasses*, **19**(6), pp. 141–143.

[77] Kailer, A., K. Nickel & Y. Gogotsi [1999]. 'Raman microspectroscopy of nanocrystalline and amorphous phases in hardness indentations.' *Journal of Raman Spectroscopy*, **30**(10), pp. 939–946.

[78] Kamitsos, E. [1989]. 'Modifying role of alkali-metal cations in borate glass networks.' *Journal of Physical Chemistry*, **93**, pp. 1604–1611.

[79] Kamitsos, E. [1996]. 'Reply to "Comment on 'Infrared-reflectance spectra of heat-treated, sol-gel-derived silica' ".' *Physical Review B*, **53**(21), pp. 14659–14662.

[80] Kamitsos, E. & G. Chryssikos [1998]. 'Alkali sites in glass.' *Solid State Ionics*, **105**, pp. 75–85.

[81] Kamitsos, E., G. Chryssikos & M. Karakassides [1988]. 'Glass transition phenomena and cation vibrations in alkali borate glasses.' *Physics and Chemistry of glasses*, **29**(3), pp. 121–126.

[82] Kamitsos, E., G. Chryssikos, A. Patsis & J. Duffy [1996]. 'Metal ion sites in oxide glasses - relation to glass basicity and ion transport.' *Journal of Non-Crystalline Solids*, **196**, pp. 249–254.

[83] Kamitsos, E., J. Kapoutsis, H. Jain & C. Hsieh [1994]. 'Vibrational study of the role of trivalent ions in sodium trisilicate glass.' *Journal of Non-Crystalline Solids*, **171**, pp. 31–45.

[84] Kamitsos, E., A. Patsis & G. Chryssikos [1993]. 'Infrared reflectance investigation of alkali diborate glasses.' *Journal of Non-Crystalline Solids*, **152**, pp. 246–257.

[85] Kamitsos, E., A. Patsis, M. Karakassides & G. Chryssikos [1990]. 'Infrared reflectance spectra of lithium borate glasses.' *Journal of Non-Crystalline Solids*, **126**, pp. 52–67.

[86] Kamitsos, E., A. Patsis & G. Kordas [1993]. 'Infrared-reflectance spectra of heat-treated, sol-gel-derived silica.' *Physical Review B*, **48**(17), pp. 12499–12505.

[87] Kamitsos, E. & W. Risen Jr. [1984]. 'Vibrational spectra of single and mixed alkali pentasilicate glasses.' *Journal of Non-Crystalline Solids*, **65**, pp. 333–354.

[88] Kamitsos, E., Y. Yiannopoulos & J. Duffy [2002]. 'Optical Basicity and Refractivity of Germanate Glasses.' *Journal of Physical Chemistry B*, **106**, pp. 8988–8993.

[89] Kapoor, S., X. Guo, R. Youngman, C. Hogue, J. Mauro, S. Rzoska, M. Bockowski, L. Jensen & M. Smedskjaer [2017]. 'Network Glasses Under Pressure: Permanent Densification in Modifier-Free Al_2O_3 - B_2O_3 - P_2O_5 - SiO_2 Systems.' *Physical Review Applied*, **7**, pp. 054011.

[90] Kassir-Bodon, A., T. Deschamps, C. Martinet, B. Champagnon, J. Teisseire & G. Kermouche [2012]. 'Raman Mapping of the Indentation-Induced Densification of a Soda-Lime-Silicate Glass.' *International Journal of Applied Glass Science*, **3**(1), pp. 29–35.

[91] Kato, Y., H. Yamazaki, S. Yoshida & J. Matsuoka [2010]. 'Effect of densification on crack initiation under Vickers indentation test.' *Journal of Non-Crystalline Solids*, **356**, pp. 1768–1773.

[92] Kermouche, G., E. Barthel, D. Vandembroucq & P. Dubujet [2008]. 'Mechanical modelling of indentation-induced densification in amorphous silica.' *Acta Materialia*, **56**, pp. 3222–3228.

[93] Kiefer, P., R. Balzer, J. Deubener, H. Behrens, T. Waurischk, S. Reinsch & R. Müller [2019]. 'Density, elastic constants and indentation hardness of hydrous soda-lime-silica glasses.' *Journal of Non-Crystalline Solids*, **521**, pp. 119480.

[94] Kim, C., M. Bell & D. McKeown [1995]. 'Vibrational analysis of beryl ($Be_3Al_2Si_6O_{18}$) and its constituent ring (Si_6O_{18}).' *Physica B*, **205**, pp. 193–208.

[95] Kirk, C. [1988]. 'Quantitative analysis of the effect of disorder-induced mode coupling on infrared absorption in silica.' *Physical Review B*, **38**(2), pp. 1255–1273.

[96] Kirkpatrick, R. & R. Brow [1995]. 'Nuclear magnetic resonance investigation of the structures of phosphate and phosphate-containing glasses: a review.' *Solid State Nuclear Magnetic Resonance*, **5**, pp. 9–21.

[97] Kittel, C. [2005]. *Introduction to Solid State Physics*. John Wiley & Sons, 8th edition. ISBN 0-471-41526-X.

[98] Kneubühl, F. [1989]. 'Review on the theory of the dielectric dispersion of insulators.' *Infrared Physics*, **29**(6), pp. 925–942.

[99] Knipping, J., L. Bilenker, A. Simon, M. Reich, F. Barra, A. Deditius, M. Wälle, C. Heinrich, F. Holtz & R. Munizaga [2015]. 'Trace elements in magnetite from massive iron oxide-apatite deposits indicate a combined formation by igneous and magmatic-hydrothermal processes.' *Geochimica et Cosmochimica Acta*, **171**, pp. 15–38.

[100] Konidakis, I., C.-P. Varsamis, E. Kamitsos, D. Möncke & D. Ehrt [2010]. 'Structure and properties of mixed strontium-manganese metaphosphate glasses.' *Journal of Physical Chemistry C*, **114**, pp. 9125–9138.

[101] Kono, Y. & C. Sanloup, editors [2018]. *Magmas Under Pressure: Advances in High-Pressure Experiments on Structure and Properties of Melts*. Elsevier. ISBN 978-0-12-811301-1.

[102] Kosinski, S., D. Krol, T. Duncan, D. Douglass, J. MacChesney & J. Simpson [1988]. 'Raman and NMR spectroscopy of SiO_2 glasses co-doped with Al_2O_3 and P_2O_5.' *Journal of Non-Crystalline Solids*, **105**, pp. 45–52.

[103] Kotz, F., K. Arnold, W. Bauer, D. Schild, N. Keller, K. Sachsenheimer, T. Nargang, C. Richter, D. Helmer & B. Rapp [2017]. 'Three-dimensional printing of transparent fused silica glass.' *Nature*, **544**, pp. 337–342.

[104] Kubicki, J. & M. Toplis [2002]. 'Molecular orbital calculations on aluminosilicate tricluster molecules: Implications for the structure of aluminosilicate glasses.' *American Mineralogist*, **87**, pp. 668–678.

[105] Lacy, E. [1963]. 'Aluminium in glasses and in melts.' *Physics and Chemistry of Glasses*, **4**(6), pp. 234–238.

[106] Lafuente, B., R. Downs, H. Yang & N. Stone [2015]. *The power of databases: the RRUFF project. In: Highlights in Mineralogical Crystallography*, chapter 1, pp. 1–30. W. De Gruyter. ISBN 978-3-11-041704-3.

[107] Lamberson, L. [2016]. *Influence of Atomic Structure on Plastic Deformation in Tectosilicate Calcium-Aluminosilicate, Magnesium-Aluminosilicate and Calcium-Galliosilicate Glasses*. Ph.D. thesis, Cornell University.

[108] Lambropoulos, J., S. Xu & T. Fang [1996]. 'Constitutive Law for the Densification of Fused Silica, with Applications in Polishing and Microgrinding.' *Journal of the American Ceramic Society*, **79**(6), pp. 1441–1452.

[109] Le Losq, C. & D. Neuville [2013]. 'Effect of the Na/K mixing on the structure and the rheology of tectosilicate silica-rich melts.' *Chemical Geology*, **346**, pp. 57–71.

[110] Le Losq, C., D. Neuville, W. Chen, P. Florian, D. Massiot, Z. Zhou & G. Greaves [2017]. 'Percolation channels: a universal idea to describe the atomic structure and dynamics of glasses and melts.' *Scientific Reports*, **7**, pp. 16490.

[111] Le Losq, C., D. Neuville, R. Moretti & J. Roux [2012]. 'Determination of water content in silicate glasses using Raman spectrometry: implications for the study of explosive volcanism.' *American Mineralogist*, **97**, pp. 779–790.

[112] Li, D., M. Fleet, G. Bancroft, M. Kasrai & Y. Pan [1995]. 'Local structure of Si and P in SiO_2 - P_2O_5 and Na_2O - SiO_2 - P_2O_5 glasses: a XANES study.' *Journal of Non-Crystalline Solids*, **188**, pp. 181–189.

[113] Limbach, R., B. Rodrigues, D. Möncke & L. Wondraczek [2015]. 'Elasticity, deformation and fracture of mixed fluoride-phosphate glasses.' *Journal of Non-Crystalline Solids*, **430**, pp. 99–107.

[114] Limbach, R., B. Rodrigues & L. Wondraczek [2014]. 'Strain-rate sensitivity of glasses.' *Journal of Non-Crystalline Solids*, **404**, pp. 124–134.

[115] Limbach, R., A. Winterstein-Beckmann, J. Dellith, D. Möncke & L. Wondraczek [2015]. 'Plasticity, crack initiation and defect resistance in alkali-borosilicate glasses: From normal to anomalous behavior.' *Journal of Non-Crystalline Solids*, **417-418**, pp. 15–27.

[116] Lönnroth, N. & Y. Yue [2009]. 'Influence of chemical composition on the physical properties of basaltic glasses.' *Glass Technology: European Journal of Glass Science and Technology Part A*, **50**(3), pp. 165–173.

[117] Lockyer, M., D. Holland & R. Dupree [1995]. 'The structure of (5x) P_2O_5 - (1-x) K_2O - 4(1-x) SiO_2 glasses.' *Physics and Chemistry of Glasses*, **36**(1), pp. 22–30.

[118] Loewenstein, W. [1954]. 'The distribution of aluminum in the tetrahedra of silicates and aluminates.' *American Mineralogist*, **39**, pp. 92–96.

[119] London, D., G. Morgan VI, H. Babb & J. Loomis [1993]. 'Behavior and effects of phosphorus in the system Na_2O - K_2O - Al_2O_3 - SiO_2 - P_2O_5 - H_2O at 200 MPa (H_2O).' *Contributions to Mineralogy and Petrology*, **113**, pp. 450–465.

[120] Long, D. [1977]. *Raman Spectroscopy*. McGraw-Hill. ISBN 0-07-038675-7.

[121] Long, D. [2002]. *The Raman Effect*. John Wiley & Sons. ISBN 0-471-49028-8.

[122] Lucas, B. & W. Oliver [1999]. 'Indentation power-law creep of high-purity indium.' *Metallurgical and Materials Transactions A: Physical Metallurgy and Materials Science*, **30A**, pp. 601–610.

[123] Luo, J., N. Smith, C. Pantano & S. Kim [2018]. 'Complex refractive index of silica, silicate, borosilicate, and boroaluminosilicate glasses

- Analysis of glass network vibration modes with specular-reflection IR spectroscopy.' *Journal of Non-Crystalline Solids*, **494**, pp. 94–103.

[124] MacKenzie, K. [1972]. 'Infrared Frequency Calculations for Ideal Mullite (3 Al_2O_3 - 2 SiO_2).' *Journal of the American Ceramic Society*, **55**(2), pp. 68–71.

[125] MacKenzie, K. & M. Smith [2002]. *Multinuclear Solid-State NMR of Inorganic Materials*. Pergamon. ISBN 978-0-08-043787-3.

[126] Maier, V., K. Durst, J. Mueller, B. Backes, H. Höppel & M. Göken [2011]. 'Nanoindentation strain-rate jump tests for determining the local strain-rate sensitivity in nanocrystalline Ni and ultrafine-grained Al.' *Journal of Materials Research*, **26**(11), pp. 1421–1430.

[127] Maier, V., B. Merle, M. Göken & K. Durst [2013]. 'An improved long-term nanoindentation creep testing approach for studying the local deformation processes in nanocrystalline metals at room and elevated temperatures.' *Journal of Materials Research*, **28**(9), pp. 1177–1177.

[128] Makishima, A. & J. MacKenzie [1973]. 'Direct calculation of Young's Modulus of Glass.' *Journal of Non-Crystalline Solids*, **12**, pp. 35–45.

[129] Malinovsky, V. & A. Sokolov [1986]. 'The Nature of Boson Peak in Raman Scattering in Glasses.' *Solid State Communications*, **57**(9), pp. 757–761.

[130] Martin, R. & F. Galeener [1981]. 'Correlated excitations and Raman scattering in glasses.' *Physical Review B*, **23**(6), pp. 3071–3081.

[131] Mazurin, O. [2007]. 'Problems of Compatibility of the Values of Glass Transition Temperatures Published in the World Literature.' *Glass Physics and Chemistry*, **33**(1), pp. 22–36.

[132] McKeown, D., M. Bell & C. Kim [1993]. 'Raman spectroscopy of silicate rings: Benitoite and the three-membered ring.' *Physical Review B*, **48**(22), pp. 16357–16365.

[133] McKeown, D., G. Waychunas & G. Brown [1985]. 'EXAFS study of the coordination environment of aluminum in a series of silica-rich glasses and selected minerals within the Na_2O - Al_2O_3 - SiO_2 system.' *Journal of Non-Crystalline Solids*, **74**, pp. 349–371.

[134] McMillan, P. & B. Piriou [1982]. 'The structures and vibrational spectra of crystals and glasses in the silica-alumina system.' *Journal of Non-Crystalline Solids*, **53**, pp. 279–298.

[135] McMillan, P., B. Piriou & A. Navrotsky [1982]. 'A Raman spectroscopic study of glasses along the joins silica-calcium aluminate, silica-sodium aluminate, and silica-potassium aluminate.' *Geochimica et Cosmochimica Acta*, **46**, pp. 2021–2037.

[136] McMillan, P., B. Poe, P. Gillet & B. Reynard [1994]. 'A study of SiO_2 glass and supercooled liquid to 1950 K via high-temperature Raman spectroscopy.' *Geochimica et Cosmochimica Acta*, **58**(17), pp. 3653–3664.

[137] Medenbach, O., W. Maresch, P. Mirwald & W. Schreyer [1980]. 'Variation of refractive index of synthetic Mg-cordierite with H_2O content.' *American Mineralogist*, **65**, pp. 367–373.

[138] Mercier, M., A. Di Muro, D. Giordano, N. Métrich, P. Lesne, M. Pichavant, B. Scaillet, R. Clocchiatti & G. Montagnac [2009]. 'Influence of glass polymerisation and oxidation on micro-Raman water analysis in alumino-silicate glasses.' *Geochimica et Cosmochimica Acta*, **73**(1), pp. 197–217.

[139] Merzbacher, C. & W. White [1988]. 'Structure of Na in aluminosilicate glasses: A far-infrared reflectance spectroscopic study.' *American Mineralogist*, **73**, pp. 1089–1094.

[140] Merzbacher, C. & W. White [1991]. 'The structure of alkaline earth aluminosilicate glasses as determined by vibrational spectroscopy.' *Journal of Non-Crystalline Solids*, **130**, pp. 18–34.

[141] Milkey, R. [1960]. 'Infrared spectra of some tectosilicate glasses.' *American Mineralogist*, **45**, pp. 990–1007.

[142] Miller, F. [1983]. 'The History of Spectroscopy as Illustrated on Stamps.' *Applied Spectroscopy*, **37**(3), pp. 219–225.

[143] Möncke, D., E. Kamitsos, D. Palles, R. Limbach, A. Winterstein-Beckmann, T. Honma, Z. Yao, T. Rouxel & L. Wondraczek [2016]. 'Transition and post-transition metal ions in borate glasses: Borate ligand speciation, cluster formation, and their effect on glass transition and mechanical properties.' *Journal of Chemical Physics*, **145**, pp. 124501.

[144] Mysen, B. [1998]. 'Phosphorus solubility mechanisms in haplogranitic aluminosilicate glass and melt: Effect of temperature and aluminum content.' *Contributions to Mineralogy and Petrology*, **133**(1), pp. 38–50.

[145] Mysen, B. [1999]. 'Structure and properties of magmatic liquids: From haplobasalt to haploandesite.' *Geochimica et Cosmochimica Acta*, **63**(1), pp. 95–112.

[146] Mysen, B. & G. Cody [2001]. 'Silicate-phosphate interactions in silicate glasses and melts: II. Quantitative, high-temperature structure of P-bearing alkali aluminosilicate melts.' *Geochimica et Cosmochimica Acta*, **65**(14), pp. 2413–2431.

[147] Mysen, B., L. Finger, D. Virgo & F. Seifert [1982]. 'Curve-fitting of Raman spectra of silicate glasses.' *American Mineralogist*, **67**(7-8), pp. 686–695.

[148] Mysen, B., F. Holtz, M. Pichavant, J.-M. Beny & J.-M. Montel [1997]. 'Solution mechanisms of phosphorus in quenched hydrous and anhydrous granitic glass as a function of peraluminosity.' *Geochimica et Cosmochimica Acta*, **61**(18), pp. 3913–3926.

[149] Mysen, B. & P. Richet [2005]. *Developments in Geochemistry Volume 10 - Silicate Glasses and Melts*. Elsevier, first edition. ISBN 978-0-444-52011-1.

[150] Mysen, B., F. Ryerson & D. Virgo [1981]. 'The structural role of phosphorus in silicate melts.' *American mineralogist*, **66**, pp. 106–117.

[151] Mysen, B. & M. Toplis [2007]. 'Structural behavior of Al^{3+} in peralkaline, metaluminous, and peraluminous silicate melts and glasses at ambient pressure.' *American Mineralogist*, **92**, pp. 933–946.

[152] Mysen, B., D. Virgo & F. Seifert [1982]. 'The structure of silicate melts implications for chemical and physical properties of natural magma.' *Reviews of Geophysics and Space Physics*, **20**(3), pp. 353–383.

[153] Navrotsky, A., K. Geisinger, P. McMillan & G. Gibbs [1985]. 'The tetrahedral framework in glasses and melts - inferences from molecular orbital calculations and implications for structure, thermodynamics, and physical properties.' *Physics and Chemistry of Minerals*, **11**, pp. 284–298.

[154] Neuville, D., L. Cormier, D. Caurant & L. Montagne, editors [2016]. *From Glass to Crystal - Nucleation, growth and phase separation, from research to applications*. EDP Sciences. ISBN 978-2-7598-1783-2.

[155] Neuville, D., L. Cormier & D. Massiot [2004]. 'Al environment in tectosilicate and peraluminous glasses: A ^{27}Al MQ-MAS NMR, Raman, and XANES investigation.' *Geochimica et Cosmochimica Acta*, **68**(24), pp. 5071–5079.

[156] Neuville, D., L. Cormier & D. Massiot [2006]. 'Al coordination and speciation in calcium aluminosilicate glasses: Effects of composition determined by ^{27}Al MQ-MAS NMR and Raman spectroscopy.' *Chemical Geology*, **229**, pp. 173–185.

[157] Neuville, D., L. Cormier, V. Montouillout, P. Florian, F. Millot, J. Rifflet & D. Massiot [2008]. 'Structure of Mg- and Mg/Ca aluminosilicate glasses: ^{27}Al NMR and Raman spectroscopy investigations.' *American Mineralogist*, **93**(11-12), pp. 1721–1731.

[158] Neuville, D., L. Cormier, V. Montouillout & D. Massiot [2007]. 'Local Al site distribution in aluminosilicate glasses by ^{27}Al MQMAS NMR.' *Journal of Non-Crystalline Solids*, **353**, pp. 180–184.

[159] Neuville, D., D. de Ligny & G. Henderson [2014]. 'Advances in Raman Spectroscopy Applied to Earth and Material Sciences.' *Reviews in Mineralogy and Geochemistry*, **78**, pp. 509–541.

[160] Neuville, D. & B. Mysen [1996]. 'Role of aluminium in the silicate network: In situ, high-temperature study of glasses and melts on the join SiO_2-$NaAlO_2$.' *Geochimica et Cosmochimica Acta*, **60**(10), pp. 1727–1737.

[161] Nizamutdinova, A. [2019]. *Modern Solid State NMR on Amorphous Materials: High-Coordinated Glasses and Polyacrylnitrile*. Ph.D. thesis, Universität Augsburg. (In preparation).

[162] Nizamutdinova, A., H. Kirchhain, L. van Wüllen, N. Sawangboon & D. Brauer [2018]. 'The structural role of alumina in alkali phosphosilicate glasses: a multinuclear solid state NMR study.' *Physics and Chemistry of Glasses: European Journal of Glass Science and Technology Part B*, **59**(6), pp. 267–276.

[163] Novikov, A., D. Neuville, L. Hennet, Y. Gueguen, D. Thiaudiere, T. Charpentier & P. Florian [2017]. 'Al and Sr environment in tectosilicate glasses and melts: Viscosity, Raman and NMR investigation.' *Chemical Geology*, **461**, pp. 115–127.

[164] Nowak, M. & H. Behrens [2001]. 'Water in rhyolitic magmas: getting a grip on a slippery problem.' *Earth and Planetary Science Letters*, **184**, pp. 515–522.

[165] Oliver, W. & G. Pharr [1992]. 'An improved technique for determining hardness and elastic modulus using load and displacement sensing indentation experiments.' *Journal of Materials Research*, **7**(6), pp. 1564–1583.

[166] Oliver, W. & G. Pharr [2004]. 'Measurement of hardness and elastic modulus by instrumented indentation: Advances in understanding and refinements to methodology.' *Journal of Materials Research*, **19**(01), pp. 3–20.

[167] Palles, D., I. Konidakis, C. Varsamis & E. Kamitsos [2016]. 'Vibrational spectroscopic and bond valence study of structure and bonding in Al_2O_3-containing AgI - $AgPO_3$ glasses.' *RSC Advances*, **6**(20), pp. 16697–16710.

[168] Pasquarello, A., J. Sarnthein & R. Car [1998]. 'Dynamic structure factor of vitreous silica from first principles: Comparison to neutron-inelastic-scattering experiments.' *Physical Review B*, **57**(22), pp. 14133–14140.

[169] Pauling, L. [1927]. 'The sizes of ions and the structure of ionic crystals.' *Journal of the American Chemical Society*, **49**, pp. 765–790.

[170] Pichavant, M., J.-M. Montel & L. Richard [1992]. 'Apatite solubility in peraluminous liquids: Experimental data and an extension of the Harrrison-Watson model.' *Geochimica et Cosmochimica Acta*, **56**, pp. 3855–3861.

[171] Plotnichenko, V., V. Sokolov, V. Koltashev & E. Dianov [2002]. 'On the structure of phosphosilicate glasses.' *Journal of Non-Crystalline Solids*, **306**(3), pp. 209–226.

[172] Poe, B., C. Romano, N. Zotov, G. Cibin & A. Marcelli [2001]. 'Compression mechanisms in aluminosilicate melts: Raman and XANES spectroscopy of glasses quenched from pressures up to 10 GPa.' *Chemical Geology*, **174**, pp. 21–31.

[173] Rabia, M., S. Degioanni, C. Martinet, J. Le Brusq, B. Champagnon & D. Vouagner [2016]. 'A-thermal elastic behavior of silicate glasses.' *Journal of Physics: Condensed Matter*, **28**(7), pp. 075402.

[174] Rao, K. [2002]. *Structural Chemistry of Glasses*. Elsevier. ISBN 0080439586.

[175] Ray, C. & D. Day [1997]. 'An Analysis of Nucleation-Rate Type of Curves in Glass as Determined by Differential Thermal Analysis.' *Journal of the American Ceramic Society*, **80**(12), pp. 3100–3108.

[176] Ray, N. [1974]. 'Composition-property relationships in inorganic oxide glasses.' *Journal of Non-Crystalline Solids*, **15**, pp. 423–434.

[177] Ren, M., J. Cheng, S. Jaccani, S. Kapoor, R. Youngman, L. Huang, J. Du & A. Goel [2019]. 'Composition - structure - property relationships in alkali aluminosilicate glasses: A combined experimental - computational approach towards designing functional glasses.' *Journal of Non-Crystalline Solids*, **505**, pp. 144–153.

[178] Richet, P., R. Robie, J. Rogez, B. Hemingway, P. Courtial & C. Téqui [1990]. 'Thermodynamics of open networks: Ordering and entropy in $NaAlSiO_4$ glass, liquid, and polymorphs.' *Physics and Chemistry of Minerals*, **17**, pp. 385–394.

[179] Riebling, E. [1966]. 'Structure of Sodium Aluminosilicate Melts Containing at Least 50 mole % SiO_2 at 1500°C.' *The Journal of Chemical Physics*, **44**(8), pp. 2857–2865.

[180] Rouxel, T. [2006]. 'Elastic properties of glasses: a multiscale approach.' *Comptes Rendus - Mécanique*, **334**(12), pp. 743–753.

[181] Rouxel, T. [2007]. 'Elastic properties and short-to medium-range order in glasses.' *Journal of the American Ceramic Society*, **90**(10), pp. 3019–3039.

[182] Rouxel, T. [2015]. 'Driving Force for Indentation in Glass: Composition, Pressure and Temperature Dependence.' *Philosophical Transactions of the Royal Society A*, **373**, pp. 20140140.

[183] Rouxel, T., H. Ji, T. Hammouda & A. Moréac [2008]. 'Poisson's Ratio and the Densification of Glass under High Pressure.' *Physical Review Letters*, **100**, pp. 225501.

[184] Ryerson, F. & P. Hess [1980]. 'The role of P_2O_5 in silicate melts.' *Geochimica et Cosmochimica Acta*, **44**, pp. 611–624.

[185] Ryerson, P. & P. Hess [1978]. 'Implications of liquid-liquid distribution coefficients to mineral-liquid partitioning.' *Geochimica et Cosmochimica Acta*, **42**, pp. 921–932.

[186] Safford, H. & A. Silverman [1947]. 'Alumina-Silica Relationship in Glass.' *Journal of the American Ceramic Society*, **30**(7), pp. 203–211.

[187] Sanchez-Valle, C. & J. Bass [2010]. 'Elasticity and pressure-induced structural changes in vitreous $MgSiO_3$-enstatite to lower mantle pressures.' *Earth and Planetary Science Letters*, **295**, pp. 523–530.

[188] Sawangboon, N., A. Nizamutdinova, R. Limbach, E. Meechoowas, K. Tapasa, D. Möncke, L. Wondraczek, E. Kamitsos, L. van Wüllen & D. Brauer. 'Modification of silicophosphate glass composition, structure and properties via crucible material and melting conditions.' (In preparation).

[189] Schaller, T., C. Rong, M. Toplis & H. Cho [1999]. 'TRAPDOR NMR investigations of phosphorus-bearing aluminosilicate glasses.' *Journal of Non-Crystalline Solids*, **248**, pp. 19–27.

[190] Schmücker, M. & H. Schneider [1996]. 'A new approach on the coordination of Al in non-crystalline gels and glasses of the system Al_2O_3 - SiO_2.' *Berichte der Bunsengesellschaft für physikalische Chemie*, **100**(9), pp. 1550–1553.

[191] Schmücker, M. & H. Schneider [2002]. 'New evidence for tetrahedral triclusters in aluminosilicate glasses.' *Journal of Non-Crystalline Solids*, **311**, pp. 211–215.

[192] Scholze, H. [1991]. *Glass - Nature, Structure and Properties.* Springer. ISBN 978-1-4613-9071-8.

[193] Sehgal, J. & S. Ito [1998]. 'A New Low-Brittleness Glass in the Soda - Lime - Silica Glass Family.' *Journal of the American Ceramic Society*, **81**(9), pp. 2485–2488.

[194] Seifert, F., B. Mysen & D. Virgo [1982]. 'Three-dimensional network structure of quenched melts (glass) in the systems SiO_2 - $NaAlO_2$, SiO_2 - $CaAl_2O_4$ and SiO_2 - $MgAl_2O_4$.' *American Mineralogist*, **67**, pp. 696–717.

[195] Sellappan, P., T. Rouxel, F. Celarie, E. Becker, P. Houizot & R. Conradt [2013]. 'Composition dependence of indentation deformation and indentation cracking in glass.' *Acta Materialia*, **61**(16), pp. 5949–5965.

[196] Sen, P. & M. Thorpe [1977]. 'Phonons in AX_2 glasses: From molecular to band-like modes.' *Physical Review B*, **15**(8), pp. 4030–4038.

[197] Sengupta, P. [2012]. 'A review on immobilization of phosphate containing high level nuclear wastes within glass matrix - Present status and future challenges.' *Journal of Hazardous Materials*, **235**, pp. 17–28.

[198] Shannon, R. [1976]. 'Revised effective ionic radii and systematic studies of interatomic distances in halides and chalcogenides.' *Acta Crystallographica*, **A32**, pp. 751–767.

[199] Shannon, R. & C. Prewitt [1969]. 'Effective Ionic Radii in Oxides and Fluorides.' *Acta Crystallographica*, **B25**, pp. 925–946.

[200] Sharma, S., J. Mammone & M. Nicol [1981]. 'Raman investigation of ring configurations in vitreous silica.' *Nature*, **292**, pp. 140–141.

[201] Sharma, S., J. Philpotts & D. Matson [1985]. 'Ring distributions in alkali- and alkaline-earth aluminosilicate framework glasses - a Raman spectroscopic study.' *Journal of Non-Crystalline Solids*, **71**, pp. 403–410.

[202] Shelby, J. [2005]. *Introduction to Glass Science and Technology*. The Royal Society of Chemistry. ISBN 0-85404-639-9.

[203] Shibata, N., M. Horigudhi & T. Edahiro [1981]. 'Raman spectra of binary high-silica glasses and fibers containing GeO_2, P_2O_5 and B_2O_3.' *Journal of Non-Crystalline Solids*, **45**, pp. 115–126.

[204] Shim, S.-H. & K. Catalli [2009]. 'Compositional dependence of structural transition pressures in amorphous phases with mantle-related compositions.' *Earth and Planetary Science Letters*, **283**, pp. 174–180.

[205] Shuker, R. & R. Gammon [1970]. 'Raman-Scattering Selection-Rule Breaking and the Density of States in Amorphous Materials.' *Physical Review Letters*, **25**(4), pp. 222–225.

[206] Smedskjaer, M., J. Mauro, J. Kjeldsen & Y. Yue [2013]. 'Microscopic Origins of Compositional Trends in Aluminosilicate Glass Properties.' *Journal of the American Ceramic Society*, **96**(5), pp. 1436–1443.

[207] Smith, E. & G. Dent [2005]. *Modern Raman Spectroscopy - A Practical Approach*. Wiley. ISBN 0-471-49794-0.

[208] Spitzer, W., R. Miller, D. Kleinman & L. Howarth [1962]. 'Far Infrared Dielectric Dispersion in $BaTiO_3$, $SrTiO_3$, and TiO_2.' *Physical Review*, **126**(5), pp. 1710–1721.

[209] Stavrou, E., D. Palles, E. Kamitsos, A. Lipovskii, D. Tagantsev, Y. Svirko & S. Honkanen [2014]. 'Vibrational study of thermally ion-exchanged sodium aluminoborosilicate glasses.' *Journal of Non-Crystalline Solids*, **401**, pp. 232–236.

[210] Stebbins, J., J. Oglesby & S. Kroeker [2001]. 'Oxygen triclusters in crystalline $CaAl_4O_7$ (grossite) and in calcium aluminosilicate glasses: ^{17}O NMR.' *American Mineralogist*, **86**, pp. 1307–1311.

[211] Stebbins, J. & Z. Xu [1997]. 'NMR evidence for excess non-bridging oxygen in an aluminosilicate glass.' *Nature*, **390**, pp. 1996–1998.

[212] Stoch, L. & M. Środa [1999]. 'Infrared spectroscopy in the investigation of oxide glasses structure.' *Journal of Molecular Structure*, **511**, pp. 77–84.

[213] Stolper, E. [1982]. 'Water in silicate glasses: An infrared spectroscopic study.' *Contributions to Mineralogy and Petrology*, **81**, pp. 1–17.

[214] Stubičan, V. & R. Roy [1961]. 'Isomorphous substitution and infrared spectra of the layer lattice silicates.' *American Mineralogist*, **46**, pp. 32–51.

[215] Svenson, M., L. Thirion, R. Youngman, J. Mauro, M. Bauchy, S. Rzoska, M. Bockowski & M. Smedskjaer [2016]. 'Effects of Thermal and Pressure Histories on the Chemical Strengthening of Sodium Aluminosilicate Glass.' *Frontiers in Materials*, **3**, pp. 1–11.

[216] Tagiara, N., D. Palles, E. Simandiras, V. Psycharis, A. Kyritsis & E. Kamitsos [2017]. 'Synthesis, thermal and structural properties of pure TeO_2 glass and zinc-tellurite glasses.' *Journal of Non-Crystalline Solids*, **457**, pp. 116–125.

[217] Takada, A., J. Parker, A. Durán & K. Bange, editors [2018]. *Teaching Glass Better*. International Commission on Glass. ISBN 978-84-17528-04-1.

[218] Tang, Y., H. Zhang & B. Rao [2016]. 'The effect of phosphorus on manganocolumbite and manganotantalite solubility in peralkaline to peraluminous granitic melts the effect of P on Nb and Ta solubility.' *American Mineralogist*, **101**, pp. 415–422.

[219] Tarragó, M., H. Esteves, M. Garcia-Valles, S. Martínez & D. Neuville [2018]. 'Effect of Ca in P-doped basaltic glass-ceramics: Application to waste inertization.' *Materials Letters*, **220**, pp. 266–268.

[220] Tarragó, M., M. Garcia-Valles, S. Martínez & D. Neuville [2018]. 'Phosphorus solubility in basaltic glass: Limitations for phosphorus immobilization in glass and glass-ceramics.' *Journal of Environmental Management*, **220**, pp. 54–64.

[221] Taylor, M. & G. Brown [1979]. 'Structure of mineral glasses - I. The feldspar glasses $NaAlSi_3O_8$, $KAlSi_3O_8$, $CaAl_2Si_2O_8$.' *Geochimica et Cosmochimica Acta*, **43**, pp. 61–75.

[222] Taylor, M. & G. Brown [1979]. 'Structure of mineral glasses-II. The SiO_2-$NaAlSiO_4$ join.' *Geochimica et Cosmochimica Acta*, **43**, pp. 1467–1473.

[223] Thompson, L. & J. Stebbins [2012]. 'Non-stoichiometric non-bridging oxygens and five-coordinated aluminum in alkaline earth aluminosilicate glasses: Effect of modifier cation size.' *Journal of Non-Crystalline Solids*, **358**, pp. 1783–1789.

[224] Thomsen, R., J. Skribsted & Y. Yue [2018]. 'The charge-balancing role of calcium and alkali ions in per-alkaline aluminosilicate glasses.' *The Journal of Physical Chemistry B*, **122**, pp. 3184–3195.

[225] Tiegel, M., R. Hosseinabadi, S. Kuhn, A. Herrmann & C. Rüssel [2015]. 'Young's modulus, Vickers hardness and indentation fracture toughness of alumino silicate glasses.' *Ceramics International*, **41**(6), pp. 7267–7275.

[226] Toplis, M. & D. Dingwell [1996]. 'The variable influence of P_2O_5 on the viscosity of melts of differing alkali/aluminium ratio: Implications for the structural role of phosphorus in silicate melts.' *Geochimica et Cosmochimica Acta*, **60**(21), pp. 4107–4121.

[227] Toplis, M., D. Dingwell & T. Lenci [1997]. 'Peraluminous viscosity maxima in Na_2O - Al_2O_3 - SiO_2 liquids: The role of triclusters in tectosilicate melts.' *Geochimica et Cosmochimica Acta*, **61**(13), pp. 2605–2612.

[228] Toplis, M. & T. Schaller [1998]. 'A MAS NMR study of glasses in the system $x\,Na_2O - (1\text{-}x)\,Al_2O_3 - 2\,SiO_2 - y\,P_2O_5$.' *Journal of Non-Crystalline Solids*, **224**(1), pp. 57–68.

[229] Tossel, J. & R. Cohen [2001]. 'Calculation of the electric field gradients at 'tricluster'-like O atoms in the polymorphs of Al_2SiO_5 and in aluminosilicate molecules: models for tricluster O atoms in glasses.' *Journal of Non-Crystalline Solids*, **286**, pp. 187–199.

[230] Varshneya, A. [1994]. *Fundamentals of Inorganic Glasses*. Academic Press. ISBN 0-12-714970-8.

[231] Veber, A., M. Cicconi, H. Reinfelder & D. de Ligny [2018]. 'Combined Differential scanning calorimetry, Raman and Brillouin spectroscopies: A multiscale approach for materials investigation.' *Analytica Chimica Acta*, **998**, pp. 37–44.

[232] Vegiri, A. & E. Kamitsos [2010]. 'Pressure-induced structural transformations in glass $0.3\,Li_2O$ - $0.7\,B_2O_3$: A molecular dynamics study.' *Physical Review B*, **82**, pp. 054114.

[233] Veksler, I., R. Thomas & R. Wirth [2003]. 'Crystallization of $AlPO_4$ - SiO_2 solid solutions from granitic melt and implications for P-rich melt inclusions in pegmatitic quartz.' *American Mineralogist*, **88**, pp. 1724–1730.

[234] Velli, L., C. Varsamis, E. Kamitsos, D. Möncke & D. Ehrt [2005]. 'Structural investigation of metaphosphate glasses.' *Physics and Chemistry of Glasses*, **46**(2), pp. 178–181.

[235] Velli, L., C. Varsamis, E. Kamitsos, D. Möncke & D. Ehrt [2008]. 'Optical basicity and refractivity in mixed oxyfluoride glasses.' *Physics and Chemistry of Glasses*, **49**(4), pp. 182–187.

[236] Wang, Y., A. Hamza & E. Ma [2006]. 'Temperature-dependent strain rate sensitivity and activation volume of nanocrystalline Ni.' *Acta Materialia*, **54**, pp. 2715–2726.

[237] Wang, Z., Y. Sun, S. Seetharaman, M. Zhang, M. Guo, Z. Li, Z. Guo & Z. Zhang [2016]. 'Viscous Flow and Crystallization Behaviors of P-bearing Steelmaking Slags with Varying Fluorine Content.' *ISIJ International*, **56**(4), pp. 546–553.

[238] Webster, J., R. Thomas, D. Rhede, H.-J. Förster & R. Seltmann [1997]. 'Melt inclusions in quartz from an evolved peraluminous pegmatite: Geochemical evidence for strong tin enrichment in fluorine-rich and phosphorus-rich residual liquids.' *Geochimica et Cosmochimica Acta*, **61**(13), pp. 2589–2604.

[239] Weigel, C., C. Le Losq, R. Vialla, C. Dupas, S. Clément, D. Neuville & B. Rufflé [2016]. 'Elastic moduli of $XAlSiO_4$ aluminosilicate glasses: effects of charge-balancing cations.' *Journal of Non-Crystalline Solids*, **447**, pp. 267–272.

[240] Whitfield, C., E. Brody & W. Bassett [1976]. 'Elastic moduli of NaCl by Brillouin scattering at high pressure in a diamond anvil cell.' *Review of Scientific Instruments*, **47**(8), pp. 942–947.

[241] Whittaker, E. & R. Muntus [1970]. 'Ionic radii for use in geochemistry.' *Geochimica et Cosmochimica Acta*, **34**, pp. 945–956.

[242] Winterstein-Beckmann, A., D. Möncke, D. Palles, E. Kamitsos & L. Wondraczek [2013]. 'Structure-property correlations in highly modified Sr, Mn-borate glasses.' *Journal of Non-Crystalline Solids*, **376**, pp. 165–174.

[243] Winterstein-Beckmann, A., D. Möncke, D. Palles, E. Kamitsos & L. Wondraczek [2014]. 'Raman spectroscopic study of structural changes induced by micro-indentation in low alkali borosilicate glasses.' *Journal of Non-Crystalline Solids*, **401**, pp. 110–114.

[244] Winterstein-Beckmann, A., D. Möncke, D. Palles, E. Kamitsos & L. Wondraczek [2015]. 'Structure and Properties of Orthoborate Glasses in the Eu_2O_3 - (Sr,Eu)O - B_2O_3 Quaternary.' *The Journal of Physical Chemistry B*, **119**, pp. 3259–3272.

[245] de Wispelaere, S., D. Cabaret, C. Levelut, S. Rossano, A.-M. Flank, P. Parent & F. Farges [2004]. 'Na-, Al-, and Si K-edge XANES study of sodium silicate and sodium aluminosilicate glasses: influence of the glass surface.' *Chemical Geology*, **213**, pp. 63–70.

[246] Wondraczek, L., J. Mauro, J. Eckert, U. Kühn, J. Horbach, J. Deubener & T. Rouxel [2011]. 'Towards ultrastrong glasses.' *Advanced Materials*, **23**(39), pp. 4578–4586.

[247] Wong, J. [1976]. 'Vibrational spectra of vapor-deposited binary phosphosilicate glasses.' *Journal of Non-Crystalline Solids*, **20**, pp. 83–100.

[248] Wray, J. & J. Neu [1969]. 'Refractive index of several glasses as a function of wavelength and temperature.' *Journal of the Optical Society of America*, **59**(6), pp. 774–776.

[249] van Wüllen, L., G. Tricot & S. Wegner [2007]. 'An advanced NMR protocol for the structural characterization of aluminophosphate glasses.' *Solid State Nuclear Magnetic Resonance*, **32**(2), pp. 44–52.

[250] Wyllie, P. & O. Tuttle [1964]. 'Experimental Investigation of Silicate Systems Containing Two Volatile Components - Part III. The Effects of SO_3, P_2O_5, HCl and Li_2O, in Addition to H_2O, on the Melting Temperatures of Albite and Granite.' *American Journal of Science*, **262**, pp. 930–939.

[251] Yadav, A. & P. Singh [2015]. 'A Review on Structure of Glasses by Raman Spectroscopy.' *RSC Advances*, **5**, pp. 67583–67609.

[252] Yamamoto, K. & H. Ishida [1994]. 'Optical theory applied to infrared spectroscopy.' *Vibrational Spectroscopy*, **8**, pp. 1–36.

[253] Yiannopoulos, Y., G. Chryssikos & E. Kamitsos [2001]. 'Structure and properties of alkaline earth borate glasses.' *Physics and Chemistry of Glasses*, **42**(3), pp. 164–172.

[254] Yoshida, S., J.-C. Sanglebœuf & T. Rouxel [2005]. 'Quantitative evaluation of indentation-induced densification in glass.' *Journal of Materials Research*, **20**(12), pp. 3404–3412.

[255] Zeidler, A., P. Salmon & B. Skinner [2014]. 'Packing and the structural transformations in liquid and amorphous oxides from ambient to extreme conditions.' *Proceedings of the National Academy of Sciences of the United States of America*, **111**(28), pp. 10045–10048.

[256] Zeng, H., L. Wang, F. Ye, B. Yang, J. Chen, G. Chen & L. Sun [2016]. 'Mechanical-Structural Investigation of Chemical Strengthening Aluminosilicate Glass through Introducing Phosphorus Pentoxide.' *Frontiers in Materials*, **3**, pp. 53.

[257] Zhao, Q., M. Guerette & L. Huang [2012]. 'Nanoindentation and Brillouin light scattering studies of elastic moduli of sodium silicate glasses.' *Journal of Non-Crystalline Solids*, **358**, pp. 652–657.

[258] Zorn, R. [2011]. 'The boson peak demystified?' *Physics*, **4**, pp. 44.

Appendix: Tabulated data

This appendix lists tabulated values for results that were presented in graphical form throughout this thesis.

Table A1: Data overview for the glass transition temperature, T_g, and the maximum position of the FIR band.

Glass	T_g (°C)	FIR max. (cm^{-1})
Si70P0	851 ± 5	158 ± 3
Si70P7.5	713 ± 5	204 ± 3
Si60P0	838 ± 5	166 ± 3
Si60P2.5	808 ± 5	169 ± 3
Si60P5	774 ± 5	173 ± 3
Si60P6.25	738 ± 5	174 ± 3
Si60P7.5	721 ± 5	182 ± 3
Si55.5P7.5	735 ± 5	176 ± 3
Si50P0	822 ± 5	182 ± 3
Si50P7.5	737 ± 5	174 ± 3

Table A2: Data overview for density, ρ, molar volume, V_m, packing density, C_g, and oxygen packing density, ρ_{ox}.

Glass	ρ (g/cm^3)	V_m (cm^3/mol)	C_g (-)	ρ_{ox} (g/cm^3)
Si70P0	2.41 ± 0.01	27.64 ± 0.11	0.481 ± 0.002	1.158 ± 0.005
Si70P7.5	2.33 ± 0.01	30.56 ± 0.13	0.474 ± 0.002	1.165 ± 0.005
Si60P0	2.47 ± 0.01	27.89 ± 0.11	0.487 ± 0.002	1.147 ± 0.005
Si60P2.5	2.44 ± 0.01	28.86 ± 0.12	0.484 ± 0.002	1.150 ± 0.005
Si60P5	2.42 ± 0.01	29.75 ± 0.12	0.483 ± 0.002	1.156 ± 0.005
Si60P6.25	2.40 ± 0.01	30.18 ± 0.13	0.482 ± 0.002	1.160 ± 0.005
Si60P7.5	2.39 ± 0.01	30.70 ± 0.13	0.481 ± 0.002	1.159 ± 0.005
Si55.5P7.5	2.42 ± 0.01	30.73 ± 0.13	0.484 ± 0.002	1.158 ± 0.005
Si50P0	2.50 ± 0.01	28.42 ± 0.11	0.487 ± 0.002	1.126 ± 0.005
Si50P7.5	2.45 ± 0.01	30.88 ± 0.13	0.487 ± 0.002	1.153 ± 0.005

Table A3: Data overview for the position in cm^{-1} (pos.) and relative area in % (area) of the deconvoluted high frequency Raman bands.

Glass		T_{2s}	$Q^{4,low}_{Si/Al}$	$Q^{4,high}_{Si/Al}$	$\nu_s(Q^2_P)$	$\nu_{as}(Q^2_P)$
Si70P0	pos.	983.4 ± 0.9	1085.0 ± 0.4	1165.0 ± 1.4	-	-
	area	26.7 ± 2.0	68.2 ± 4.6	5.0 ± 1.3	-	-
Si60P0	pos.	959.4 ± 1.1	1045.1 ± 0.9	1140.6 ± 2.1	-	-
	area	16.7 ± 3.2	79.7 ± 8.5	3.6 ± 1.3	-	-
Si60P2.5	pos.	960.4 ± 1.9	1050.7 ± 3.7	1146.7 ± 5.4	1058.0 ± 0.7	1201.6 ± 3.1
	area	6.8 ± 3.0	79.3 ± 13.6	8.7 ± 5.8	2.8 ± 1.5	2.4 ± 2.3
Si60P5	pos.	965.0 ± 1.4	1057.6 ± 0.9	1164.5 ± 5.8	1057.6 ± 0.4	1209.7 ± 1.1
	area	2.0 ± 0.4	78.1 ± 5.4	7.9 ± 1.3	8.8 ± 1.2	3.1 ± 0.9
Si60P6.25	pos.	969.3 ± 1.6	1062.4 ± 1.8	1166.0 ± 8.3	1062.4 ± 0.5	1213.2 ± 1.1
	area	1.9 ± 0.5	73.6 ± 8.7	10.3 ± 2.2	10.6 ± 2.1	3.6 ± 1.0
Si60P7.5	pos.	973.3 ± 1.9	1064.9 ± 3.3	1163.5 ± 12.4	1064.9 ± 0.5	1215.4 ± 1.5
	area	1.1 ± 0.4	70.8 ± 12.9	11.6 ± 4.1	12.0 ± 3.0	4.5 ± 1.6
Si50P0	pos.	932.6 ± 1.0	990.7 ± 0.8	1085.7 ± 3.0	-	-
	area	0.8 ± 0.1	84.1 ± 3.3	15.1 ± 1.6	-	-

Table A4: Data overview for the refractive index, n (without units), at the wavelengths 480, 546.1, 632.8 and 1300 nm.

Glass	n_{480}	$n_{546.1}$	$n_{632.8}$	n_{1300}
Si70P0	1.5007 ± 0.0005	1.4966 ± 0.0005	1.4944 ± 0.0001	1.4836 ± 0.0001
Si70P7.5	1.4824 ± 0.0010	1.4788 ± 0.0010	1.4773 ± 0.0020	1.4663 ± 0.0013
Si60P0	1.5109 ± 0.0005	1.5066 ± 0.0005	1.5036 ± 0.0001	1.4925 ± 0.0008
Si60P2.5	1.5048 ± 0.0005	1.5007 ± 0.0005	1.4967 ± 0.0005	1.4857 ± 0.0001
Si60P5	1.4985 ± 0.0003	1.4944 ± 0.0003	1.4913 ± 0.0001	1.4810 ± 0.0004
Si60P6.25	1.4954 ± 0.0005	1.4912 ± 0.0005	1.4884 ± 0.0002	1.4780 ± 0.0003
Si60P7.5	1.4924 ± 0.0005	1.4885 ± 0.0005	1.4864 ± 0.0007	1.4756 ± 0.0006
Si55.5P7.5	1.4966 ± 0.0005	1.4926 ± 0.0005	1.4898 ± 0.0002	1.4792 ± 0.0001
Si50P0	1.5212 ± 0.0005	1.5166 ± 0.0005	1.5130 ± 0.0001	1.5012 ± 0.0002
Si50P7.5	1.5018 ± 0.0003	1.4976 ± 0.0003	1.4953 ± 0.0008	1.4842 ± 0.0011

Table A5: Data overview for electronic polarisability, α_m, oxygen polarisability, $\alpha_{O^{2-}}$, theoretical optical basicity, Λ_{th}, and the centre of gravity (COG) of the high frequency envelope of IR and Raman spectra.

Glass	α_m (Å^3)	$\alpha_{O^{2-}}$ (Å^3)	Λ_{th} (-)	IR COG (cm^{-1})	Raman COG (cm^{-1})
Si70P0	3.192 ± 0.013	1.550 ± 0.007	0.56 ± 0.01	1042 ± 6	1063 ± 6
Si70P7.5	3.425 ± 0.016	1.504 ± 0.007	0.51 ± 0.01	1090 ± 6	1089 ± 6
Si60P0	3.272 ± 0.013	1.580 ± 0.007	0.58 ± 0.01	1022 ± 6	1032 ± 6
Si60P2.5	3.346 ± 0.014	1.561 ± 0.007	0.56 ± 0.01	1038 ± 6	1053 ± 6
Si60P5	3.417 ± 0.014	1.541 ± 0.007	0.55 ± 0.01	1049 ± 6	1063 ± 6
Si60P6.25	3.450 ± 0.014	1.531 ± 0.007	0.54 ± 0.01	1057 ± 6	1070 ± 6
Si60P7.5	3.497 ± 0.015	1.528 ± 0.007	0.53 ± 0.01	1063 ± 6	1075 ± 6
Si55.5P7.5	3.522 ± 0.015	1.535 ± 0.007	0.54 ± 0.01	1053 ± 6	1066 ± 6
Si50P0	3.385 ± 0.014	1.627 ± 0.007	0.61 ± 0.01	997 ± 6	1000 ± 6
Si50P7.5	3.572 ± 0.015	1.553 ± 0.007	0.55 ± 0.05	1041 ± 6	1053 ± 6

Table A6: Data overview for the elastic properties shear modulus, G, bulk modulus, K, Young's modulus, E, and Poisson's ratio, ν, measured by ultrasonic echometry (e), Brillouin spectroscopy (B) and nanoindentation (n).

Glass		G (GPa)	K (GPa)	E (GPa)	ν (-)
Si70P0	e	29.2 ± 0.4	40.2 ± 1.6	70.5 ± 1.1	0.208 ± 0.011
	B	29.5 ± 0.2	39.7 ± 0.4	71.0 ± 0.4	0.202 ± 0.002
	n	-	-	68.3 ± 0.1	-
Si70P7.5	e	26.8 ± 0.5	33.8 ± 1.8	63.7 ± 1.2	0.186 ± 0.015
	B	26.3 ± 0.2	34.0 ± 0.4	62.7 ± 0.4	0.193 ± 0.002
	n	-	-	60.3 ± 0.2	-
Si60P0	e	29.6 ± 0.3	42.1 ± 1.4	71.9 ± 0.9	0.216 ± 0.008
	B	29.3 ± 0.2	41.3 ± 0.4	71.0 ± 0.4	0.213 ± 0.002
	n	-	-	68.9 ± 0.3	-
Si60P2.5	e	28.7 ± 0.4	40.6 ± 1.5	69.7 ± 1.0	0.214 ± 0.010
	B	28.4 ± 0.2	40.6 ± 0.4	69.0 ± 0.4	0.216 ± 0.002
	n	-	-	66.2 ± 0.3	-
Si60P5	e	27.5 ± 0.5	38.4 ± 2.1	66.6 ± 1.3	0.211 ± 0.015
	B	28.4 ± 0.2	39.8 ± 0.3	68.9 ± 0.4	0.211 ± 0.002
	n	-	-	66.2 ± 0.7	-
Si60P6.25	e	26.6 ± 0.5	37.4 ± 2.0	64.6 ± 1.3	0.212 ± 0.015
	B	27.0 ± 0.2	37.4 ± 0.3	65.3 ± 0.4	0.209 ± 0.002
	n	-	-	61.7 ± 0.3	-
Si60P7.5	e	25.9 ± 0.6	37.2 ± 2.4	63.1 ± 1.5	0.217 ± 0.018
	B	26.2 ± 0.2	36.7 ± 0.3	63.5 ± 0.4	0.211 ± 0.002
	n	-	-	60.0 ± 0.2	-
Si55.5P7.5	e	26.9 ± 0.5	38.3 ± 2.0	65.3 ± 1.3	0.216 ± 0.014
	B	26.9 ± 0.2	37.9 ± 0.3	65.2 ± 0.4	0.213 ± 0.002
	n	-	-	62.9 ± 0.4	-
Si50P0	e	29.8 ± 0.5	45.8 ± 2.0	73.5 ± 1.2	0.233 ± 0.011
	B	30.6 ± 0.2	45.7 ± 0.4	75.1 ± 0.4	0.226 ± 0.002
	n	-	-	72.2 ± 0.2	-
Si50P7.5	e	26.8 ± 0.4	39.6 ± 1.5	65.5 ± 1.0	0.224 ± 0.010
	B	26.9 ± 0.2	39.4 ± 0.3	65.7 ± 0.4	0.222 ± 0.002
	n	-	-	62.5 ± 0.1	-

Table A7: Data overview for Vickers hardness, H_v, nanoindentation hardness, H, crack resistance, CR, strain rate sensitivity, m, and the densification-induced shift of the centre of gravity (COG) of the low frequency Raman region, determined after correction for either just a baseline or for combined baseline and data reduction by the Long equation.

Glass	H_v (GPa)	H (GPa)	CR (N)	m (-)	COG shift$_{base}$ (cm^{-1})	COG shift$_{base+Long}$ (cm^{-1})
Si70P0	5.88 ± 0.27	7.11 ± 0.03	5.2 ± 1.6	0.0131 ± 0.0008	18.9 ± 0.9	18.9 ± 0.9
Si70P7.5	5.07 ± 0.20	5.83 ± 0.05	4.6 ± 0.9	0.0160 ± 0.0003	20.0 ± 1.0	23.7 ± 1.4
Si60P0	6.17 ± 0.30	7.02 ± 0.04	4.4 ± 0.6	0.0147 ± 0.0009	13.5 ± 0.0	12.1 ± 0.9
Si60P2.5	5.90 ± 0.21	6.60 ± 0.06	8.1 ± 1.3	0.0150 ± 0.0008	17.6 ± 0.9	15.4 ± 1.1
Si60P5	5.26 ± 0.14	6.33 ± 0.07	4.7 ± 0.7	0.0154 ± 0.0007	16.5 ± 1.0	18.3 ± 0.7
Si60P6.25	5.25 ± 0.19	6.01 ± 0.04	7.5 ± 0.9	0.0162 ± 0.0009	18.4 ± 0.7	18.0 ± 1.1
Si60P7.5	5.14 ± 0.19	5.80 ± 0.02	5.3 ± 1.0	0.0172 ± 0.0012	16.8 ± 1.1	16.7 ± 1.1
Si55.5P7.5	5.26 ± 0.29	6.02 ± 0.06	5.7 ± 1.3	0.0180 ± 0.0018	16.2 ± 1.2	13.2 ± 0.5
Si50P0	6.30 ± 0.32	7.13 ± 0.03	3.1 ± 0.5	0.0123 ± 0.0009	14.6 ± 2.0	13.5 ± 1.2
Si50P7.5	5.24 ± 0.18	5.87 ± 0.03	9.3 ± 1.6	0.0165 ± 0.0010[a]	14.9 ± 2.8	13.7 ± 1.0

[a] During analysis of m for one sample (glass Si50P7.5), the buildup of a new hardness plateau after jumping to the strain rate 0.001 s^{-1} was slowed down for three of the ten investigated indentations. As the plateau was still reached, those indentations were not omitted from analysis, but their hardness for the strain rate 0.001 s^{-1} was only averaged over a penetration depth range of 60 to 90 nm instead of 100 nm.

Zusammenfassung

Ziel dieser Arbeit war die Untersuchung des Einflusses von Phosphat auf die mechanischen Eigenschaften von metalumischen Alumosilicatgläsern mit besonderem Fokus auf zugrunde liegende strukturelle Änderungen. Drei Glasreihen wurden synthetisiert um die Auswirkungen von steigendem P_2O_5-Gehalt zu untersuchen, sowie auch die Auswirkungen von variablem SiO_2-Gehalt in phosphathaltigen und phosphatfreien Gläsern. Eine Synthese metalumischer Phospho-Alumosilicatgläser war ohne signifikante Phosphatverluste möglich.
Alle Gläser wurden umfassend auf ihre mechanischen Eigenschaften hin charakterisiert, wobei für Härte und elastische Eigenschaften jeweils mehrere Methoden Anwendung fanden. Außerdem wurden Verdichtung, Risswiderstand und Dehnratenabhängigkeit untersucht. Neben den mechanischen Eigenschaften der Gläser wurden auch Glasübergangstemperatur und Kristallisation sowie Dichte und Brechungsindex bestimmt und zur weiteren strukturellen Interpretation herangezogen. Die Glasstruktur wurde durch Kombination von Infrarot-, Raman- (VV: parallel polarisiert und VH: kreuzpolarisiert) und Festkörper-NMR-Spektroskopie analysiert, letztere durchgeführt von Projektpartnern. Die Interpretation der Glasstruktur erfolgte nach den Prinzipien der Netzwerkpolymerisierung, der Packungsdichte und des ionischen Bindungsgrades.

- Die Kombination von Infrarot-, Raman- und NMR-Spektroskopie zeigte, dass Phosphat sowohl mit Natrium als auch mit Aluminium interagierte. Daraus ergaben sich ladungsausgeglichene Gruppen depolymerisierter Q^2_P-Einheiten (Metaphosphatgruppen) sowie vollständig polymerisierter Q^4_P-Einheiten (Al-O-P-Bindungen). Die Silicat- und Aluminatgruppen verblieben im Q^4-Zustand.
  Die komplementären Informationen zur Gruppensymmetrie aus Infrarot- und Ramanspektroskopie ermöglichten eine detaillierte Bandenzuordnung für die untersuchten Gläser. Dies ebnete auch den Weg für die weitere Verwendung der Spektren in der Analyse von Verdichtung und Ionizität. Durch die Untersuchung von VV- und VH-Ramanspektren zeigte sich, dass sich eine Phosphat-Ramanbande bei Änderung der Glaszusammensetzung weniger stark verschob als Alumosilicatbanden. Dies wurde einer verringerten Kopplung der Q^2_P-Gruppen mit dem Rest den Netzwerks zugeschrieben. Diese Phosphat-

bande verschob sich auch bei Variation des SiO_2-Gehaltes. Daraus ließ sich schließen, dass Phosphat ins Alumosilicatnetzwerk integriert war.

- Eine Erhöhung des Phosphatgehaltes durch Austausch von $NaAlO_2$ gegen P_2O_5 sollte gemäß Annahme das Molvolumen erhöhen und die Polymerisierung reduzieren. Die Erhöhung des Molvolumens wurde durch Messung der Dichte bestätigt, die reduzierte Polymerisierung durch Spektroskopie sowie durch eine starke Abnahme der Glasübergangstemperatur.
  Eine gleichzeitige Abnahme der Härte wurde teilweise der abnehmenden Polymerisierung zugeschrieben und teilweise dem zunehmenden Molvolumen. Auch Brechungsindex und elastische Moduln nahmen ab, was hauptsächlich mit der Abnahme der Dichte begründet werden konnte. Die Abnahme des Brechungsindex kann jedoch auch teilweise auf die Ausbildung von Al-O-P-Bindungen zurückzuführen sein. Schließlich wurde mit zunehmendem Phosphatgehalt eine Abnahme des ionischen Bindungscharakters festgestellt.
  Durch die starke Abnahme der Glasübergangstemperatur bei steigendem Phosphatgehalt ergibt sich eine einfachere Verarbeitbarkeit im Vergleich zu phosphatfreien Alumosilicatgläsern. Weiterhin wurde beobachtet, dass Phosphat die Kristallisation erschwert. Auch dies stellt einen Vorteil für die Verarbeitbarkeit dar und wurde der Integration von Phosphat ins Alumosilicatnetzwerk über Al-O-P-Bindungen zugeschrieben.

- Bei Variation des SiO_2-Gehaltes durch Austausch von $[AlO_4]^-$- gegen SiO_4-Tetraeder wurde angenommen, dass die Polymerisierung nahezu konstant bleibt. Dies wurde durch annähernd konstante Werte von Härte, Molvolumen sowie der elastischen Moduln E und G bestätigt. Auch vergleichsweise geringe Änderungen der Glasübergangstemperatur bei Variation des SiO_2-Gehaltes deuteten auf nur geringe Änderung der Polymerisierung hin.
  Eine leichte Abnahme der elastischen Eigenschaften, allen voran K, bei steigendem SiO_2-Gehalt konnte nicht über konstante Polymerisierung erklärt werden aber über die gleichzeitig abnehmende Packungsdichte. Auch eine Abnahme des Brechungsindex bei steigenden SiO_2-Gehalt konnte mit der abnehmenden Dichte begründet werden.
  Die Änderungen von T_g waren allerdings komplizierter. In phosphatfreien Gläsern nahm T_g mit zunehmendem SiO_2-Gehalt leicht zu, in phosphathaltigen Gläsern nahm T_g jedoch leicht ab.
  Der ionische Bindungsgrad nahm für steigenden SiO_2-Gehalt ab. Die stärker kovalenten Bindungen in Gläsern mit hohem SiO_2-Gehalt sind

eine mögliche Erklärung für die leichte T_g-Zunahme in phosphatfreien Gläsern.

- Die Abnahme von T_g in phosphathaltigen Gläsern bei steigendem SiO_2-Gehalt wurde als Konkurrenz zwischen Aluminat- und Phosphatgruppen um Ladungsausgleich durch Natrium interpretiert. Eine solche Konkurrenz kann potentiell zu leichten Änderungen der Polymerisierung führen und damit T_g beeinflussen. Diese Interpretation wurde durch eine Verschiebung der Natriumbande in Ferninfrarotspektren (FIR) unterstützt, die auf zunehmende Assoziation von Natrium mit Phosphat bei steigendem SiO_2-Gehalt hindeutete. Eine vergleichbare Verschiebung der FIR-Bande zeigte auch in der Glasreihe mit ansteigendem Phosphatgehalt eine zunehmende Assoziation von Natrium mit Phosphat an.
  Interessanterweise deutete die FIR-Bandenverschiebung in phosphatfreien Gläsern auf eine schwächere Bindung von Na bei steigendem SiO_2-Gehalt hin, obwohl hier keine Änderung der ladungsausgleichenden Rolle von Na gegenüber Al zu erwarten war. Dies wurde mit ionischen Wechselwirkungen zwischen benachbarten $Na^+[AlO_4]^-$-Tetraedern begründet. Solche Wechselwirkungen sollten mit abnehmender Anzahl an $Na^+[AlO_4]^-$-Tetraedern bei steigendem SiO_2-Gehalt schwächer werden. Diese Interpretation behält jedoch vorläufigen Charakter. Zu ihrer weiteren Untersuchung müssen noch metalumische Gläser mit einem Überschuss an $Na^+[AlO_4]^-$- über SiO_4-Tetraedern synthetisiert und auf ihre FIR-Bande hin untersucht werden.
  Die erfolgreiche Verknüpfung des anomalen T_g-Verlaufs mit der FIR-Natriumbande zeigte auf, dass eine detailliertere Untersuchung der Rolle der Alkalikationen neue Einblicke in die Glasstruktur gewähren kann. Hier bietet sich für die Zukunft noch eine Untersuchung der Na-O-Bindungslänge und der Na-Koordination an, ebenso wie eine genauere Untersuchung der Konkurrenz zwischen Phosphat- und Aluminatgruppen um Natrium.

- Der ionische Bindungsgrad wurde über die Berechnung von Sauerstoffpolarisierbarkeit und theoretischer optischer Basizität abgeschätzt. Sowohl mit zunehmendem P_2O_5-Gehalt als auch mit zunehmendem SiO_2-Gehalt nahm der ionische Bindungsgrad ab. Außerdem deckte sich die Beziehung zwischen Sauerstoffpolarisierbarkeit und optischer Basizität mit einem etablierten, empirischen Ausdruck für einfache Oxidgläser. Im Hinblick auf die Komplexität des untersuchten Systems mit drei Netzwerkbildnern ist dies bemerkenswert. Für die Berechnung

von Sauerstoffpolarisierbarkeit und theoretischer optischer Basizität war die Annahme nötig, dass die Glaszusammensetzung den nominellen Werten entspricht. Diese Berechnungen könnten in Zukunft durch experimentelle Bestimmung der optischen Basizität an Gläsern, die Ionen mit entsprechender Sondenfunktion enthalten, wie etwa Pb^{2+}, unterstützt werden.

- Interessanterweise ließ sich eine Korrelation zwischen theoretischer optischer Basizität und Verschiebungen der Hochfrequenzbanden von IR- und Ramanspektren feststellen. Die Bandenverschiebungen wurden über Änderungen der Glaszusammensetzung erklärt, wobei P-O-Bindungen die durchschnittliche Bindungsstärke der Gläser im Vergleich zu Si-O- und Al-O-Bindungen erhöhten.
  Diese durchschnittliche Bindungsstärke wird offenbar gut durch die theoretische optische Basizität wiedergegeben. Dies kann dadurch erklärt werden, dass die optische Basizität Änderungen von schwächerer ionischer Bindung zu gerichteter und damit stärkerer kovalenter Bindung beschreibt. Die Korrelation zwischen optischer Basizität und den Bandenverschiebungen gelang über alle drei untersuchten Glasserien hinweg.
  Bisher wurden solche Frequenzverschiebungen in IR- und Ramanspektren nur über die veränderliche Stärke eines einzelnen Bindungstyps erklärt (P-O in Phosphatgläsern) oder über veränderliche Verhältnisse zwischen zwei Netzwerkbildnern (Al/Si-Verhältnis in Alumosilicatgläsern). Beide Ansätze greifen bei den komplexeren Phospho-Alumosilicatgläsern zu kurz. Die neue Korrelation mit der optischen Basizität könnte sich als flexibler herausstellen, da die Basizität alle Glaskomponenten sowie deren Stöchiometrie berücksichtigt. Um die weitere Verwendbarkeit dieser Korrelation zu prüfen müssen jedoch zunächst weitere, einfachere Glaszusammensetzungen auf deren Gültigkeit hin untersucht werden.

- Die Untersuchung der mechanischen Eigenschaften über Indentierung warf die Frage nach dem plastischen Deformationsmechanismus auf. Ausgehend von der Poissonzahl sollte der Deformationsmechanismus der untersuchten Gläser überwiegend Verdichtung sein, mit zusätzlichen Beiträgen durch Scherung. Die Glasverdichtung in Vickerseindrücken wurde untersucht indem damit zusammenhängende Verschiebungen der Niedrigfrequenz-Ramanspektren bestimmt wurden. Gläser mit niedrigerer Ausgangsdichte zeigten höhere Verschiebungen, was auf stärkere Verdichtung hindeutete. Die Ergebnisse waren allerdings nichtlinear über der Glaszusammensetzung. Dies wurde vorläu-

fig einer Änderung des Deformationsmechanismus zugeschrieben. Um diese Zuordnung zu verifizieren und die relativen Beiträge von Verdichtung und Scherung zu bestimmen könnte eine Studie des aufgestauten Materialvolumens am Rande der Indentierungen geeignet sein.

- Im Rahmen der mechanischen Charakterisierung wurden auch die Dehnratenabhängigkeit und der Risswiderstand untersucht, hinterließen aber offene Fragen. Eine Zunahme der Dehnratenabhängigkeit bei steigendem P_2O_5-Gehalt konnte mit einer Abnahme der Dichte und einer Depolymerisierung erklärt werden. Dagegen ist ein nichtlinearer Verlauf der Dehnratenabhängigkeit bei steigendem SiO_2-Gehalt noch nicht zur Genüge verstanden.
  Der Risswiderstand zeigte große Streuung bei zunehmendem P_2O_5-Gehalt, weshalb eine Interpretation im Hinblick auf die Glaszusammensetzung zwecklos war. Dieses Problem kann höchstwahrscheinlich durch die Herstellung von Proben höherer Homogenität behoben werden, sowie durch Ausführung der Experimente unter kontrollierter Atmosphäre.

Zusammenfassend ist anzumerken, dass die Untersuchung von Gläsern der Modellzusammensetzung SiO_2 - Al_2O_3 - Na_2O - P_2O_5 die erfolgreiche Identifikation struktureller Hintergründe der gemessenen Eigenschaftsverläufe ermöglichte. Allerdings wurden auch neue, komplexere Wechselwirkungen entdeckt, die Anlass zu weiteren Untersuchungen geben, wie etwa die Konkurrenz zwischen Aluminat- und Phosphatgruppen um Natrium. Dennoch legen die Ergebnisse dieser Arbeit eine Grundlage für das Maßschneidern thermischer, optischer und mechanischer Glaseigenschaften durch simple Variation von P_2O_5- und SiO_2-Gehalt. Außerdem stellt diese Arbeit die erste umfassende Analyse der mechanischen Eigenschaften metalumischer Phospho-Alumosilicatgläser dar. Die Ergebnisse sind potentiell von Nutzen für künftige Ingenieuranwendungen sowie für geowissenschaftliche Studien zur Magmaverdichtung. Für peralkalische und peralumische Phospho-Alumosilicatgläser sind bisher keine derart detaillierten mechanischen Analysen verfügbar. Eine Erweiterung der hier gezeigten Datensätze auf diese Zusammensetzungen ist daher erstrebenswert. Die nicht-metalumischen Zusammmensetzungen könnten dabei noch weitere mögliche strukturelle Rollen für Natrium und Aluminium aufwerfen.

Selbstständigkeitserklärung

Ich erkläre, dass ich die vorliegende Arbeit selbstständig und unter Verwendung der angegebenen Hilfsmittel, persönlichen Mitteilungen und Quellen angefertigt habe.

Ort, Datum	Thilo Grammes